Doping Efficiency and Limits in Wurtzite (Mg,Zn)O Alloys

Von der Fakultät für Physik und Geowissenschaften

der Universität Leipzig

genehmigte

DISSERTATION

zur Erlangung des akademischen Grades

doctor rerum naturalium

Dr. rer. nat.

vorgelegt

von M. Sc. Abdurashid A. Mavlonov

geboren am 3. April 1986 in Taschkent

Gutachter: Prof. Dr. Marius Grundmann (Universität Leipzig)
Dr. Klaus Ellmer (Helmholtz-Zentrum Berlin)

Tag der Verleihung: 21. November 2016

Abstract

In this thesis, the structural, optical, and electrical properties of wurtzite $Mg_xZn_{1-x}O$:Al and $Mg_xZn_{1-x}O$:Ga thin films have been investigated in dependence on Mg and dopant concentration. Among the transparent conductive oxides (TCOs), ZnO based compounds have gained renewed interest as a transparent electrode for large scale applications such as defroster windows, flat panel displays, touch screens, and thin film solar cells due to low material and processing cost, non-toxicity, and suitable physical properties. In general, these applications require transparent electrodes with lowest possible resistivity of $\rho < 10^{-3}\,\Omega\,\mathrm{cm}$ and lower [1]. Recently, it has been reported that Ga and Al doped ZnO thin films can be deposited with respective resistivity of $5.1 \times 10^{-5}\,\Omega\,\mathrm{cm}$ [2] and $3 \times 10^{-5}\,\Omega\,\mathrm{cm}$ [3] which are similar to the data obtained for other practical TCOs, i.e. the resistivity of about $4 \times 10^{-5}\,\Omega\,\mathrm{cm}$ for Sn doped In_2O_3 (ITO) thin films [4]. Moreover, the bandgap of ZnO can be increased by alloying with Mg offering band alignment between transparent electrode and active (or buffer) layer of the device, e.g. Cu(In,Ga)Se_2 solar cells [5]. The tunable bandgap of these transparent electrodes can further increase the efficiency of the devices by avoiding energy losses in the interface region of the layers. From this point of view, this work has been aimed to investigate the doping efficiency and limits in transparent conductive (Mg,Zn)O alloys. For this purpose, the samples investigated in this work have been grown by pulsed-laser deposition (PLD) using a novel, continuous composition spread method (CCS). In general, this method allows to grow thin films with lateral composition gradient(s) [6, 7]. All $Mg_xZn_{1-x}O$:Al and $Mg_xZn_{1-x}O$:Ga thin films have been deposited on 2-inch in diameter glass, *c*- or *r*-plane sapphire substrates using threefold segmented PLD targets in order to grow thin films with two perpendicular, lateral composition gradients, i.e. the Mg composition is varied in one direction whereas the Al/Ga concentration is varied in a perpendicular direction [7, 8]. In order to investigate the influence of the temperature, samples grown at different substrate temperatures in the range of 25 to 600 °C were investigated. The optical and electrical measurements have been carried out on $(5\times5)\,\mathrm{mm}^2$ samples that were cut from the CCS wafers along the respective composition gradients, i.e. Mg and Al/Ga contents. Subsequently, physical properties of thin films have been analyzed for a large range of Al/Ga content between 0.5 and 7 at.%, which corresponds to doping concentrations between 2×10^{20} and $3 \times 10^{21}\,\mathrm{cm}^{-3}$, for different fixed Mg contents x(Mg) ranging from 0.01 to 0.1.

It has been found that practically the limiting the dopant concentrations is about $2 \times 10^{21}\,\mathrm{cm}^{-3}$. Further, the electrical data suggests, that the compensating intrinsic defect is doubly chargeable hinting to the zinc vacancy (V_{Zn}) as microscopic origin. Increasing the dopant concentration above $2 \times 10^{21}\,\mathrm{cm}^{-3}$ leads to a degradation of electrical and structural properties [8].

Further, the influence of growth and annealing temperatures on structural, electrical and optical properties of the films has been studied. For that purpose, Al and Ga doped ($2.5\,\text{at.\%} \mathrel{\widehat{=}} 1 \times 10^{21}\,\text{cm}^{-3}$) $\text{Mg}_{0.05}\text{Zn}_{0.95}\text{O}$ thin films have been chosen from CCS samples grown at $T_\text{g} = (25 - 600)\,°\text{C}$. For both doping series, the samples grown at higher temperatures exhibit better crystalline quality compared to the samples grown at lower growth temperatures. As a result, samples grown at higher temperatures reveal higher Hall mobility. For the Al-doping series, the highest free charge carrier density of $n = 8.2 \times 10^{20}\,\text{cm}^{-3}$ was obtained for an $\text{Mg}_{0.05}\text{Zn}_{0.95}\text{O:Al}$ thin film grown at 200 °C, with corresponding Hall mobility of $\mu = 13.3\,\text{cm}^2/\text{Vs}$, a resistivity of $\rho = 5.7 \times 10^{-4}\,\Omega\text{cm}$, and optical bandgap of $E_\text{g} = 3.8\,\text{eV}$. Interestingly, the free charge carrier density of $n \approx (5 - 8) \times 10^{20}\,\text{cm}^{-3}$ for samples grown with $T_\text{g} \leq 300\,°\text{C}$ is clearly higher than the value of $n = 1.25 \times 10^{20}\,\text{cm}^{-3}$ that was obtained for the high temperature grown sample, i.e. at $T_\text{g} = 600\,°\text{C}$. Furthermore, for all T_g, Al-doped films have a higher doping efficiency than the Ga-doped counterparts. In order to look deeper into the microscopic origin of this behavior, the samples were post-annealed in vacuum at 400 °C. Experimental results showed that the free charge carrier density of Al-doped samples first decreased and saturated afterward with increasing annealing time. On the other hand, the free charge carrier density of the Ga-doped samples first slightly increased and saturated with increasing annealing time. For both doping series, the saturation value of $n \approx 1 \times 10^{20}\,\text{cm}^{-3}$ was very close to the data that has been observed for (i) high temperature grown samples and (ii) the solubility limit of Al in ZnO of $0.3\,\text{at.\%} \mathrel{\widehat{=}} 1.2 \times 10^{20}\,\text{cm}^{-3}$, that has been determined by Shirouzu *et al.* for high temperature grown ($T_\text{g} > 600\,°\text{C}$) Al-doped ZnO [9]. Correspondingly, the optical bandgap also changed, i.e. increased (decreased) for Al- (Ga-) doping series, and approached a constant value of $3.5 \pm 0.1\,\text{eV}$ which is explained by generation of acceptor-like compensating defects, and the solubility limit of the dopants. From XRD data, no secondary phases were found for as-grown and post-annealed films. However, the slight improvement of crystalline quality has been observed on post-annealed samples. Further, it has been shown that the growth and annealing temperatures are important as they strongly affect the metastable state of the solid solution that samples grown at low temperature represent. The low solubility limit of the dopants, i.e. $\approx 0.3\,\text{at.\%}$ for Al in ZnO under equilibrium condition, can be increased by preparing samples by non-equilibrium growth techniques [10]. This is also consistent with experimental results of this work that Al- as well as Ga-doped metastable ZnO and (Mg,Zn)O thin films can be prepared with highest possible doping efficiency for the dopant concentration up to $\sim 2.5\,\text{at.\%}$ when growth or annealing temperatures below 400 °C are used.

Contents

List of Figures

List of Tables

Chapter 1

Introduction

Transparent conductive oxides (TCOs) have a phenomenal ability to combine high electrical conductivity with high optical transparency. An acceptable combination of these parameters is only realizable if the material has (i) a large bandgap of $> 3\,\mathrm{eV}$, and (ii) a high free charge carrier density exceeding $10^{20}\,\mathrm{cm}^{-3}$ together with a high mobility above $1\,\mathrm{cm}^2/\mathrm{V\,s}$ [1]. Wide bandgap semiconductors, such as oxide semiconductors, are materials of choice for the practical usage as transparent electrodes in large scale applications, e.g. thin film solar cells. CdO was the first TCO material reported by Bädeker in 1907 [11]. Subsequently, Cd-based TCO materials, i.e. CdO:In, have depicted minimum resistivity in the order of $\rho \approx 10^{-4}\,\Omega\,\mathrm{cm}$ [11–13], but currently there is no practical interest due to toxicity of the Cd element.

In general, there are a number of requirements for a good TCO which are summarized in table 1.1. One of the most important requirements is non-toxicity of the material which can be prepared with good optical and electrical properties. Currently, TCO materials used in devices contain In, Sn, or Zn [14], namely, In_2O_3, SnO_2, and ZnO. In particular, they are Sn-doped In_2O_3 (ITO), F-doped SnO_2 (FTO), and Al-doped ZnO (AZO) [13, 15, 16]. Among them, ITO is mostly used in industry due to its superior electrical and optical properties [1, 17], e.g. low resistivity of $\rho = 4.4 \times 10^{-5}\,\Omega\,\mathrm{cm}$ [18]. However, the increased number of applications, and the high price of In require alternative materials for transparent electrodes that contain ecologically friendly and cost efficient compounds with adjustable properties such as tunable bandgap which is needed for band alignment, and controllable free charge carrier density. Among the oxide compounds, the (Mg,Zn)O alloy is found to be a suitable ternary compound for transparent electrode applications, for e.g. thin film solar cells [19, 20], because of its tunable band gap, high transparency in the near ultraviolet (NUV) and visible (VIS) range of the spectrum and its readily n-type dopability for Mg contents of $x(\mathrm{Mg}) \leq 0.1$ [21–23]. It has been reported that

Table 1.1: Properties relevant to TCO materials and their applications. Adapted from Ref. [36]

General criteria	Ecologically friendly materials, sustainable processing, low material and processing cost, availability, ease of application
Opto-electronic criteria	Transparency in the visible spectral range, i.e. 400 − 800 nm, high conductivity, high carrier concentration, high mobility, suitability to flexible electronics, tunable bandgap−possibility of band alignment
Processing criteria	Low deposition temperatures, chemical stability under ambient conditions, annealing stability, compatibility with vacuum or non-vacuum processing, etchability, interfacial chemistry and surface states

the bandgap of wurtzite $Mg_xZn_{1-x}O$ can be systematically tuned from 3.3 eV up to 4.2 eV by changing the composition in the range of $0 < x < 0.44$ [23]. However, one of the main issues is to realize highly conducting (Mg,Zn)O films, since the resistivity of (Mg,Zn)O tends to increase with increasing Mg content [24–28]. It has been reported that introducing group III elements, such as Al and Ga is an efficient way to realize degenerate (Mg,Zn)O alloys with resistivity of about $\rho \approx 10^{-4}\,\Omega\,\text{cm}$ [29, 30] as it has been the case for ZnO films [31–33]. However, in other reports the minimal value of resistivity was only about $\rho \approx 10^{-3}\,\Omega\,\text{cm}$ [25–28, 34]. The increase in resistivity results from both decrease in the free charge carrier density and the mobility. To maintain a high doping efficiency is an essential point for the optimization of TCO materials. For this, limitations of the doping efficiency in the semiconductors, i.e. shallowness of the dopant energy levels, solubility limit and formation of intrinsic compensating defects, have to be considered [35].

From this point of view, this work is aimed to investigate the limitations of doping in wurtzite (Mg,Zn)O alloys in order to explore their origin and to find possible ways to avoid them. In order to approach this goal, two main strategies have been followed, namely, to investigate the doping efficiency of

(i) as-grown samples deposited at fixed growth temperature, T_g, and

(ii) post-annealed samples grown at different T_g.

In the first part, as grown thin films with high crystallographic quality, i.e. deposited at high growth temperature of 600 °C, are discussed in dependence on their composition(s) in order to analyze the influence of dopant concentration on the physical properties of the films. For this purpose, the group III elements Al and Ga have been chosen as dopants. $Mg_xZn_{1-x}O$:Al and $Mg_xZn_{1-x}O$:Ga thin films have been prepared on 2-inch in diameter c-plane sapphire substrates by pulsed laser deposition (PLD) using a continuous composition spread method (CCS) [7, 8], that allows to grow thin films with lateral composition gradient(s). Consequently, the structural, optical and electrical properties of the films have been investigated in dependence on the Al/Ga concentration in the range of 0.5 and 7 at.%, which corresponds to doping concentrations of N_d between 2×10^{20} and $3 \times 10^{21}\,\mathrm{cm}^{-3}$, for different fixed Mg contents x(Mg) ranging from 0.01 to 0.1.

In the second part, the influence of the temperature on the physical properties of the films has been investigated. For this purpose, the samples with optimal dopant concentration that were grown at different growth temperatures, i.e. $T_\mathrm{g} = (25 - 600)\,°\mathrm{C}$, have been chosen and post-annealed in vacuum at 400 °C.

This work was started based on the knowledge and experience, which had been gained over the last two decades in the semiconductor physics group at Universität Leipzig, in the area of the sample preparation, e.g. PLD as well as CCS methods [7, 14, 37, 38] and characterization, e.g. spectroscopic ellipsometry [39–41].

Chapter 2

Applications and the Status of TCOs

2.1 Applications

Early investigations on TCOs were first reported by Bädeker in 1907 [11]. He showed the possibility to prepare CdO thin films with low resistivity of $1.2 \times 10^{-3}\,\Omega$cm that could meet the requirements of most of the current TCO applications, e.g. front contacts for thin film solar cells [1]. However, extensive and systematic investigations on TCOs were started in 1950's, after (i) the first usage of TCOs in large-scale as a defrosters to protect the aircraft windshields from freezing during the World War II [42], and (ii) beginning of the "semiconductor age" after the successful realization of the first transistors in 1947 [14, 43].

As shown in table 2.1, the number of TCO applications have further increased after the first successful usage of TCOs in large-scale as defrosters, namely, chemical barriers for corrosion-resistant coating [46]; transparent front electrodes for flat panel displays [47, 48], and touch screens [49–52]; electrochromic windows [53, 54]; transparent top electrodes for thin film photovoltaics (PVs) [16, 55]; transparent infrared (IR) reflectors for energy-efficient low emissivity (low-e) windows [56, 57]; varistors [58–60], and gas sensors [61–64]. Obviously, investigation on TCOs as a transparent electrode for most of these applications has started much earlier, i.e. in 1950s, compared to usage as well as high performance that have been manifested from 1990s. This can be explained by continuous improvements on these material systems that have been achieved during the last three decades [1, 14, 33, 65]. As the majority of these applications require highly conductive TCOs, i.e. with lowest possible resistivity, most investigations on TCO materials have been directed to achieve high conductivity.

Table 2.1: Applications of the transparent electrodes. Note that the chronological order of the applications given in this table may differ.

Applications	Year	Reference
Defrosting windows	1940s	[42]
Patent: Transparent heaters for freezers	1995	[44]
Patent: Aircraft cockpits	2012	[45]
Chemical barriers for corrosion-resistant coating	1940s	
Patent: Corrosion resistant coating for metal surfaces	1943	[46]
Transparent front electrodes for flat panel displays	1950s	[47]
Patent: Low resistance electrodes useful in flat panel displays	1994	[48]
Touch screens	1960s	[49]
Patent: Resistive touch screen	1998	[50]
Patent: Capacitive touch screen	2007	[51]
Patent: Optical touch screen	2010	[52]
Electrochromic windows	1970s	[53]
Patent: Electrochromic glass for use in cars and buildings	1997	[54]
Transparent top electrodes for thin film solar cells	1970s	[55]
($\eta \approx 8.5\,\%$): CdTe cells by Matsushita		
($\eta = 13.6\,\%$): a-Si:H (stabilized) cells by AIST	2015	[55]
($\eta = 22.1\,\%$): CdTe cells by First Solar	2016	[55]
($\eta = 22.3\,\%$): CIGS by Solar Frontier	2015	[55]
Low emissivity (low-e) windows	1980s	[56]
Patent: Low transmission low emissivity glass window and method of manufacture	1993	[57]
Varistors	1990s	[58, 59]
Patent: Liquid crystal display device having varistor elements	1992	[60]
Gas sensors	2000s	[61–63]
Patent: High-sensitivity transparent gas sensor and method for manufacturing the same	2013	[64]

2.2 Research Development

In the 1950s, early reported TCOs showed relatively low conductivity. For example, first reported ITO thin films showed a conductivity of about 10 S/cm [66]. Later, the improved conductivity of around 500 S/cm was reported for In-doped ZnO films [67].

The extensive research on TCOs was done in the 1970s and 1980s. Along with other binary TCOs, i.e. In_2O_3, and SnO_2, the number of reports on ZnO thin films were also increased. Those ZnO thin films were prepared using various deposition techniques, such as spray pyrolysis [68], magnetron sputtering [69, 70], evaporation [71], as well as metal organic vapor deposition [72]. The films prepared using most of these methods needed additional heat treatment in order to obtain good electrical and optical properties, yet Minami and coworkers reported one of the first works on the realization of highly conductive and transparent ZnO thin films grown by magnetron sputtering on

TABLE 2.2: Reported dopant elements to enhance the electrical properties of binary TCOs for transparent electrode applications. The symbols of "⊙", "⊕", "⊗", "×", and "××" indicate the "very good", "good", "poor", "toxic", and "very toxic", respectively. Adapted from [4, 73]

Material	Dopant	Resistivity	Toxicity
CdO	In, Sn	⊙	××
In_2O_3	Sn, Ge, Mo, Ti, Zr, Hf, Nb, Ta, W, Te, F	⊙	×
ZnO	Al, Ga, B, In, Y, Sc, V, Si, Ge, Ti, Zr, Hf, F	⊙	
SnO_2	Sb, As, F, Nb, Ta	⊕	
Ga_2O_3	Sn	⊗	
TiO_2	Nb, Ta	⊗	

corning glass without intentional heating during and after deposition [87]. They showed the possibility of the realization of highly conductive ZnO thin films with a resistivity of $\rho \approx 5 \times 10^{-4}\,\Omega$cm, a free charge carrier density in the order of $n \sim 10^{20}\,\mathrm{cm}^{-3}$, a mobility of $\mu \approx 120\,\mathrm{cm}^2/\mathrm{Vs}$, and high transparency above 85 % in the visible (VIS) range of the spectrum. In these undoped ZnO thin films, shallow donor energy levels are expected resulting from native defects, i.e. zinc interstitials (Zn_i), that can produce free charge carrier density in the order of $n \sim 10^{20}\,\mathrm{cm}^{-3}$ [87]. In contrast, the free

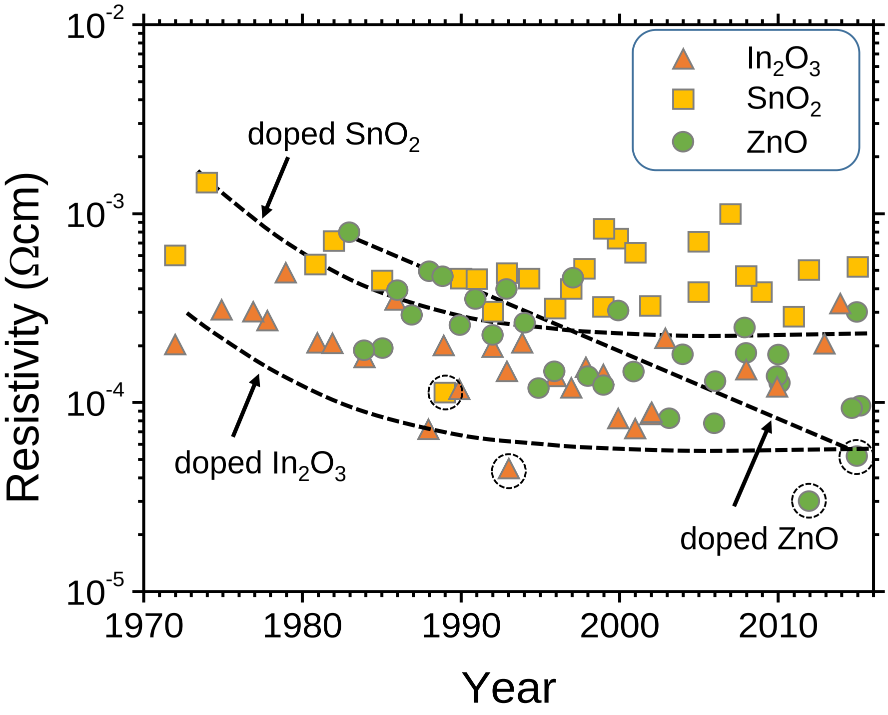

FIGURE 2.1: Reported resistivity of impurity doped In_2O_3, SnO_2, and ZnO. The dotted circles indicate the record values for each TCOs, being: $\rho = 5.1 \times 10^{-5}\,\Omega\,$cm (GZO, in 2015) [2], $\rho = 3 \times 10^{-5}\,\Omega\,$cm (AZO, in 2012) [3], $\rho \approx 1.1 \times 10^{-4}\,\Omega\,$cm (FTO, in 1989) [4], and $\rho = 4.4 \times 10^{-5}\,\Omega\,$cm (ITO, in 1993) [18]. The dashed and solid lines are guide to the eye. Data adapted from [2–4, 74–86].

Table 2.3: Electrical properties of impurity-doped ZnO. The abbreviations CVD, PLD, DS-MS and RF-MS indicate the growth methods of chemical vapor deposition, pulsed-laser deposition, dc and rf-magnetron sputtering, respectively.

Material	Dopant content	ρ ($10^{-4}\,\Omega\,\mathrm{cm}$)	n ($10^{20}\,\mathrm{cm}^{-3}$)	Growth method	T_g (°C)	Ref.
ZnO:Al	2.0 wt.%	0.3	8.6	DC-MS	370	[3]
ZnO:Al	1.6-4.6 at. %	0.85	15.0	PLD	230	[76]
ZnO:Ga	0.75 at. %	0.51	29	PLD	400	[2]
ZnO:Ga	2-7 wt.%	1.2	14.5	RF-MS	25	[4]
ZnO:B	4.0 wt.%	6.4	2.5	RF-MS	25	[94]
ZnO:In	2.0 wt.%	8.1	4.0	RF-MS	25	[94]
ZnO:Y	4.0 wt.%	7.9	3	DC-MS	200	[95]
ZnO:Sc	2.0 wt.%	3.1	6.9	DC-MS	200	[95]
ZnO:Si	2.0 wt.%	3.8	12	RF-MS	250	[89]
ZnO:Ge	1.6 at. %	7.4	8.8	RF-MS	140	[90]
ZnO:Ti	2.0 at. %	5.6	6.2	RF-MS	140	[90]
ZnO:Zr	5.4 at. %	5.2	5.5	RF-MS	140	[90]
ZnO:Hf	4.1 at. %	5.5	3.5	RF-MS	140	[90]
ZnO:F	0.5 at. %	6.5	3.9	CVD	400	[91]

charge carrier density of those undoped ZnO films exhibited a strong dependency on the growth conditions, since the source of free charge carriers, i.e. native donors, were found to be unstable at high temperatures of about $T \geq 100\,°\mathrm{C}$. Consequently, the number of investigations on impurity doped ZnO thin films increased. For this purpose, mainly the group III-elements, i.e. B, Ga, Al, and In were used as these ions were suggested to be an effective donor in ZnO [67, 88]. Additionally, group IV and also group VII elements, i.e. Si, Ge, Hf, Ti, Zr, and F, for doping ZnO thin films have been reported [89–91] where Si was found to be the best dopant in this group with achievable resistivity of $\rho = 4 \times 10^{-4}\,\Omega\,\mathrm{cm}$ resulting from the free charge carrier density of $n \approx 9 \times 10^{20}\,\mathrm{cm}^{-3}$ and mobility of $\mu \approx 10\,\mathrm{cm}^2/\mathrm{Vs}$. This favorable electrical properties, and the high stability in hydrogen plasma [1] further expands the applicability of ZnO, i.e. makes it a more suitable TCO layer for amorphous silicon (a-Si) photovoltaics (PV) compared to ITO as the characteristics of these cells were found to degrade due to the diffusion of In into the active layer [92, 93].

Recently, research on ZnO has gained renewed attention in fundamental and applied fields due to existing possibilities for using ZnO based compounds as an transparent top/front electrode in large scale application, i.e. thin film solar cells, flat panel diplays, and touch screens. In general, these applications require transparent electrodes with minimum resistivity. As shown in figure 2.1, the resistivity of impurity-doped In_2O_3 and SnO_2 has saturated during the last two decades, reaching the lowest values of

$\rho = 4.4 \times 10^{-5}\,\Omega\text{cm}$ and $\rho \approx 1.1 \times 10^{-4}\,\Omega\text{cm}$, respectively. On the other hand, resistivity of doped ZnO thin films is still decreasing and reaching minimum values of $\rho = 3 \times 10^{-5}\,\Omega\text{cm}$ (AZO) and $\rho = 5.1 \times 10^{-5}\,\Omega\text{cm}$ (GZO) that are comparable to the resistivity of doped In_2O_3 thin films. These record values have been achieved on magnetron sputtered AZO and PLD grown GZO films resulting from high free charge carrier density of $n = 8.6 \times 10^{20}\,\text{cm}^{-3}$ and $n = 2.9 \times 10^{21}\,\text{cm}^{-3}$ as well as high mobility of $\mu = 242\,\text{cm}^2/\text{Vs}$ and $\mu = 41.9\,\text{cm}^2/\text{Vs}$, respectively. Table 2.2 depicts the main dopant elements used to enhance the electrical and optical properties of the binary TCO materials. As shown in the table, doped ZnO thin films have very good electrical properties in comparison to other non-toxic compounds.

In table 2.3, the electrical transport properties of ZnO thin films are summarized for reported dopant elements. As shown in the table, Al- and Ga-doped ZnO thin films exhibit very high free charge carrier density compared to ZnO thin films doped with other elements. Thus, Al and Ga elements have been chosen to investigate degenerately doped wurtzite (Mg,Zn)O alloys, i.e. (Mg,Zn)O:Al and (Mg,Zn)O:Ga thin films, in this work.

Chapter 3

Fundamentals of ZnO

In this chapter, the fundamentals of bandgap engineering, doping mechanisms and formation energies of the native defects in ZnO are reviewed.

3.1 Structural Properties

ZnO can exhibit the (i) hexagonal wurtzite, and (ii) cubic zinc blende structures. However, only the former crystallographic phase is thermodynamically stable under ambient conditions. The wurtzite structure of ZnO was first determined by Bragg [1]. It has a space group of $P6_3mc$, in that both Zn (cation) and O (anion) sublattices have a hexagonal close-packed (hcp) structure. Figure 3.1 depicts the unit cell and the planar views of the wurtzite ZnO along the (b) [0001] and (c) $[\bar{1}\bar{1}20]$ directions. Wurtzite ZnO has bulk lattice parameters of $a = b = 3.2501\,\text{Å}$ and $c = 5.2071\,\text{Å}$ [96].

Furthermore, the (Mg,Zn)O alloy crystallizes in rocksalt structure if $x(\text{Mg}) > 0.6$ in $\text{Mg}_x\text{Zn}_{1-x}\text{O}$ (cf. figure 3.5), or grown at high pressures.

All samples investigated in this work have an hexagonal wurtzite structure.

3.2 Electrical Properties

In the tetrahedrally bonded ZnO, the s- and p-orbitals of cation and anion form sp^3-hybrids, the overlap of which leads to bonding and antibonding combinations. As a result of this, the conduction band (CB) of ZnO is mainly derived from Zn 4s states, whereas the valence band (VB) is composed by O 2p states. The CB and the VB of ZnO are separated by the bandgap, E_g. Figure 3.2 depicts the bandgap structure of wurtzite

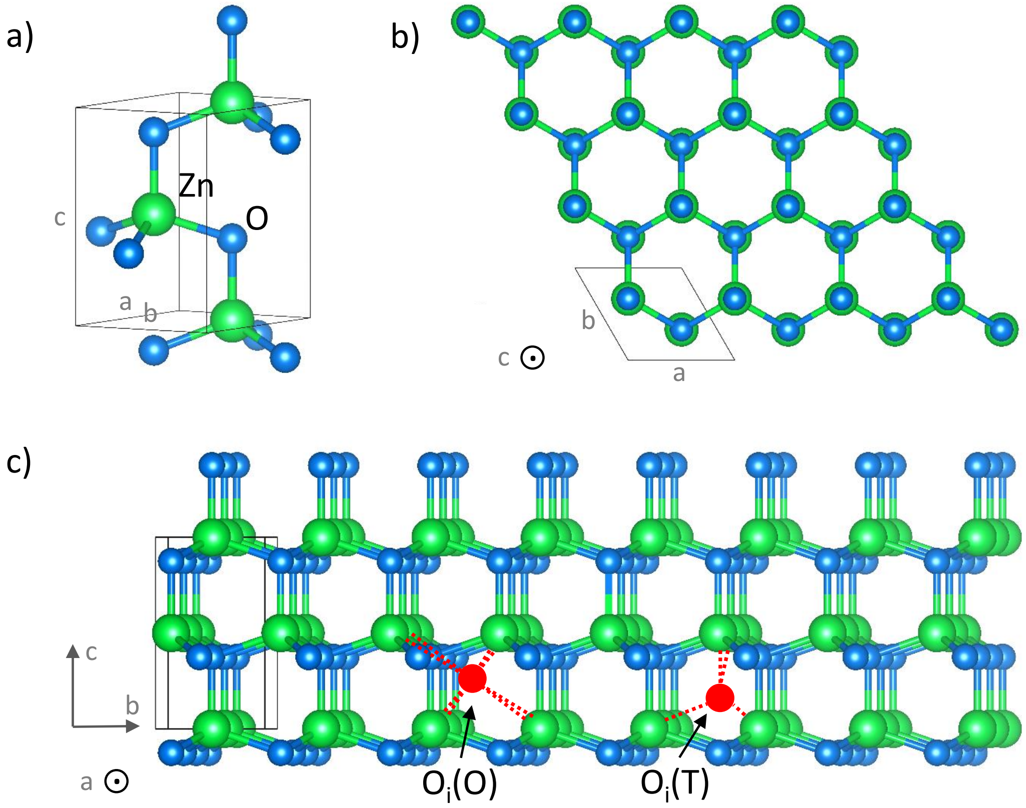

FIGURE 3.1: (a) Unit cell, and the planar views of wurtwite structure of ZnO along the (b) [0001] and (c) [$\bar{1}\bar{1}20$] directions. Red circles are the position of the oxygen interstitials at octahedral ($O_i(O)$) and tetrahedral sites ($O_i(T)$). "a", "b" and "c" indicate the axes of the hexagonal structure. Note that the lattice parameters a = b. The images were drawn using VESTA program [97].

ZnO obtained from density-functional theory (DFT) calculations within the generalized-gradient approximation including self-interaction corrections (GGA+U) [98]. As-shown in the figure, ZnO has a direct bandgap of about 3.4 eV at Γ-point.

Young *et al.* have argued that the CB of ZnO can be estimated parabolically with a density-of-states (DOS) effective mass of $m_\mathrm{d}^* \approx 0.3\,m_\mathrm{e}$ for low free charge carrier density, i.e. $n \approx 1 \times 10^{19}\,\mathrm{cm}^{-3}$, whereas strong deviation from parabolic approximation was found with an increased mass, i.e. $m_\mathrm{d}^* \approx 0.48\,m_\mathrm{e}$, in Al-doped ZnO that has a high free charge carrier density of $n \approx 5 \times 10^{20}\,\mathrm{cm}^{-3}$ [99].

3.3 Bandgap Engineering in ZnO

ZnO based compounds have gained additional attention due to the possibility to tune the bandgap by alloying with group II elements, i.e. CdO, MgO, and BeO [23]. Figure 3.3 depicts the bandgap energies of these materials as a function of $a-$lattice constant at

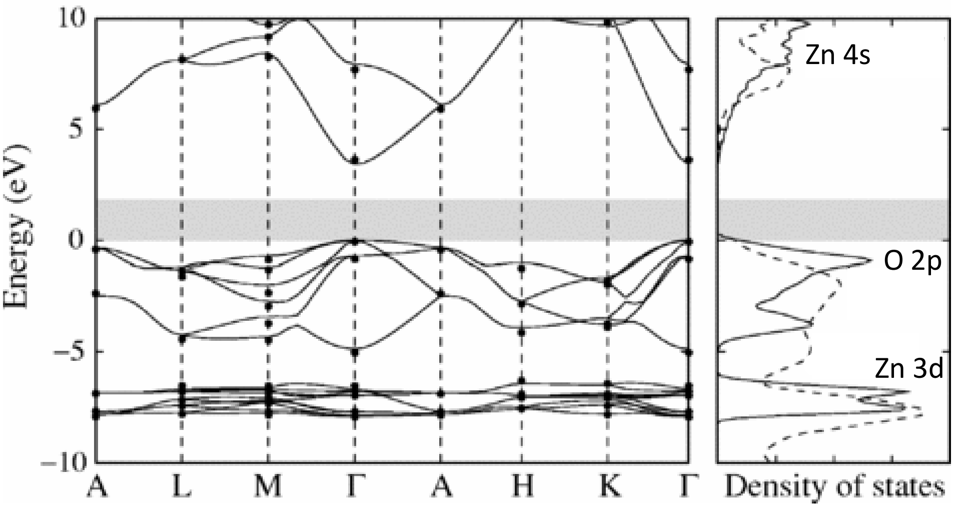

Figure 3.2: Bandgap structure of wurtzite ZnO obtained from density-functional theory calculations within the generalized-gradient approximation including self-interaction corrections (GGA+U). The conduction band states have been rigidly shifted to the experimental bandgap. In the right plot, the solid and dashed lines show the calculated and experimental density of states, respectively. The gray area indicates the calculated bandgap. Adapted from [98].

room temperature (RT). As shown, CdO has a lower bandgap energy of 2.18 eV in comparison to ZnO (3.3 eV), whereas MgO and BeO have a larger bandgap energies of 7.8 eV and 10.6 eV, respectively. Consequently, when the CdO is used for alloying, it results to decrease the bandgap of ZnO, whereas the MgO and BeO compounds affect to increase the bandgap. Among these ternary compounds, (Mg,Zn)O alloy has gained more attentions due to its non-toxicity. Additionally, it has been reported that the structural properties of wurtzite (Mg_xZn_{1-x})O solid solution, i.e. $0 < x < 0.6$, remains almost unchanged with changing the Mg content [23]. Figure 3.4 depicts the reported $c-$lattice constant of (Be,Zn)O and wurtzite (Mg,Zn)O alloys as a function of Be/Mg content. In the former, $c-$lattice constant showed a strong dependency on Be content, whereas it shows a much weaker dependence on Mg content in (Mg,Zn)O alloy. As a result, the (Mg,Zn)O alloy has been widely investigated as it has an advantage of usage in the following applications. They are:

(i) band alignment for thin film photovoltaics, i.e. CIGS thin film solar cells [19, 20].

(ii) ZnO/(Mg,Zn)O heterostructures [100].

One of the main requirements of bandgap engineering is avoidance of phase separation as the efficiency and the performance of the devices are strongly dependent on the crystalline quality. For instance, Rao *et al.* [5] have studied that the conduction band offset of −0.3 eV at ZnO/CdS interface can be avoided at CdS/$Mg_{0.15}Zn_{0.85}$O interface

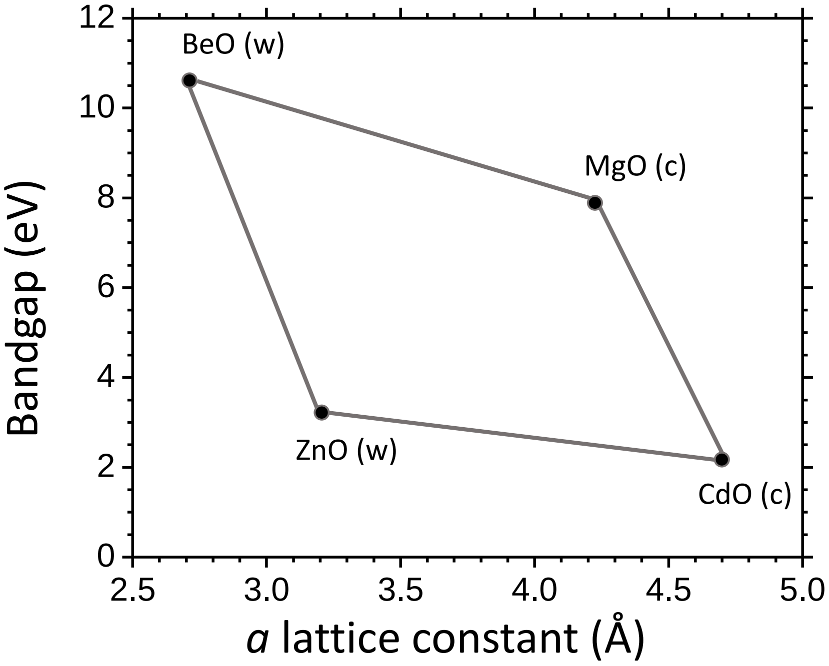

Figure 3.3: The bandgap energy versus a-lattice constant of ZnO, CdO, MgO, and BeO. "c" and "w" denote the cubic and wurtzite structure of the respective materials.

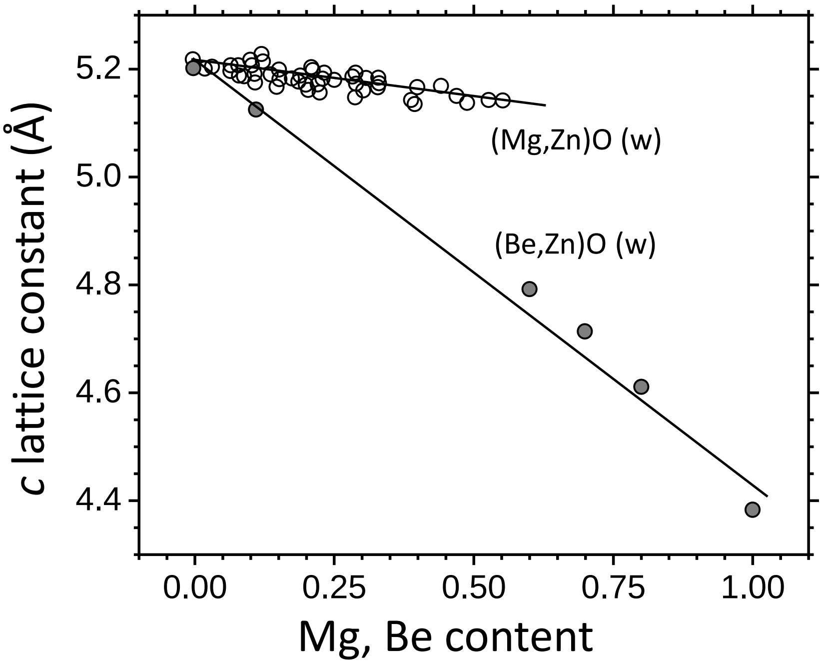

Figure 3.4: c-lattice constant of (Mg,Zn)O, and (Be,Zn)O alloys as a function of Mg and Be content. "w" denotes the wurtzite structure. Adapted from [23].

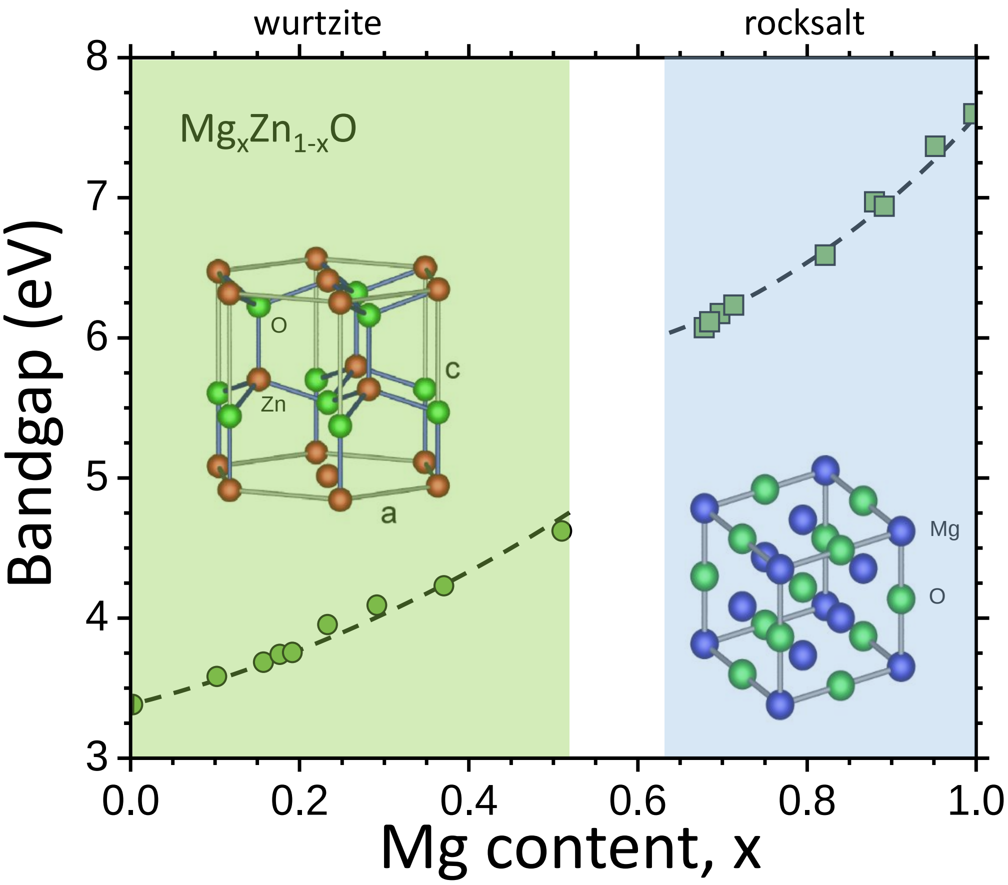

FIGURE 3.5: The bandgap energy of (Mg,Zn)O alloy versus Mg content. The data for the wurtzite and rocksalt structures adapted from [39] and [40], respectively.

(cf. figure 3.6). It has been reported that the bandgap of wurtzite $Mg_xZn_{1-x}O$ can be systematically tuned from 3.3 eV up to 4.2 eV by changing the composition in the range of $0 < x < 0.44$ [23]. In many reports, the experimentally obtained bandgap showed a linear increase with increasing Mg content [101–103]. Von Wenckstern *et al.* have summarized the experimental values of the bandgap [23], and they found that the composition evolution of the bandgap energy could be well described by Vegard's law including bowing parameters, that can be summarized for wurtzite-phase and rocksalt-phase as following [104]:

$$E_g(\text{wurtzite} : Mg_xZn_{1-x}O) = 3.339 + 1.241x + 1.89x^2, \tag{3.1}$$

$$E_g(\text{rocksalt} : Mg_xZn_{1-x}O) = 3.679 + 1.516x + 2.48x^2. \tag{3.2}$$

This character of the bandgap energy can be qualitatively explained by the molecular orbital theory. Zhang *et al.* performed a first-principles total energy study to investigate the electron exchange correlation in (Mg,Zn)O alloy using the generalized gradient

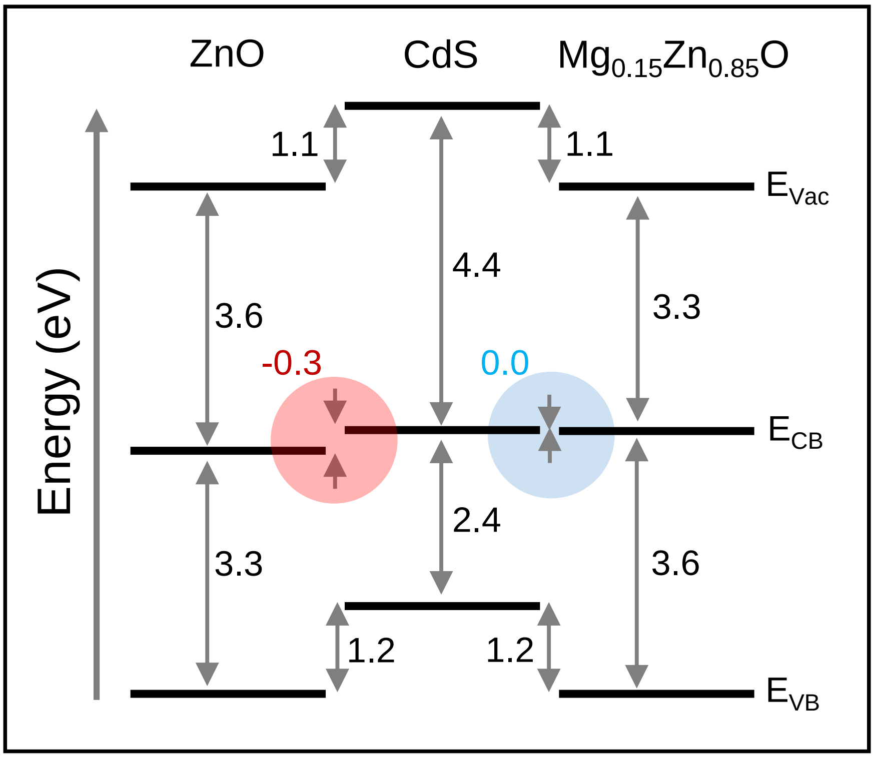

FIGURE 3.6: Band alignment at ZnO/CdS and CdS/$Mg_{0.15}Zn_{0.85}O$ interfaces. Adapted from [5].

approximation (GGA). They argued that bandgap widening occurs with increasing Mg content in (Mg,Zn)O due to the decrease of the Zn 4s states [105]. Similar arguments can be made using the Bloch theorem where the bandgap is determined by the bond strength. Since Mg-O has a stronger bond than Zn-O, a larger bandgap is expected for increased Mg content [104].

3.4 Native Point Defects in ZnO

In this section, the formation energy of electrically active native defects is discussed.

Native defects in ZnO have been extensively investigated using first-principles studies in literature with regard to its non-stoichiometry and n-type conductivity [106, 107]. Recently, Oba *et al.* have reviewed the status of these first-principles approaches to point defects, defect energetics, atomic and electronic structures, defect-induced properties of ZnO focusing on the energetics of the native defects [108]. Based on this study, the formation energy of the native defects in ZnO is described here with regard to the n-type conductivity of ZnO, i.e. the Fermi energy level of $E_F > 3\,\text{eV}$, where $E_F = 0$ corresponds to the energy of the valence band maximum. Figure 3.7 depicts the formation energy

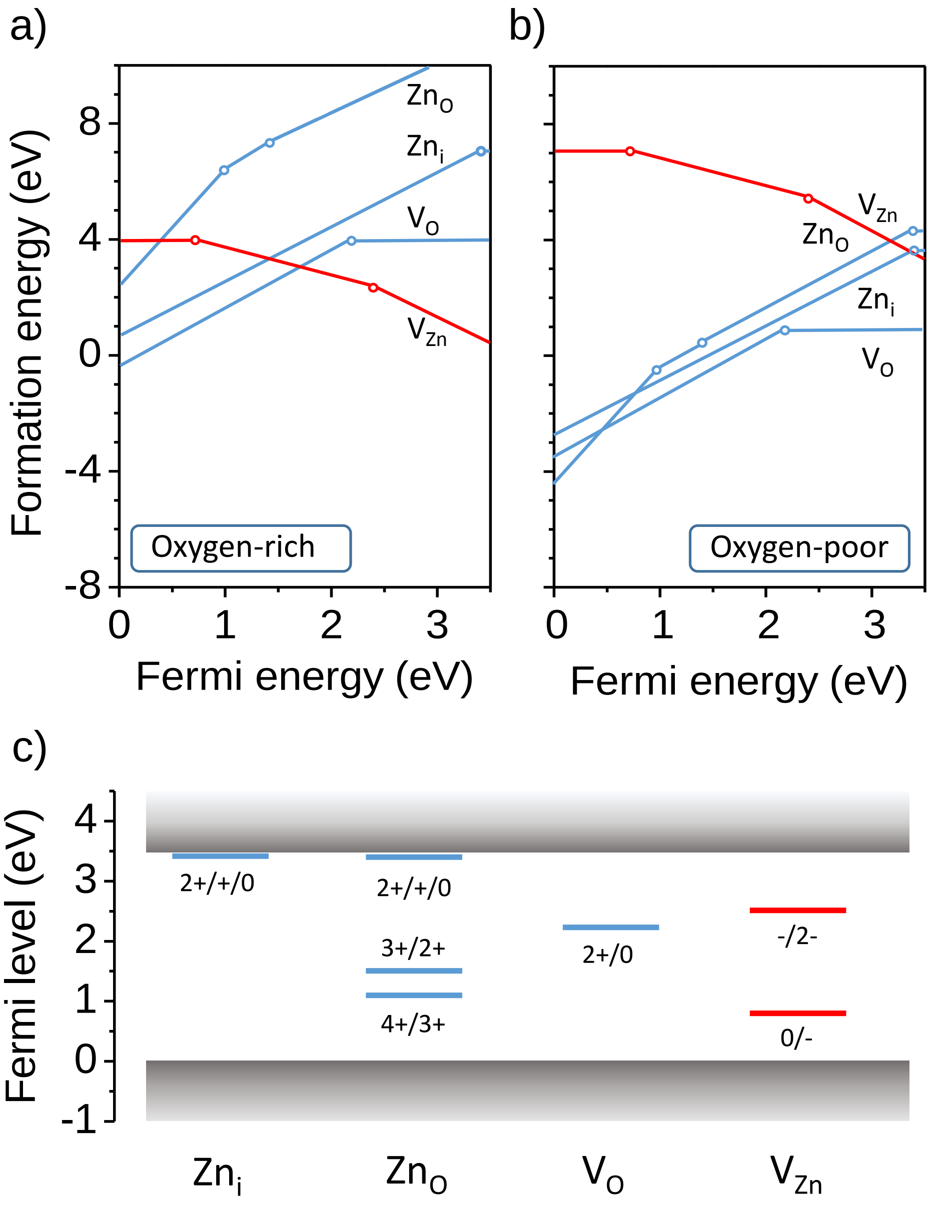

Figure 3.7: Formation energies and thermodynamic transition levels of the Zn interstitial at the octahedral site (Zn_i), the Zn anti-site (Zn_O), the O vacancy (V_O), and the Zn vacancy (V_{Zn}) in ZnO for (a) O-rich (Zn-rich) and (b) O-poor (Zn-rich) limits. (c) Thermodynamic transition levels corresponding to the open circles in (a, b). Donor (acceptor) like defects are given with blue (red) color or plus (minus) sign. The numbers indicate the charge state of the defects. Data adapted from [108].

of native point defects in ZnO as a function of Fermi energy level for (a) oxygen-rich (zinc-poor),(b) oxygen-poor (zinc-rich) limits, and (c) thermodynamic transition levels that are given with open circles in (a, b). In the following, the native defects that are electrically active in ZnO are discussed.

Zinc interstitial

In general, the zinc interstitials (Zn_i) can occupy two positions: (i) the octahedral site, i.e. $Zn_i(O)$, or (ii) the tetrahedral site, i.e. $Zn_i(T)$, of the wurtzite structure of ZnO. In figure 3.7, only $Zn_i(O)$ is considered as the latter one has been reported to be energetically less favorable [109, 110] or dynamically unstable [111–113]. The transition level of Zn_i is close to the conduction band minimum (CBM), i.e. within 50 meV, hence it is a shallow donor. In contrast, even for oxygen-poor limit, Zn_i has a high formation energy of ~ 4 eV if the Fermi level energy is close to the conduction band. Thus, its concentration is expected to be low in thermal equilibrium.

Zinc anti-site

Zinc anti-sites (Zn_O) are located at the oxygen sites. Similar to Zn_i, it also depicts a transition level of $\epsilon(2+/+/0)$ in the vicinity of the CBM (cf. figure 3.7 c). Additionally, the Zn_O has a two transition levels of $\epsilon(4+/3+)$ and $\epsilon(3+/2+)$ located below the mid bandgap. In other words, the Zn_O involves both shallow as well as deep donor levels. However, the formation energy of Zn_O for n-type condition is higher compared to Zn_i. Therefore its formation is unlikely for n-type ZnO.

Oxygen vacancy

The oxygen vacancy (V_O) has only one thermodynamic transition level of $\epsilon(2+/0)$ located at 2.2 eV above the valence band maximum (VBM) or 1.2 eV below the CBM. As-shown in figure 3.7 (a, b), the 2+ charge state is electrically favorable for low Fermi energy level (E_F), i.e. below the thermodynamic transition level, and the formation energy depends on the E_F. With increasing E_F, the formation energy approaches the neutral state at 2.2 eV above the VBM. For n-type conditions, i.e. E_F is close to the CBM, it is much preferable in comparison to other defects by depicting the lowest formation energy of 1 eV for oxygen-poor limit (cf. figure 3.7 b). Therefore, V_O has been suggested to be a source of non-stoichiometry in ZnO. On the other hand, despite its low formation energy, V_O has a deep donor level that limits its contribution to n-type conductivity.

Zinc vacancy

The zinc vacancy (V_{Zn}) has been suggested to be a major acceptor-like defect in ZnO [98, 106, 108, 114] that has two acceptor levels of $\epsilon(0/-)$ and $\epsilon(-/2-)$ located at 0.7 eV and 2.4 eV above the VBM, respectively. As shown in figure 3.7 a, for oxygen-rich (zinc-poor) limit, the formation energy of the V_{Zn} is very low. And under oxygen-poor chemical potential conditions, the formation energy increases, being about 4 eV for n-type condition. Despite this increased formation energy, i.e under oxygen-poor chemical potential condition, V_{Zn} still remains as main acceptor-like defect in n-type ZnO by strongly contributing to unintentional compensation of free charge carriers [115].

3.5 Doping in ZnO

For transparent electrode applications of ZnO, thin films are needed with highest possible carrier mobility and free charge carrier density at RT. The former can be maintained by preparing samples with high crystalline quality, while the latter can be achieved using two approaches, namely by:

(i) creating intrinsic donors in the lattice, or

(ii) introducing extrinsic dopants.

In the following, these approached are explained in brief.

3.5.1 Intrinsic Doping

As already described above, non-intentionally doped ZnO crystals had good conductivity resulting from the deviations of stoichiometry [1, 87]. In other words, electrically active intrinsic defects − oxygen vacancies (V_O) or Zn interstitials (Zn_i) [116] form intrinsic dopants in ZnO. The former has been proved by annealing experiments. The resistivity of the samples increased (decreased) when they were annealed in an oxygen atmosphere (vacuum) [1]. The latter one has been verified by high-energy (MeV) electron irradiation studies [117].

Obtained low resistivity of ZnO thin films by intrinsic doping is still insufficient for transparent electrode applications due to their (i) increased resistivity under heat treatment, and (ii) decreased optical transmittance for increased Zn access. These limitation can only be surpassed by extrinsic doping.

3.5.2 Extrinsic Doping

Extrinsic doping of n-type ZnO thin films is mainly carried out by the addition of group III elements, i.e. Al, Ga, and In ions. These ions were expected to be hydrogenic dopants in ZnO [67, 88]. Furthermore, other dopants, i.e. group IV elements have been reported. As discussed earlier, the group III elements, i.e. Al, and Ga, doped films have depicted the highest electrical transport properties (cf. table 2.3). In general, it is assumed that the group III elements substitute Zn cations in ZnO, giving one free electron into the system that is not required for bonding [118]. This process introduces additional energy levels, i.e. donor ionization energies, within the bandgap. For Al, Ga and In, it is located at 53 meV, 54.6 meV and 63.2 meV below the CBM [119]. As discussed in chapter 2, free charge carrier densities of $n \approx 10^{21}\,\mathrm{cm}^{-3}$ have been obtained by extrinsic doping of ZnO thin films. In these films, the donor levels overlap and form an impurity band. Hence, these material systems are then called degenerately doped where free electrons can be described similar to the electrons in metals. In wurtzite (Mg,Zn)O alloys, the donor ionization energies of Al, Ga and In have been suggested to remain unchanged. Ke *et al.* [10] have calculated the ionization energies of Al, Ga and In dopants in $\mathrm{Mg}_x\mathrm{Zn}_{1-x}\mathrm{O}$ alloys using supercell approach (SCA) and found that the Al and the Ga dopants remain as hydrogenic donors over the whole studied composition range of $0 \leq x \leq 0.5$, whereas only In donors show a pronounced deep level character for Mg compositions above $x \geq 0.4$. Corresponding to these theoretical results, high free charge carrier density of $n \approx 10^{21}\,\mathrm{cm}^{-3}$ has been also depicted for $\mathrm{Mg}_x\mathrm{Zn}_{1-x}\mathrm{O}$ alloys for Mg compositions in the range of $0 \leq x \leq 0.1$ [29]. However, it has been found that the free charge carrier density tends to decrease with increasing Mg content in impurity doped (Mg,Zn)O solid solutions. This can be explained as following: Mg as well as dopant ions, i.e. Al or Ga, substitute the Zn cations, where increased Mg incorporation in the system reduces the doping efficiency due to the limited number of available places for dopant ions. However, the expectation is that non-equilibrium growth methods might increase the incorporation of impurities, i.e. Al, [120, 121] in ZnO in comparison to equilibrium solubility limit of 0.3 at. % for Al in ZnO [9].

On the other hand, extrinsic dopants do not only increases the free charge carrier density, but also affects to the mobility. In degenerately doped ZnO:Al films, one of the best reported mobilities is $47.6\,\mathrm{cm}^2/\mathrm{Vs}$, i.e. not very different from that in highly doped (crystalline) silicon [122]. As shown in figure 3.8, grain boundary scattering can well describe the experimental data at lower free charge carrier densities, i.e. $n < 10^{20}\,\mathrm{cm}^{-3}$, while it overestimates the mobility at higher values. In this regime, the mobility can be explained by Brooks-Hering theory of ionized impurity scattering including non-parabolicity of the conduction band at high free charge carrier densities, i.e. $n \sim 10^{21}\,\mathrm{cm}^{-3}$ (cf. figure 3.8). Additional to these scattering mechanisms, alloy scattering [123], caused by modification of the lattice potential due to alloying, i.e. in $\mathrm{Mg}_x\mathrm{Zn}_{1-x}\mathrm{O}$, is also suggested to reduce the mobility. For degenerate $\mathrm{Mg}_{0.1}\mathrm{Zn}_{0.9}\mathrm{O}$, a theoretical value of $\mu_{\mathrm{alloy}} \approx 100\,\mathrm{cm}^2/\mathrm{Vs}$ has been calculated [124]. In other reports, it has been argued that changes in effective mass also contributes in changes in mobility [23]. Matsubara *et al.* have provided first evidences that the effective mass of $\mathrm{Mg}_x\mathrm{Zn}_{1-x}\mathrm{O}$ thin films increases with increasing x [24].

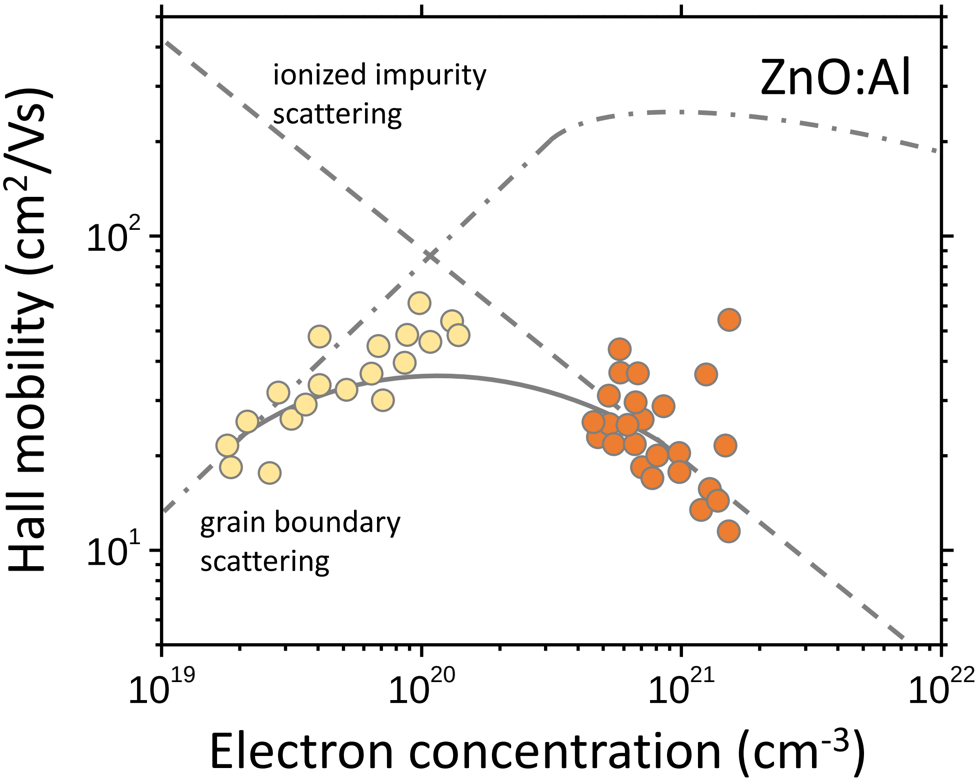

FIGURE 3.8: Hall mobility of ZnO:Al thin films as a function of free charge carrier density. The *dash-dotted line* is the mobility in the presence of grain boundaries. The *dashed line* is Brooks-Hering theory of ionized impurity scattering including non-parabolicity of the conduction band. The *solid line* is combined theory. The *circles* are experimental data. Adapted from [4, 14].

3.5.3 Doping Limitations

There are limitations for doping of semiconductors that have been summarized by Zhang *et al*. [35], namely:

- shallowness of the dopant energy levels in the sense of small thermal activation energy such that these dopants are ionized at room temperature (RT),
- solubility limit of impurities in host material, which affects the formation of secondary crystallographic phases, and
- formation of intrinsic compensating defects, i.e. acceptors in n-type ZnO and (Mg,Zn)O thin films.

This work is aimed to investigate these limitations of doping in wurtzite (Mg,Zn)O alloys.

3.6 Amphoteric Defect Model

The doping efficiency is an essential point for the optimization of TCO materials. There have been several theoretical and experimental attempts to investigate the mechanisms that are responsible for the reduction of the doping efficiency [125–128]. Among these works, the amphoteric defect model (ADM) has been successfully applied to understand the doping related phenomena in several semiconductors. That is briefly discussed for II-VI compounds in the following. For more details, the reader is referred to [129–131].

In general, ADM explains the saturation of the free charge carrier density in semiconductors that could provide a rather simple phenomenological rule capable of predicting trends in the doping behavior of semiconductor materials. The point defects and dopants of the material system can be divided into two classes:

- delocalized, shallow dopants, and
- highly localized defects and dopants.

Shallow hydrogenic donors, e.g. group III elements in ZnO and (Mg,Zn)O, and acceptors belong to the former class. The wave functions of these defects are delocalized and formed mostly close to the CBM or the VBM. Consequently, the energy levels of these defects are closely correlated with the respective band edges, i.e. CB for donors, and the VB for acceptors. As a result, these energy levels will follow the respective band edges when the locations of the edges change due to external perturbation, i.e. changing the alloy composition. On the other hand, wave functions of highly localized defects cannot be combined with any particular band structure extremum and are rather derived from extended states of the whole Brillouin zone with most substantial contributions coming from the regions of large density of states (DOS) in the CB and the VB. Therefore, the energy levels of these defects are not sensitive to the location of the comparatively low DOS at the CBM and VBM. For instance, transition metal impurities belong to this class of dopants with their highly localized d shells [131, 132]. As a result, the energy levels of the transition metals have been used as energy references to determine the band offsets in III-V and II-VI compounds due to their insensitivity to the position of local band extrema, i.e. CBM or VBM [133].

Due to this localized nature of native defects, the Fermi energy stabilizes at a certain energy level labeled E_{FS} and called Fermi level stabilization energy when the properties of the semiconductor material are fully controlled by native defects in equilibrium condition (i.e. for very large concentrations of native defects introduced by e.g. particle irradiation). It has been found that the energy level that corresponds to this Fermi

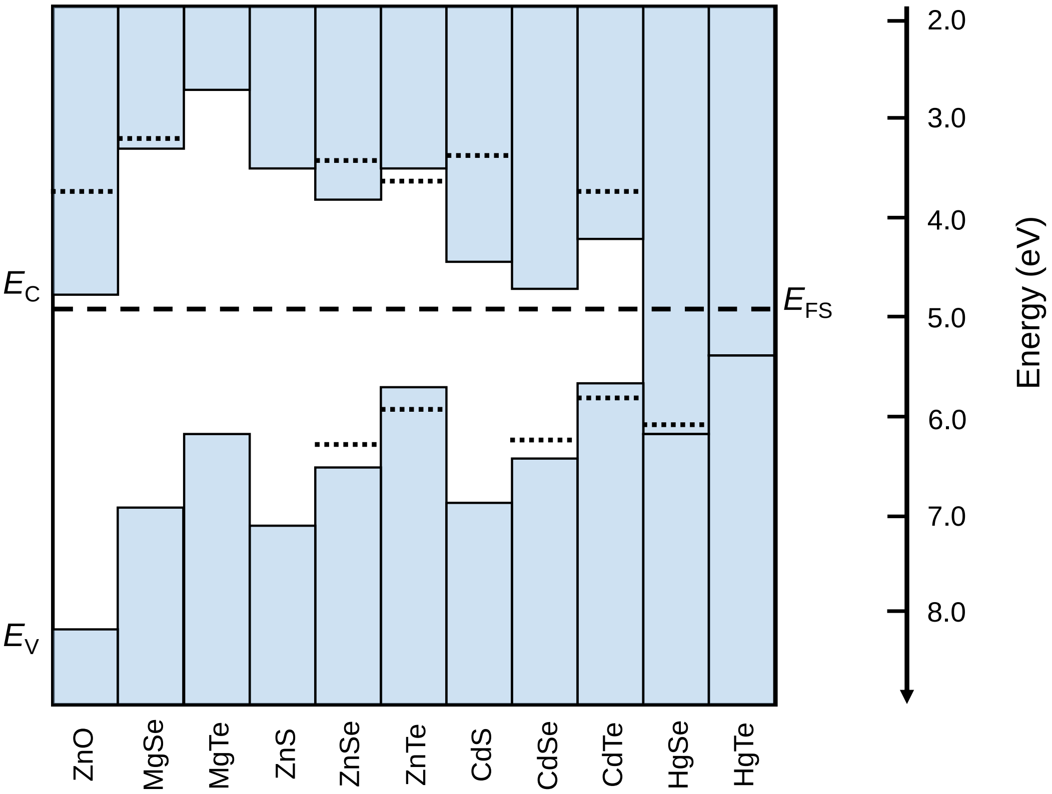

FIGURE 3.9: Band offsets in II-VI compounds. E_{FS} represents the Fermi level stabilization energy at about 4.9 eV below the vacuum level. E_{C} and E_{V} are the CBM and the VBM, respectively. The dotted lines represent positions of the Fermi energy corresponding to the highest hole and electron concentrations reported for the given material. Adapted from [126, 131].

level stabilization energy is independent of the level or the type of doping level prior to the introduction of the native defects. Thus, it is considered to be an intrinsic material property.

Figure 3.9 shows the E_{FS} for different II-VI compounds that has been found from the studies of semiconductor materials heavily damaged with high gamma rays or electrons [131]. Interestingly, E_{FS} is located approximately at a constant energy of about 4.9 eV below the vacuum level for all compounds indicating that it is an intrinsic parameter of the materials. In the case of ZnO, the CBM is located very close to E_{FS} at $E_{\mathrm{FS}} + 0.2\,\mathrm{eV}$ in comparison to the VBM that lies at the very low energy of $E_{\mathrm{FS}} - 3.1\,\mathrm{eV}$. According to ADM, n-type conductivity is favorable for such an alignment. Existing experimental data also support the fact that impurity doped ZnO can exhibit free charge carrier density of $n \approx 10^{21}\,\mathrm{cm}^{-3}$ [2, 4, 76], whereas the extremely low position of the VBM indicates that it is very difficult to achieve any p-type doping of ZnO.

3.7 Optical Properties

Generally, transparent conductive oxide thin films are highly transparent in the visible (VIS), ≈(400-800) nm, spectral range. As depicted in figure 3.10, in the low wavelength (high energy) region, the transparency of TCO materials, e.g. ZnO, is limited by absorption related to band-band (BB) transition. However, alloying the ZnO with Mg increases the bandgap, thus improving the transparency in this, high energy range. On the other hand, in the near infrared (NIR) spectral range, i.e. (800-2500) nm, the transparency is mainly limited due to absorption caused by the contribution of the free carriers (FC). The contributions of free charge carriers can be described by classical Drude approximation, where the real part of the dielectric constant can be written as [134]:

$$\mathrm{Re}\{\epsilon\} = \epsilon_\infty - \frac{ne^2}{\epsilon_0 m_e^* \omega^2}, \tag{3.3}$$

where, n is the free charge carrier density, e is the elementary charge, ϵ_∞ is the high-frequency dielectric constant, ϵ_0 is the permittivity of vacuum, m_e^* is the effective electron

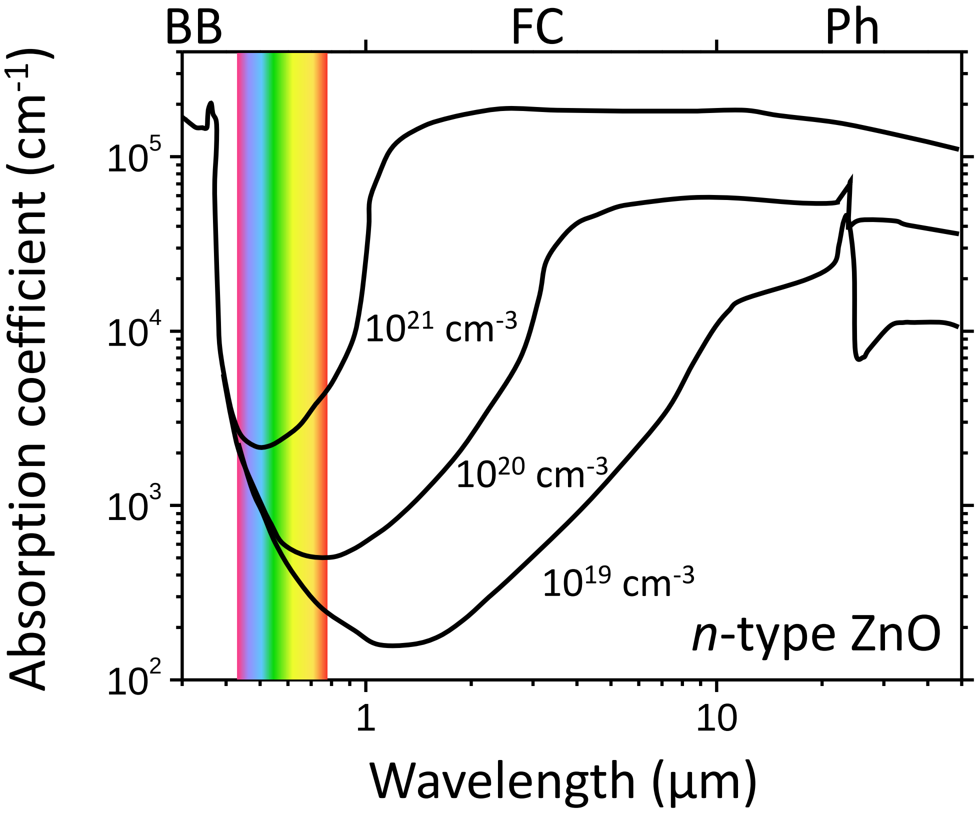

Figure 3.10: Absorption coefficient of n-type ZnO for different level of free charge carrier density. *Colored area* is the visible spectral range. "BB", "FC", and "Ph" indicate the contribution of absorption processes to band-band transition, free carrier absorption, and phonon-related absorption, respectively. Adapted from [122].

mass, and ω is the angular frequency of the light. For $\mathrm{Re}\{\epsilon\} = 0$ condition, equation 3.3 yields the plasma frequency ω_p:

$$\omega_\mathrm{p} = \left(\frac{ne^2}{\epsilon_\infty \epsilon_0 m_\mathrm{e}^*} \right)^{1/2}. \tag{3.4}$$

If $\omega > \omega_\mathrm{p}$, the material is transparent until interband transitions occur and for $\omega < \omega_\mathrm{p}$, the material becomes reflective [134]. Thus, the transparency of the material in NIR spectral range depends on ω_p (or n and m_e^*). Since, increasing the free charge carrier density results in increasing the ω_p towards the VIS spectral range (cf. figure 3.10), this limits the maximum free charge carrier density of TCOs to several $n \sim 10^{21}\,\mathrm{cm}^{-3}$ [122].

Chapter 4

Sample Growth

4.1 Target Preparation

The ceramic PLD targets that have been used in this work were fabricated by G. Ramm (Universität Leipzig). For this purpose, targets with four different compositions, being binary ZnO, (Mg,Zn)O, ZnO:Al and ZnO:Ga, were separately prepared. For (Mg,Zn)O, ZnO:Al and ZnO:Ga targets, 5N5 ZnO powder was mixed with high purity powder of MgO, Al_2O_3 and Ga_2O_3, respectively. Table 4.1 summarizes the sources and used contents of the materials in the targets. During the first process, the powder was homogenized by ball milling. Subsequently, the homogenized powder was pressed and then sintered for 12h at about 1150 °C. Further, each target was cut into pieces using a diamond saw in order to assemble segmented PLD targets for thin film deposition with continuous composition spread method. The geometries of cut targets are given in figure 4.1 and figure 4.2.

Table 4.1: Sources and purity of the powders used for target preparation. Binary ZnO, as well as (Mg,Zn)O, ZnO:Al and ZnO:Ga targets were used as CCS PLD target segments with admixtures of corresponding powders.

source powder	purity (%)	admixture (wt. %) to 5N5 ZnO powder	producer
ZnO	99.9995	–	Alfa Aeser GmbH [135]
MgO	99.998	8	Alfa Aeser GmbH [135]
Al_2O_3	99.995	0.5, 5	Alfa Aeser GmbH [135]
Ga_2O_3	99.998	0.5, 5	Sigma-Aldrich GmbH [136]

Table 4.2: Parameters of PLD chamber used for thin film deposition.

Parameters	*W-chamber*
Inner diameter × height	405 mm × 335 mm
Target-to-substrate distance	90-110 mm
Target holder	4 targets, rotation and lateral translation
Substrate holder	rotation and adjustable lateral offset
Maximal substrate size	3-inch in diameter
Maximal substrate temperature	$\sim 700\,^{\circ}\mathrm{C}$
Base pressure	10^{-7} mbar
Background gas pressure	10^{-5} mbar - 10 mbar
Background gases	Ar, O_2, N_2

4.2 Pulsed-Laser Deposition

Pulsed-laser deposition (PLD) is a comparatively simple, non-equilibrium physical growth method [38, 101]. All thin films investigated in this work have been prepared by H. Hochmuth (Universität Leipzig) using PLD by applying the continuous composition spread method. A Lambda Physik LPX 300 excimer laser that operates at 248 nm with a laser pulse energy of 600 mJ was used. Similar to other deposition methods, PLD process depends on material system, growth temperature and the energy of the incident particles that can be controlled via laser energy and the background gas, i.e. oxygen partial pressure.

Figure 4.1 depicts the schematic view of the PLD chamber. The PLD chamber used in this work for the thin film growth is referred to as "*W-chamber*". The advantages of this chamber are the synchronously rotating substrate holder with respect to the rotating target, and homogeneously heating of the substrate that has a size of about 2-inch in diameter [38]. These are the main requirements to realize continuous composition spread approach by ablating a segmented PLD target, and at the same time to minimize the thickness gradient of the film. As discussed in chapter 2, the optical and electrical properties of the films are strongly dependent on the oxygen partial pressure where O-poor (Zn-rich) chemical potential conditions have been suggested to be a better choice to grow highly conductive n-type ZnO. All samples investigated in this work have been grown at low oxygen partial pressure of 0.016 mbar in order to (i) ensure a laterally homogeneous deposition on the large-area substrate and (ii) obtain highly conductive thin films. $\mathrm{Mg}_x\mathrm{Zn}_{1-x}\mathrm{O}$:(Al/Ga) thin films were grown on 2-inch in diameter c-plane sapphire wafers using a single but threefold segmented PLD target. The samples have been grown at different substrate temperatures, in the range of $(25 - 600)\,^{\circ}\mathrm{C}$.

PLD is a non-equilibrium growth method that allows to deposit thin films in metastable state. Recent investigations, i.e. including this work, showed that CCS method can

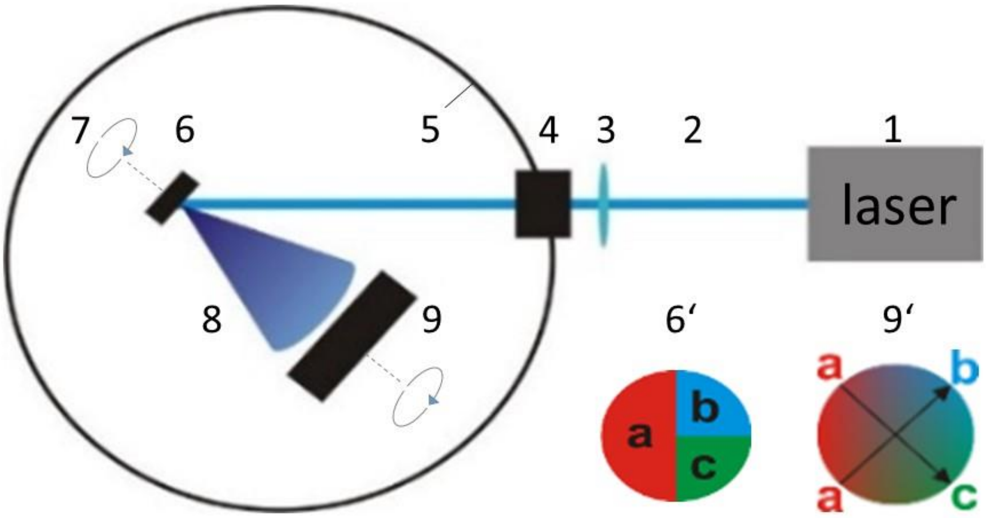

FIGURE 4.1: Schematic view of a PLD system. The labeling numbers indicate: 1: the laser, 2: laser beam, 3: converging lens, 4: entrance window, 5: PLD chamber, 6: PLD target, 7: axle, 8: plasma plume, 9: substrate on the heatable holder. 6' and 9' are the top views of the threefold segmented PLD target and the simulation of two continuous composition gradients in the film [7], respectively. The vacuum pump and inlets for background gas are not shown.

be applied without major changes in PLD chamber. Additionally, a large number of materials can be easily deposit using PLD method. However, PLD is only suitable for small substrates (up to 4-inch in diameter) and has a relatively low growth rate compared to other growth methods, i.e. magnetron sputtering, which makes it unlikely for large scale fabrication of thin films.

4.3 CCS-PLD

One of the main goals of this work is to prepare samples with similar or same growth conditions using continuous composition spread method (CCS) in order to compare their physical properties precisely, since it is difficult and time consuming to prepare a large number of sample series under similar growth conditions. From this point of view, all samples investigated in this thesis have been deposited using continuous composition spread method (CCS). This approach of using segmented targets was adopted by von Wenckstern *et al.* to a PLD process [7]. Recent investigations showed that the CCS method can be applied to PLD technique to investigate multicomponent oxide materials and obtained very systematic and fruitful results [41, 137–141].

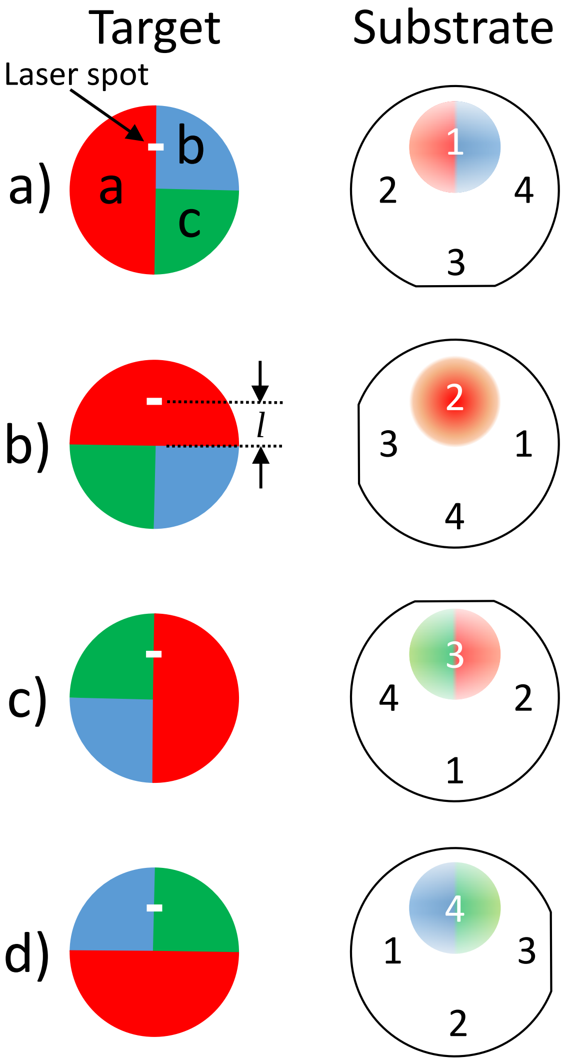

FIGURE 4.2: Schematic view of the continuous composition spread approach for pulsed-laser deposition. As an axample, four different positions of the laser spot on the segmented PLD target and corresponding plasma plume that reaches the substrate are illustrated. To deposit the samples investigated in this work, target segments of “a”, “b”, “c” were chosen to be binary [“ZnO”, “ZnO + MgO”, “ZnO + Al_2O_3”] or [“ZnO”, “ZnO + MgO”, “ZnO + Ga_2O_3”]. l is the distance between the laser spot and the center of the target.

In figure 4.2 a threefold segmented PLD target used in this work is shown together with a simulation of the film with a two-dimensional, lateral variation of the material composition. In order to deposit (Mg,Zn)O:Al and (Mg,Zn)O:Ga thin films, target segments of [“a”, “b”, “c”] were chosen to be binary [“ZnO”, “ZnO + MgO”, “ZnO + Al_2O_3”] and [“ZnO”, “ZnO + MgO”, “ZnO + Ga_2O_3”], respectively. The Concentrations of the impurities, i.e. Mg, Al, and Ga, used in the target segments are given in table 4.1.

4.4 Sample Preparation for Measurements

For the optical and electrical measurements, thin films grown on 2-inch in diameter wafers, i.e. *c*-plane sapphire or glass substrates, were cut into pieces using a diamond saw. The $(5\times5)\,\mathrm{mm}^2$ pieces were prepared along the respective composition gradients shown in figure 5.1. In order to avoid possible side effects of cutting, the surface of the wafers were protected with photo-resist during sawing process. As a result, a large material library has been created that containing the thin films with a different Al/Ga dopant concentration of $0.5\,\mathrm{at.\%} < \mathrm{Al/Ga} < 7.0\,\mathrm{at.\%}$ and Mg alloy content of $0.01 < x(\mathrm{Mg}) < 0.1$. The maximal variation of the chemical composition within such a $(5\times5)\,\mathrm{mm}^2$ piece is about $\pm0.4\,\mathrm{at.\%}$ for the Mg-content and the dopant concentration. The series of the measurements have been organized as following:

- The chemical composition of the films was determined by EDX measurements on uncut, as-grown samples, i.e. 2-inch in diameter,
- The structural investigations were done before and after cutting the samples into $(5\times5)\,\mathrm{mm}^2$ pieces, and
- the optical and electrical measurements have been carried out only on $(5\times5)\,\mathrm{mm}^2$ in size, as-grown and post-annealed samples. Gold, sputtered through a shadow mask on the corners of the films, was used as ohmic contact to perform Hall-effect measurements (cf. figure 5.3).
- The post-annealing was performed on a selected number of samples and will be discussed in chapter 7. For this purpose, the samples have been post-annealed in vacuum. During the heat treatment processes, the temperature was kept at 400 °C.

Chapter 5

Characterization

5.1 Chemical Composition Analysis

5.1.1 Energy dispersive X-ray spectroscopy

In this work, thin films were deposited by PLD using a CCS method on 2-inch in diameter substrates that have a two-dimensional, lateral gradient of “Mg, Al”, or “Mg, Ga”. According to simulations [7], the films should have a gradient of Mg in one direction whereas a gradient of Al or Ga in a perpendicular direction. Experimentally, the lateral variation of chemical composition has been analyzed by energy dispersive X-ray

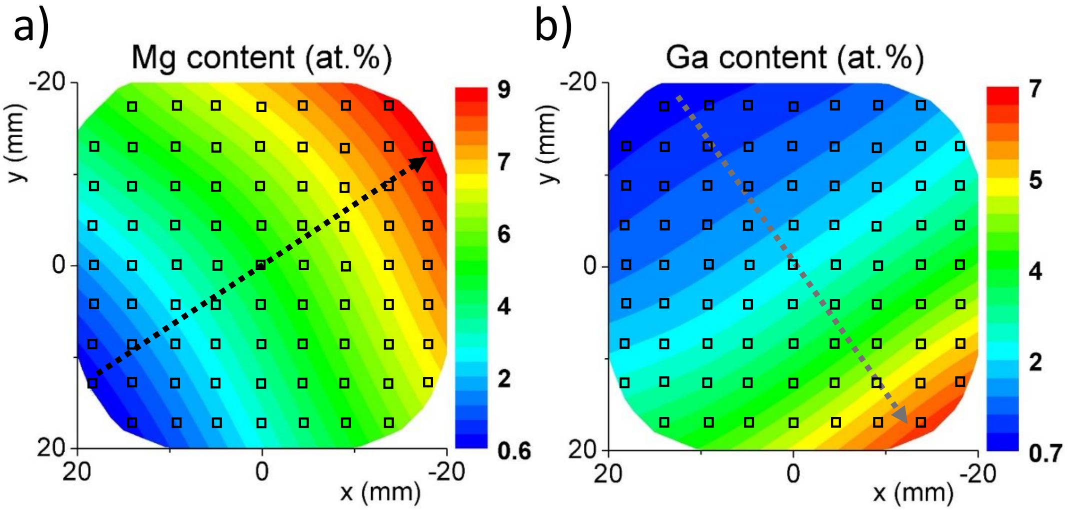

FIGURE 5.1: EDX mapping of Ga-doped (Mg,Zn)O wafer grown by PLD using the CCS method at 600 °C on *c*-plane sapphire substrate. Open rectangular shapes illustrate the 77 measurement points on the 2-inch in diameter substrate. The black and the gray arrows show the gradient direction of Mg and Ga, respectively.

spectroscopy (EDX, FEI NovaLab 200) with the detection limit of about 0.2 at.% for all impurities, i.e. Mg, Al and Ga.

Figure 5.1 depicts the EDX wafer mapping of a (Mg,Zn)O:Ga thin film. As shown in figure 5.1(b,c), the Mg-content is varied in one direction whereas the Ga-content is changing in the perpendicular direction that fulfills the prediction given in [7]. Furthermore, the similar lateral continuous composition gradients has been observed for the Al-doped (Mg,Zn)O thin films investigated in this work. The homogeneity of the material composition along the vertical direction of the films is discussed below.

5.1.2 Secondary Neutral Mass Spectrometry

The homogeneity of the material composition along the growth direction of the films might affect to the optical and electrical properties. Thus, the material composition in the direction perpendicular to the surface of the film has been investigated by Secondary Neutral Mass Spectrometry (SNMS) measurements on selected number of samples. The SNMS data were collected using the sputter voltage of 700 V and Ta mask with a diameter of 3 mm. Figure 5.2 depicts the SNMS data for (a) Al and (b) Ga-doped (Mg,Zn)O thin films grown at 200 °C on glass substrates using CCS method. It has been found that there is no composition gradient along the growth direction of the films.

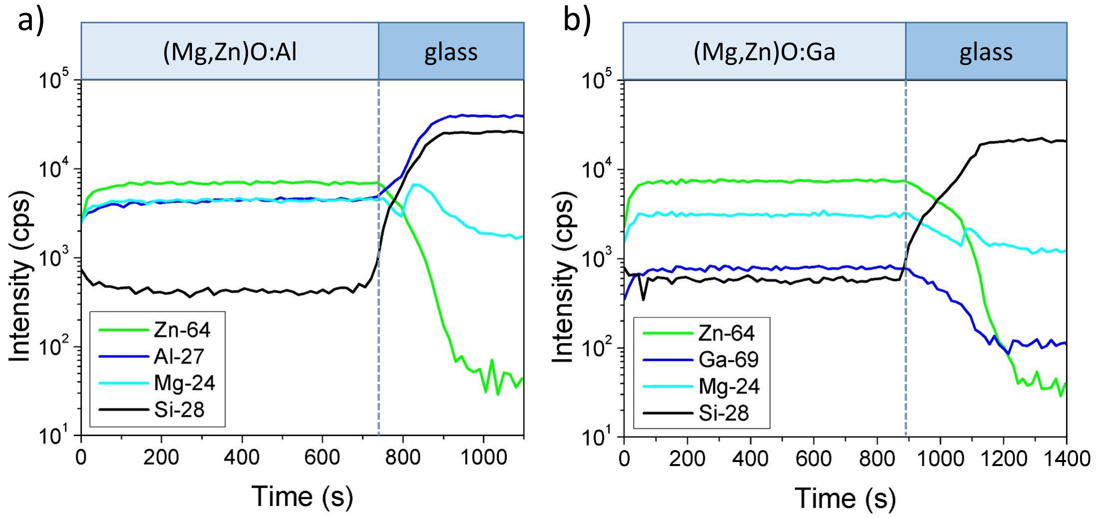

FIGURE 5.2: SNMS data of as-grown (a) Al- and (b) Ga-doped (Mg,Zn)O thin films grown at 200 °C on glass substrates. Data taken at the sputter voltage of 700 V using a Ta mask with a diamater of 3 mm.

5.2 Structure and Morphology Analysis

The crystalline quality of the films was investigated by X-ray diffraction line scans using (i) a PANalytical X'pert PRO MRD , and (ii) Philips X'pert diffractometers. The former has been used to investigate the as-grown, i.e. uncut, samples on 2-inch in diameter substrates. The letter one was mainly used to investigate the as-grown as well as post-annealed samples that have been cut into (5×5) mm^2 pieces, i.e. the samples discussed in chapter 6. For further details, the reader is referred to [38]. The surface morphology of selected samples was investigated by atomic force microscopy (AFM). All data presented in this work were collected at non-contact mode regime of the cantilever.

5.3 Electrical Properties Analysis

The electrical transport properties, i.e. free charge carrier density (n), mobility (μ), and resistivity (ρ), have been investigated by Hall-effect measurement at room temperature (RT) using van der Pauw method [142]. Hall-effect was first discovered by Edwin H. Hall in 1879 in thin gold leaf samples [143]. Nowadays, this method is widely used to investigate electrical properties of semiconductors. Van der Pauw described the requirements the sample geometry in 1958 [142]. He showed that almost all arbitrary shapes of the samples can be measured. The only requirements for accurate measurements are

- to know the thickness of the film or sample,
- to have a homogeneous, isotropic and flat sample and
- to make small contacts in comparison to the surface area.

In figure 5.3, a rectangle shape of the sample geometry used in this work is given. Here, a brief introduction for Hall-effect measurement on n-type samples will be discussed. Note that in the following equations the vector quantities are given as bold symbols. For more information, as well as for p-type samples, the reader is referred [143, 144].

If current $\mathbf{j}$ flows between contacts A and C (cf. figure 5.3) and a magnetic field $\mathbf{B}$ is applied perpendicular to the sample surface, the Lorenz force, $\mathbf{F}_L = -e[\mathbf{v}_d \times \mathbf{B}]$, deflects the electrons in the sample and introduces an electric field $\mathbf{E}_H$ between contacts B and D. In equilibrium, this electric field balances the Lorenz force:

$$-e[\mathbf{v}_d \times \mathbf{B}] - e\mathbf{E}_H = 0, \tag{5.1}$$

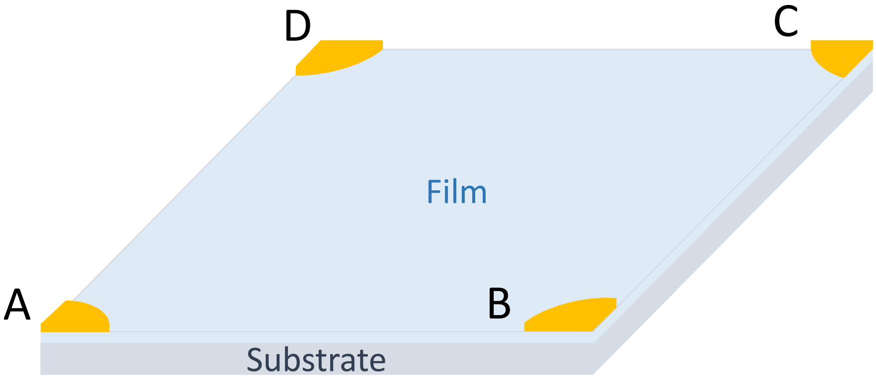

FIGURE 5.3: Sample geometry for Hall-effect measurements. The size of the samples is $5 \times 5\,\mathrm{mm}^2$. Gold was sputtered through a shadow mask on the corners of the samples, and used as ohmic contact.

or

$$-e(\frac{1}{en}\mathbf{j} \times \mathbf{B}) - e\mathbf{E}_H = 0, \tag{5.2}$$

where e is the elementary charge, $\mathbf{v}_d$ and n are the drift velocity and concentration of the electrons, and "$-$" sign is due to the negative charge of the electrons. An important quantity of this method is the Hall constant, R_{H}, which can be derived from the Hall field:

$$\mathbf{E}_H = -\frac{1}{en}\mathbf{jB} = R_{\mathrm{H}}\mathbf{jB} \tag{5.3}$$

$$R_{\mathrm{H}} = -\frac{1}{en}. \tag{5.4}$$

As discussed above, one can easily determine the conduction type of the semiconductor from the sign of the Hall constant, it is positive for p-type, and negative for n-type semiconductors. From the absolute value of R_{H}, free charge carrier density n can be derived. In Equation. 5.4, various scattering mechanisms of free charge carriers in semiconductors were neglected. In this case, The Hall constant also includes the Hall factor, r_{H}

$$R_{\mathrm{H}} = -\frac{r_{\mathrm{H}}}{en} \tag{5.5}$$

with

$$r_{\mathrm{H}} = \frac{\langle \tau_m^2 \rangle}{\langle \tau_m \rangle^2}, \tag{5.6}$$

where τ is the momentum relaxation time. The order of the magnitude of the r_{H} is 1. The Hall factor is set to one also in this work to evaluate RT measurements. The

Hall-effect are also combined with resistivity measurements using:

$$\mathbf{j} = \sigma \mathbf{E} = \rho^{-1} \mathbf{E}, \tag{5.7}$$

where σ is the electric conductivity. At the same time, the electric conductivity is related to the drift mobility, μ_d as following:

$$\sigma = \rho^{-1} = en\mu_d. \tag{5.8}$$

Solving the Equation. 5.8 for n, and substituting the result into Equation. 5.5, one obtains

$$r_{\mathrm{H}}\mu_d = \frac{R_{\mathrm{H}}}{\rho}, \tag{5.9}$$

or

$$\mu_H = \frac{R_{\mathrm{H}}}{\rho}, \tag{5.10}$$

where μ_H is the Hall mobility that is related with μ_d by

$$\mu_H = r_{\mathrm{H}}\mu_d. \tag{5.11}$$

It is also possible to perform temperature dependent Hall measurements (TdH) in the range of 35 K to 300 K using the same setup. As all films investigated are in degenerate state with high density of extrinsic donor impurities, TdH measurements have only been performed on selected samples in order to check and confirm the degenerate state of the films.

5.4 Optical Properties Analysis

As discussed in chapter 3, the most important goal is determining the relevant optical properties of TCOs, i.e. the plasma frequency ω_{p} and the optical bandgap energy E_{g}. In this work, m_{e}^* and ω_{p} have been determined using infrared spectroscopic ellipsometry measurements (IRVASE, J. A. Woollam Co.). In general, ellipsometry investigates the relative amplitude and phase change of a differently polarized light upon reflection at a sample surface. Using the model analysis of the experimental data, the model dielectric function (DF) and the film thicknesses have been extracted. From the model, the plasma frequency as well as the effective electron mass have been obtained from the DFs. The optical bandgap of the films is obtained from Tauc plots of transmission data and confirmed by the spectroscopic ellipsometry (SE) measurements (VASE, J. A. Woollam Co.).

The SE measurements and analysis have been performed by S. Richter, whereas the transmission and reflection measurements have been done by U. Teschner (all Universität Leipzig).

5.4.1 Thickness Determination

The thickness d is one of the important parameters of the films, since its accuracy plays a major role to determine the Hall constant R_{H}, n, and ρ. The thickness of the films was mainly determined using spectroscopic ellipsometry measurements and confirmed by SEM cross section images. The investigated films have thicknesses ranging from 120 to 200 nm. The thickness variation across the 2 inch in diameter wafers was $(20-30)$ nm, i.e. $< 20\%$ of the maximal thickness obtained in the center of the thin films matching quite well with simulated values for thickness variation of 16% for a distance l, i.e. $l = 20$ mm, between the normals on the centers of the target and the substrate (cf. figure 4.2) [7]. Thus, the thickness of the films has been investigated using spectroscopic ellipsometry (M2000) measurements, and confirmed by several method, such as scanning electron microscopy (SEM), 3D laser scanning microscope, and Dektak.

Chapter 6

Doping Efficiency and Limits in As-grown (Mg,Zn)O:Al and (Mg,Zn)O:Ga Thin Films

In this chapter, the structural, electrical, and optical properties of $\mathrm{Mg}_x\mathrm{Zn}_{1-x}\mathrm{O}$:Al/Ga thin films are discussed. The samples have been grown at $T_\mathrm{g} = 600\,^\circ\mathrm{C}$ on 2-inch in diameter *c*-plane sapphire substrate using PLD. For detailed information on the sample preparation, the reader is referred to chapter 4.

6.1 Structural Properties

First, XRD measurements have been evaluated for the thin films located at the center of 2-inch in diameter CCS wafers that have a fixed alloy as well as dopant composition. Figure 6.1 shows the wide-angle $2\Theta - \omega$ scans in the range of 10 to 160° for Al and Ga doped (~ 2.5 at.% determined by EDX) $\mathrm{Mg}_{0.05}\mathrm{Zn}_{0.95}\mathrm{O}$ films grown on *c*-plane sapphire substrates. This thin films have a similar thickness of about 195 nm and 185 nm, respectively. It has been found that both films are crystalline with *c*-axis orientation since the XRD data shows only (00.2), (00.4) and (00.6) diffraction peaks. This orientation was also observed for the thin films deposited on a similar substrate by different growth methods e.g. magnetron sputtering [124]. No diffraction from other phases (e.g., Zn, Ga, Al, and $\mathrm{ZnAl_2O_4}$) was detected. Furthermore, the high crystalline quality of films can be seen by comparing the intensity of the diffraction peaks of film and substrate, i.e. (00.2) reflection of the ZnO vs. (00.6) reflex of the $\mathrm{Al_2O_3}$. For both, Al and Ga-doped samples, the (00.2) peak position is found to be at 34.468° and 34.465°, respectively. These values are higher than the values observed in binary ZnO, i.e. 34.419° [96]. This can be

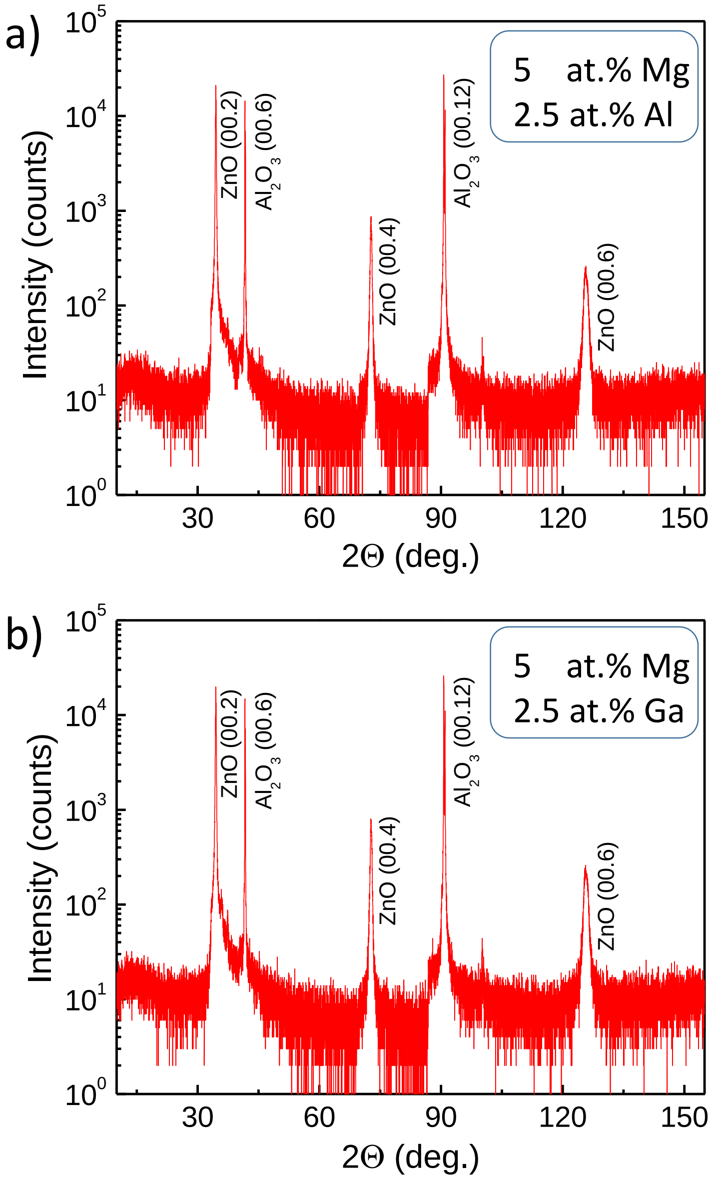

Figure 6.1: XRD wide-angle $2\Theta - \omega$ scans for (a) Al and (b) Ga doped $Mg_xZn_{1-x}O$ thin films with a doping concentration of about ~ 2.5 at.%, i.e located at the center of CCS wafers.

explained by incorporation of Mg resulting in a decrease of the *c*-lattice constant [101]. Further, the grain size of these films has been found to be about 60 nm along the growth direction, i.e. determined using the Debye-Scherrer formula (cf. equation 6.1).

Subsequently, XRD measurements have been performed around the (00.2) diffraction peak for all area of the (Mg,Zn)O:Al and (Mg,Zn)O:Ga thin films grown on a 2-inch in diameter wafers in order to investigate the influence of alloying (Mg) and doping (Al/Ga) contents on the structural properties. Figure 6.2 a) depicts the XRD peak position of the (00.2) diffraction peak as a wafer map for (Mg,Zn)O:Al thin film. As observed above, the

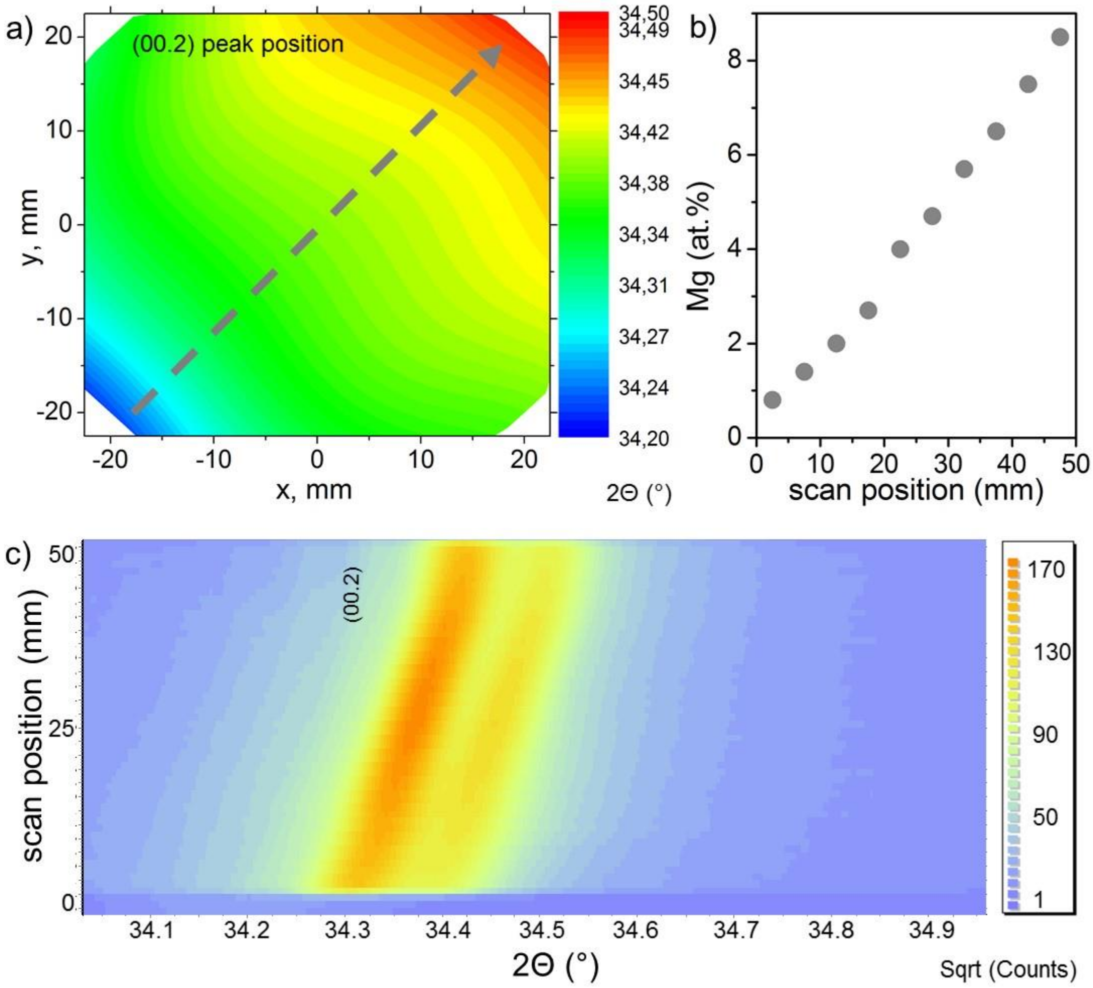

FIGURE 6.2: (a) Variation of (00.2) peak position of (Mg,Zn)O:Al thin films on a 2-inch in diameter *c*-plane sapphire substrate. The dashed gray arrow indicates the increasing direction of the Mg content which is shown in (b) whereas (c) depicts the corresponding line-scan for this (00.2) reflection peak. Note that the film has a constant Al content of about 1.5 at.% along the scanned line.

peak position has shifted to higher angles with increasing Mg content, i.e. determined by EDX (cf. chapter 5), which is indicated by the *dashed arrow*. Interestingly, the peak position is almost independent of the Al content (cf. a direction perpendicular to *dashed arrow* in figure 6.2 a). Figure 6.2 b) shows the increase of the Mg content along the XRD line-scan given in figure 6.2 c). It is also obvious from the figure that the position of the (00.2) diffraction peak systematically increases with increasing Mg content along a line of approximately constant dopant concentration of about 1.5 at.%.

In figure 6.3, XRD $2\Theta - \omega$ data are depicted as a function of Al and Ga concentrations, i.e. determined from EDX measurements, in the range of (32-37.5)° for the $Mg_xZn_{1-x}O$:(Al/Ga) thin films that have a fixed alloy composition of $x = 0.04$. As

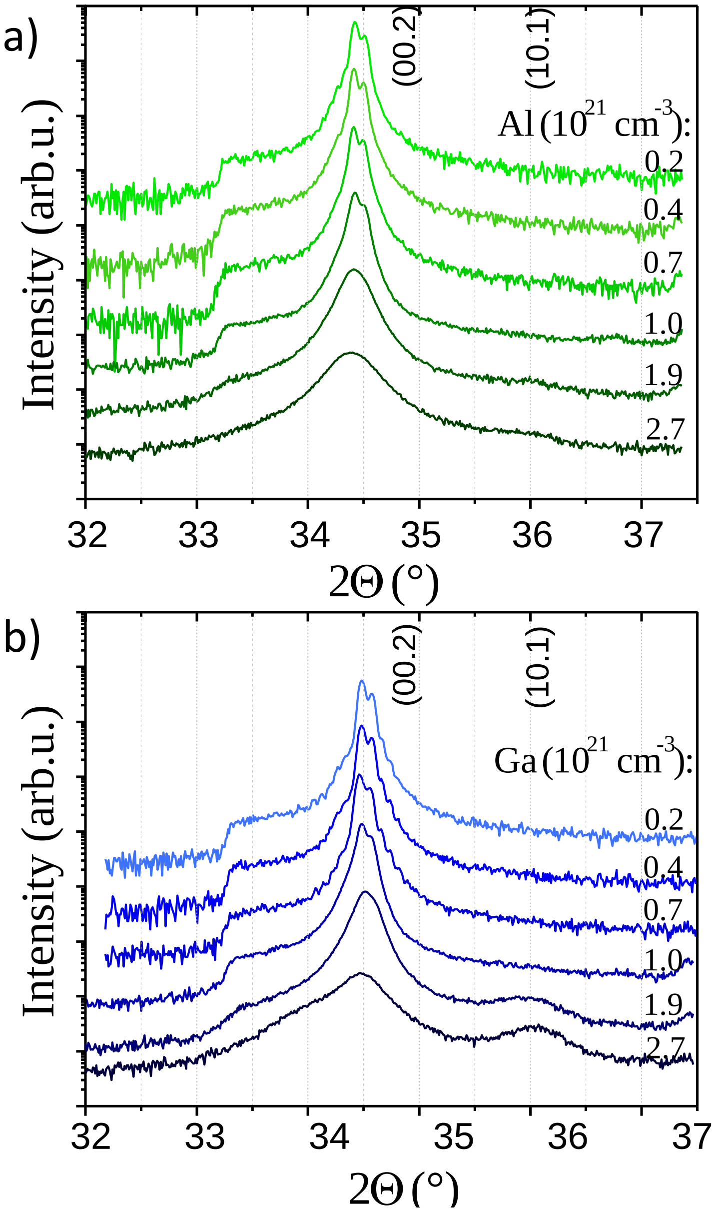

FIGURE 6.3: Selected XRD $2\Theta - \omega$ scans around the (00.2) reflection for Al (a) and Ga (b) doped $Mg_{0.04}Zn_{0.94}O$:(Al/Ga) films at different Al/Ga doping levels.

visible in the figure both dopants lead to a (00.2) diffraction peak at around 34.5°. Interestingly, at higher doping concentrations an additional (10.1) oriented phase of ZnO appears in the symmetric $2\Theta - \omega$ scans, which is more obvious in the case of Ga doping (cf. figure 6.3 b). Furthermore, in both doping series the intensity of the (00.2) diffraction peak tends to decrease with increasing doping content. In order to look deeper into this behavior, the full width at half maximum (FWHM) of the (00.2) diffraction peaks has been further analyzed. For this, the FWHM values were corrected by subtracting the instrumental width (0.025°) of the diffractometer which was obtained by measuring a high quality ZnO *c*-plane single crystal. Figure 6.4 a) depicts the FWHM of the (00.2)

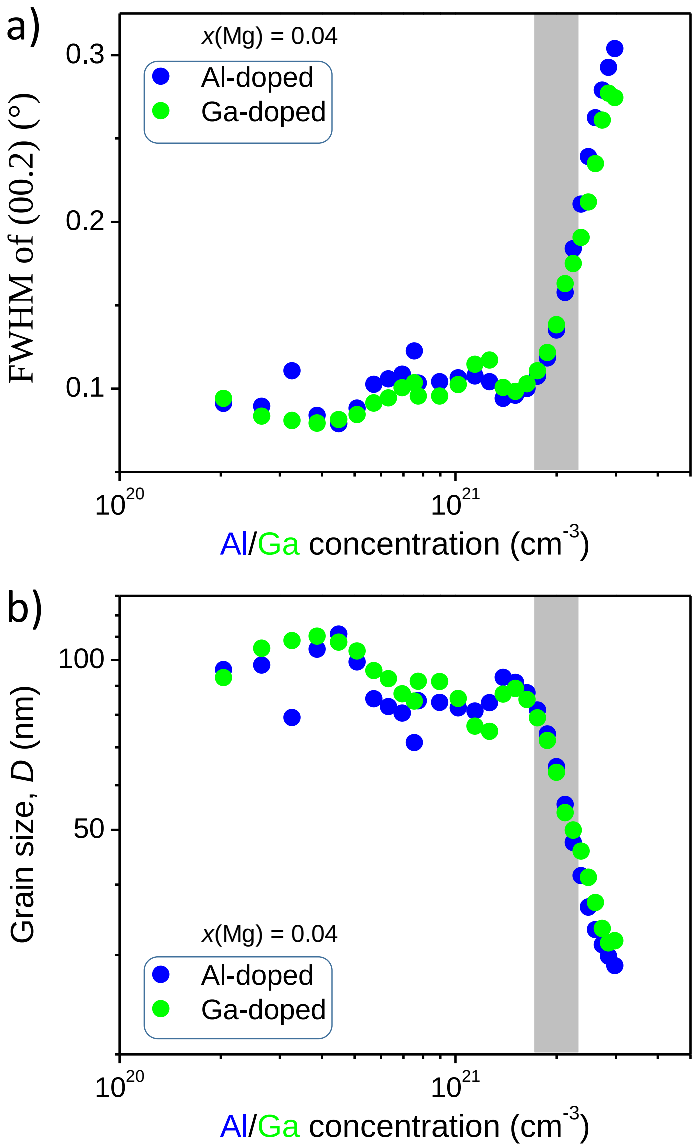

FIGURE 6.4: (a) FWHM of (00.2) peaks and (b) estimated grain size (along the growth direction) of $Mg_{0.04}Zn_{0.96}O$:(Al/Ga) films as a function of Al or Ga content. The gray area indicates the critical dopant concentration of $N_d \approx 2 \times 10^{21}$ cm^{-3} from which on the structural disorder increases rapidly.

diffraction peaks of $Mg_xZn_{1-x}O$:(Al/Ga) thin films for different Al and Ga content along a line of approximately constant alloy content of $x = 0.04$. Regardless of the dopant element, the FWHM is for low doping levels almost independent of the Al/Ga concentration, with values in the range of $(0.1 - 0.14)^\circ$, which is comparable to the reported values of binary ZnO (0.12°) and (Mg,Zn)O (0.13°) thin films prepared by PLD [101]. On the other hand, the FWHM values tend to increase above a certain critical dopant content of $N_d \sim 2 \times 10^{21}$ cm^{-3}. Furthermore, the grain size D of these films (along the growth direction) was estimated using Debye-Scherrer formula:

$$D = \frac{0.94 \cdot \lambda}{B \cdot \cos(\Theta)} \tag{6.1}$$

where λ ($= 0.154\,\mathrm{nm}$) is the wavelength of the X-rays, B is the width of the peak and 2Θ is the angle between incident and scattered wave. A minimum grain size of 70 nm has been obtained for all samples that have a dopant content of $N_\mathrm{d} < 2 \times 10^{21}\,\mathrm{cm}^{-3}$, and a clearly decreasing trend at higher dopant concentrations (cf. figure 6.4 b). An increase of the peak width with increasing Al concentration has also been observed in doped (Mg,Zn)O [27] as well as ZnO [145] and explained by a decreasing grain size that is consistent with our experimental results.

6.2 Electrical Properties

In this section, the electrical properties of $\mathrm{Mg}_x\mathrm{Zn}_{1-x}\mathrm{O}$:(Al/Ga) thin films are discussed that have been obtained using Hall-effect measurements at RT.

In figure 6.5, the dependence of the free charge carrier (electron) concentration n versus the chemical dopant concentration N_d is plotted for different Mg admixtures. Independent of the dopant element, i.e. Al or Ga, an increase of n up to a dopant concentration of $1 \times 10^{21}\,\mathrm{cm}^{-3}$, then a saturation and finally a decrease of n for $N_\mathrm{d} > 2 \times 10^{21}\,\mathrm{cm}^{-3}$ has been observed. One further notices that the free electron density is especially for higher Mg admixture clearly lower than N_d. Low dopant activation $N_\mathrm{d,act} = n/N_\mathrm{d}$ was also found by Bikowski *et al.* for $\mathrm{Mg}_{1-x}\mathrm{Zn}_x\mathrm{O}$:Al thin films grown at substrate temperatures of $(200-500)$°C (x is about 0.1); only about 1 to at most 23 % of the incorporated Al was contributing free electrons [124]. Despite the low dopant activation, distinct dependencies of the free charge carrier concentration on the dopant content have been observed. The trend described in the following holds for the Ga doping series and also for the Al doping series with 7 at.% Mg admixture. The two Al doping series with lower Mg content are considered below. For lower dopant concentration the free carrier concentration increases linearly with N_d ($n \propto N_\mathrm{d}$). This is rather surprising since it implies that if we start with dopant content of $2 \times 10^{20}\,\mathrm{cm}^{-3}$ the corresponding free charge carrier density of $(3-4) \times 10^{19}\,\mathrm{cm}^{-3}$ also increases linearly with a slope of one. This indicates that the doping efficiency remains constant in this doping regime (cf. figure 6.6). An explanation for this could be that sinks for the dopants such as grain boundaries are saturated. This means that in this regime $N_\mathrm{d,act}$ increases slightly (visible best for the Ga doping series, cf. figure 6.6 b). A more general formulation is that the doping efficiency is a function of the dopant concentration as it is evident from literature data of free charge carrier

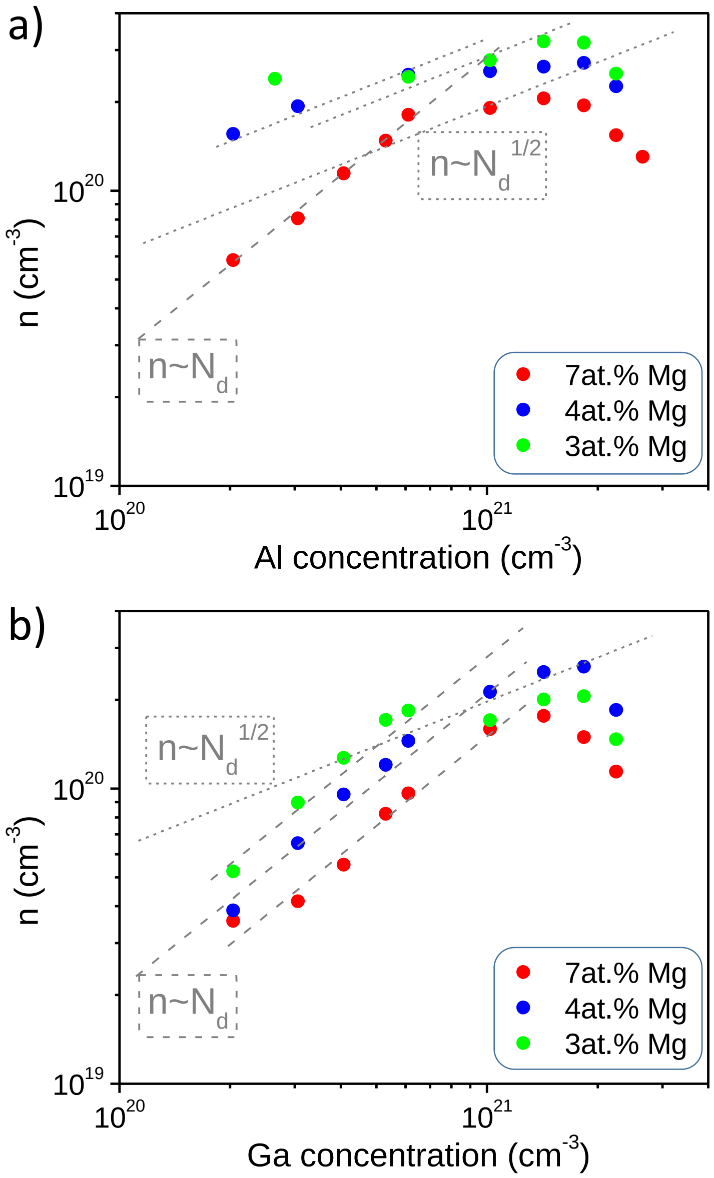

FIGURE 6.5: Dependence of the free electron concentration n on the (a) Al and (b) Ga dopant concentration N_d. Dashed lines indicate linear and dotted lines a square root dependence of n on the dopant concentration N_d.

concentration versus dopant concentration [89, 94, 146]. For higher dopant concentration up to $N_\mathrm{d} \sim 1.4 \times 10^{21}\,\mathrm{cm}^{-3}$ the increase of n with increasing N_d becomes weaker and tends more to a $n \propto {N_\mathrm{d}}^{1/2}$ behavior. Different sources for doping limitations have been discussed in the literature such as the formation of secondary phases [147] or defect complexes [148], or the formation of compensating intrinsic defects explained within the amphoteric defect model [130, 131]. In the case of ZnO or (Mg,Zn)O the main intrinsic defect forming at high n-type doping levels is the zinc vacancy (V_Zn) [115, 149–152],

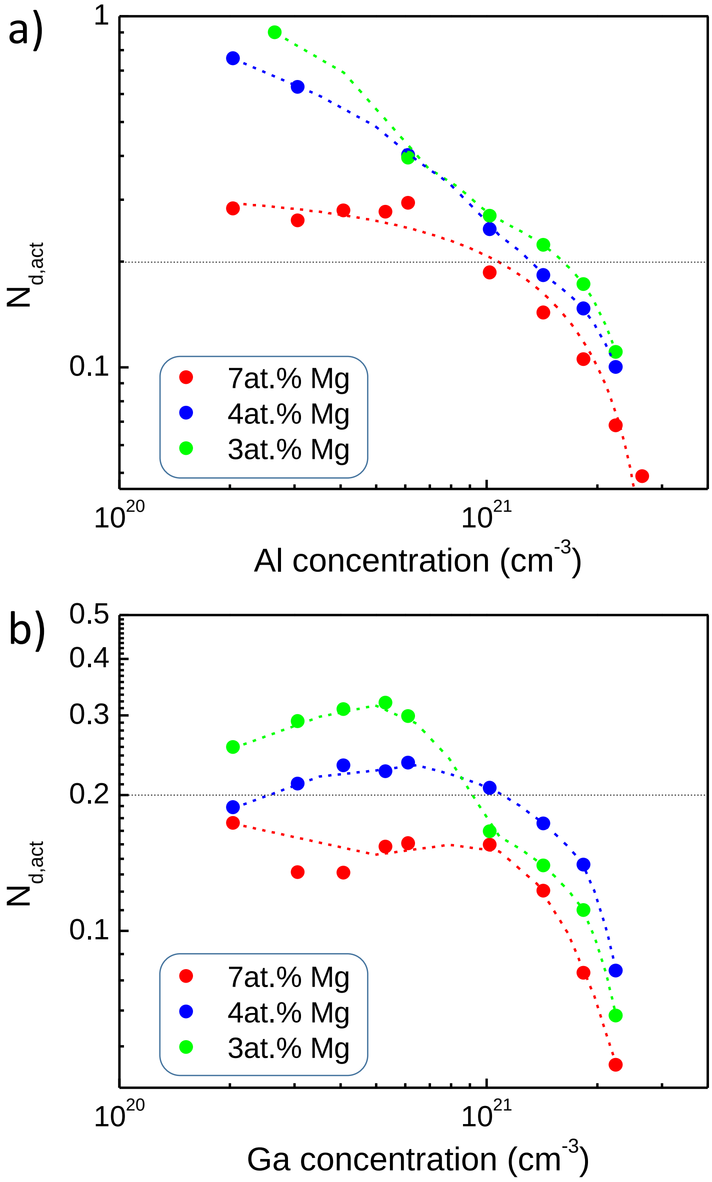

FIGURE 6.6: Dependence of the doping efficiency $N_{\mathrm{d,act}}$ on the (a) Al and (b) Ga dopant concentration N_{d}. Dashed lines are spline approximations of the data to guide the eye. The vertical dotted line indicates $N_{\mathrm{d,act}} = 0.2$.

indeed a doubly chargeable acceptor in ZnO [110] or other defects such as oxygen interstitials. Thus, the free charge carrier concentration can then be described in two ways [8, 130]:

$$n = N_{\mathrm{d}} - qN_{\mathrm{V}_{\mathrm{Zn}}^{2-}} = N_{\mathrm{c}} F_{1/2}\left(\frac{E_{\mathrm{F}} - E_{\mathrm{c}}}{kT}\right). \tag{6.2}$$

where q is the charge state of the compensating defect, $F_{1/2}$ is the Fermi integral, N_{c} and E_{c} are the conduction band density of states (DOS) and the energy of the conduction band minimum (CBM), respectively. $N_{\mathrm{V}_{\mathrm{Zn}}^{2-}}$ is expressed according to ADM as:

$$N_{\mathrm{V}_{\mathrm{Zn}}^{2-}} = \hat{N}_0 \mathrm{exp}\left(+q\frac{E_{\mathrm{F}}}{kT}\right). \tag{6.3}$$

with $q = 2$, $\hat{N}_0 = N_{\mathrm{sites}}\mathrm{exp}(-2E_{\mathrm{FS}} + H)$, N_{sites} is the density of possible lattice sites for the zinc vacancy (about $4.1 \times 10^{22}\,\mathrm{cm}^{-3}$ in wurtzite ZnO), E_{FS} is the stabilized Fermi level and H is the defect formation enthalpy. Putting equation 6.3 into equation 6.2 by substituting E_{F} one can obtain

$$n = N_{\mathrm{c}} F_{1/2}\left(\frac{1}{2}\ln\frac{N_{\mathrm{V}_{\mathrm{Zn}}^{2-}}}{\hat{N}_0} - \frac{E_{\mathrm{c}}}{kT}\right), \tag{6.4}$$

or approximately

$$n \approx N_{\mathrm{c}} \mathrm{exp}\left(\frac{1}{2}\ln\frac{N_{\mathrm{V}_{\mathrm{Zn}}^{2-}}}{\hat{N}_0} - \frac{E_{\mathrm{c}}}{kT}\right) =: \mathrm{C} N_{\mathrm{V}_{\mathrm{Zn}}^{2-}}^{1/2} \tag{6.5}$$

with a constant C. Finally as $N_{\mathrm{V}_{\mathrm{Zn}}^{2-}} \propto N_{\mathrm{d}}$, we obtain $n \propto {N_{\mathrm{d}}}^{1/2}$.

For the $\mathrm{Mg}_{0.04}\mathrm{Zn}_{0.96}\mathrm{O}$:Al series only the second regime, $n \propto {N_{\mathrm{d}}}^{1/2}$ is visible and it is shifted to lower dopant density. However, the free charge carrier concentration n for any N_{d} is higher than that of the $\mathrm{Mg}_{0.07}\mathrm{Zn}_{0.93}\mathrm{O}$:Al series and hence the maximal dopant activation is with about 60 % higher as well. For the $\mathrm{Mg}_{0.03}\mathrm{Zn}_{0.97}\mathrm{O}$:Al series neither linear ($n \propto N_{\mathrm{d}}$) nor square root ($n \propto {N_{\mathrm{d}}}^{1/2}$) regimes are visible. Presumably, these regimes are further shifted to lower dopant concentrations due to higher dopant activation for lower Mg content. This is also clear in the resistivity plot (cf. figure 6.9) where the lowest resistivity values are reached and saturated at lower dopant concentration for the $\mathrm{Mg}_{0.03}\mathrm{Zn}_{0.97}\mathrm{O}$:Al series. However, the free charge carrier concentration is for any N_{d} the highest among the (Mg,Zn)O:Al series. This implies that also the dopant activation is highest for this series as can be seen in figure 6.6 a), showing $N_{\mathrm{d,act}}$ for the (Mg,Zn)O:Al samples. For the growth parameters used, the dopant activation is higher in the Al doping series in comparison to the Ga doping series. In the literature, however, also the opposite case was reported [153]. On this issue, further experiments are needed for clarification. As a general trend, the dopant activation decreases with increasing Mg-content. Furthermore, it decreases strongly for all three Mg-contents for dopant content $N_{\mathrm{d}} > 6 \times 10^{20}\,\mathrm{cm}^{-3}$ where self-compensation becomes more and more important. Additionally, at higher doping levels of $N_{\mathrm{d}} > 2 \times 10^{21}\,\mathrm{cm}^{-3}$ $N_{\mathrm{d,act}}$ decreases rapidly. The (Mg,Zn)O:Ga series have depicted a more systematic dependence of the free carrier density on the Mg-content for a given N_{d}. The three dopant series are ordered from higher to lower free carrier concentrations for an increasing Mg-content. About 20 % of the incorporated Ga-atoms contribute free charge carriers (cf. figure 6.6 b). A slight increase of $N_{\mathrm{d,act}}$ with increasing N_{d} ($N_{\mathrm{d}} < 6 \times 10^{20}\,\mathrm{cm}^{-3}$) is found for all Mg series. Similar to

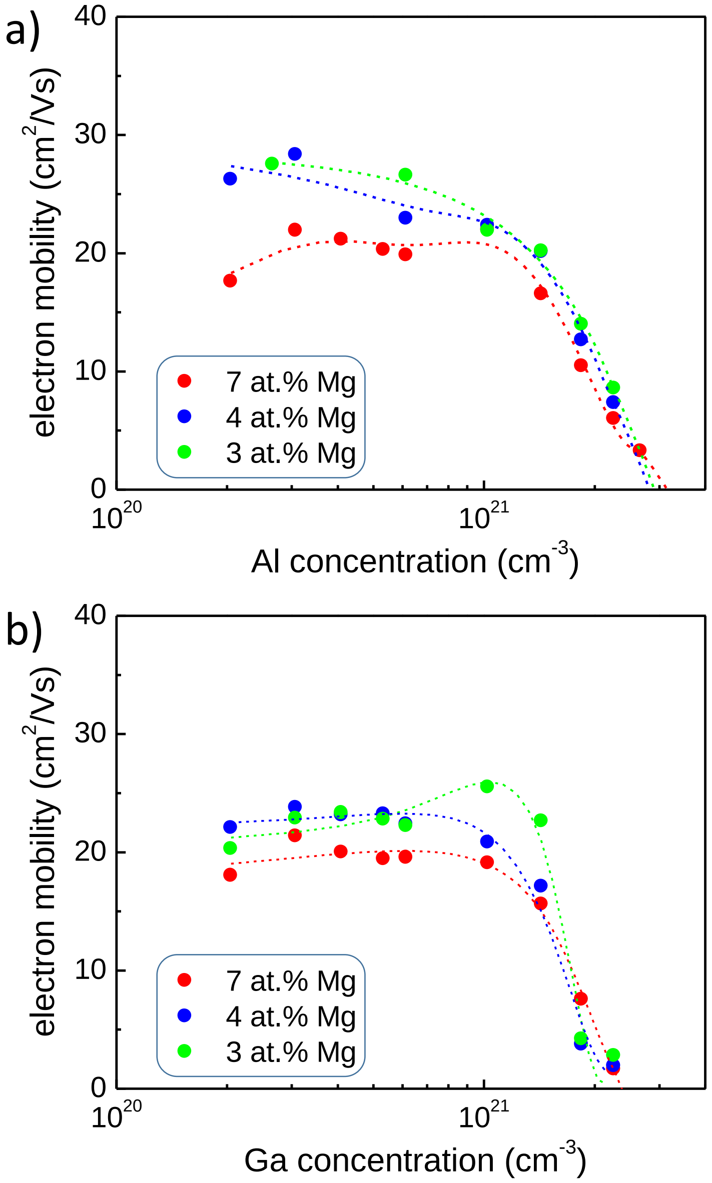

Figure 6.7: Dependence of the electron mobility on (a) the Al and (b) Ga dopant concentration. The spline approximations of the data to guide the eye.

the Al-doped samples the dopant activation decreases clearly for $N_\mathrm{d} \approx 6 \times 10^{20}\,\mathrm{cm}^{-3}$ and even stronger for $N_\mathrm{d} > 1 \times 10^{21}\,\mathrm{cm}^{-3}$. For the $\mathrm{Mg}_x\mathrm{Zn}_{1-x}\mathrm{O}$:Ga series the dependence of the free charge carrier concentration on N_d is linear up to $N_\mathrm{d} \sim 7 \times 10^{20}\,\mathrm{cm}^{-3}$, i.e. $n \sim 1 \times 10^{20}\,\mathrm{cm}^{-3}$. This is in principle the same limiting dopant concentration as it has been found for the Al doping series. However, a regime with $n \sim {N_\mathrm{d}}^{1/2}$ is only clearly visible for the $\mathrm{Mg}_x\mathrm{Zn}_{1-x}\mathrm{O}$:Ga series with $x = 0.04$. As guide to the eye, the lines having an $n \sim {N_\mathrm{d}}^{1/2}$ dependence have been plotted in figure 6.5.

The dependence of the electron mobility determined by Hall measurements on the dopant concentration is depicted in figure 6.7. Highest mobility exceeding $25\,\mathrm{cm}^2/\mathrm{Vs}$

is observed for low Mg-contents. For both dopant series a weak dependence of the mobility on doping level is found for dopant concentrations up to $10^{21}\,\mathrm{cm}^{-3}$. In contrast, a strong decrease of the mobility is found for dopant concentrations higher than $10^{21}\,\mathrm{cm}^{-3}$. This coincides with the dopant concentration above, with which the incorporation of compensating acceptors, most likely zinc vacancies, is strongly enhanced. So it is reasonable to conclude a transition from grain boundary to ionized impurity scattering being the dominant scattering process. This is supported by taking a closer look to those series with comparatively low free electron concentration ($\mathrm{Mg_{0.07}Zn_{0.93}O}$:Al, $\mathrm{Mg_{0.07}Zn_{0.93}O}$:Ga, $\mathrm{Mg_{0.04}Zn_{0.96}O}$:Ga, $\mathrm{Mg_{0.03}Zn_{0.97}O}$:Ga) for which the free carrier mobility increases or remains constant with increasing N_d in the lower doping regime. This is due to enhanced screening of and a decreased depletion region around the grain boundaries. If the dopant concentration is increased further, the density of ionized impurities increases first linearly with it. But as soon as self-compensation starts to determine the free charge carrier concentration as it is the case for $N_\mathrm{d} > 10^{21}\,\mathrm{cm}^{-3}$ a strong decrease of the mobility is observed. This is also corresponding to the transition observed in the XRD data ($N_\mathrm{d} \sim 10^{21}\,\mathrm{cm}^{-3}$, in figure 6.3), the FWHM increases strongly which fits to the argument that more and more zinc vacancies are incorporated.

In figure 6.8, the Hall mobility is plotted as a function of the free charge carrier density. As discussed above, in the doping series that exhibit comparatively low free charge carrier concentration, i.e. $\mathrm{Mg_{0.07}Zn_{0.93}O}$:Al, $\mathrm{Mg_{0.07}Zn_{0.93}O}$:Ga, $\mathrm{Mg_{0.04}Zn_{0.96}O}$:Ga and $\mathrm{Mg_{0.03}Zn_{0.97}O}$:Ga, the free carrier mobility showed a weak dependence on the free charge carrier concentration along the increasing direction of dopant content N_d until free charge carrier density reaches a value of $n \sim 1 \times 10^{20}\,\mathrm{cm}^{-3}$. As soon as n reaches this value, the mobility drops significantly with increasing dopant content supporting the fact that the ionized impurity scattering becomes more and more dominant due to an increased number of (i) dopants as well as (ii) acceptor like self-compensating defects. In Al-doping series with high doping efficiency, i.e. $\mathrm{Mg_{0.03}Zn_{0.97}O}$:Al and $\mathrm{Mg_{0.04}Zn_{0.96}O}$:Al, the mobility only drops with increasing doping level as these films already have a high free charge carrier density of $n \sim 1 \times 10^{20}\,\mathrm{cm}^{-3}$, thus additional dopants not only contribute to create free charge carriers but also acceptor-like defects that compensate free electrons and act as ionized impurity scattering centers.

Figure 6.9 illustrates the resistivity of Al- and Ga-doped $\mathrm{Mg}_x\mathrm{Zn}_{1-x}\mathrm{O}$ alloys as a function of Al and Ga concentration for indicated Mg-admixtures. The resistivity being the inverse product of the elementary charge e, the free charge carrier density n and the mobility μ (cf. equation 5.8), also depicts a distinct dependence on the doping levels.

In the doping series that have comparatively low free charge carrier density, that are

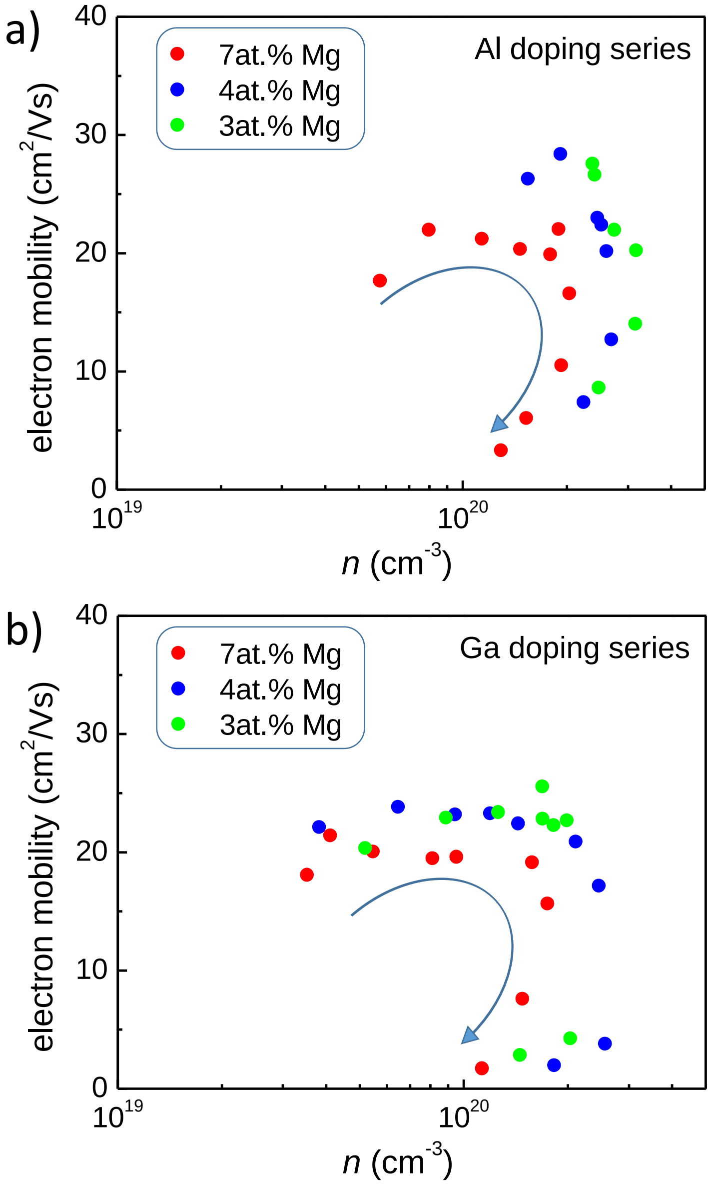

FIGURE 6.8: Dependence of the electron mobility on the free carrier density for (a) Al- and (b) Ga doped $Mg_xZn_{1-x}O$ films. The arrows indicate the increasing direction of dopant concentration.

$Mg_{0.07}Zn_{0.93}O$:Al, $Mg_{0.07}Zn_{0.93}O$:Ga, $Mg_{0.04}Zn_{0.96}O$:Ga, $Mg_{0.03}Zn_{0.97}O$:Ga, the resistivity decreases with increasing doping content up to $N_\mathrm{d} \sim 10^{21}\,\mathrm{cm}^{-3}$ mainly due to the contribution of the free charge carrier densities but not the mobility. Therefore, in two Al-doping series with high free charge carrier density, i.e. $Mg_{0.03}Zn_{0.97}O$:Al and $Mg_{0.04}Zn_{0.96}O$:Al, the resistivity shows a saturation in a certain range due to the saturation of the free charge carrier concentration. Above this doping level of $N_\mathrm{d} > 10^{21}\,\mathrm{cm}^{-3}$, the resistivity of all doping series strongly increases due to the contribution of both n and μ (cf. figure 6.5 and figure 6.7). Here, the Al dopant series reached the lowest

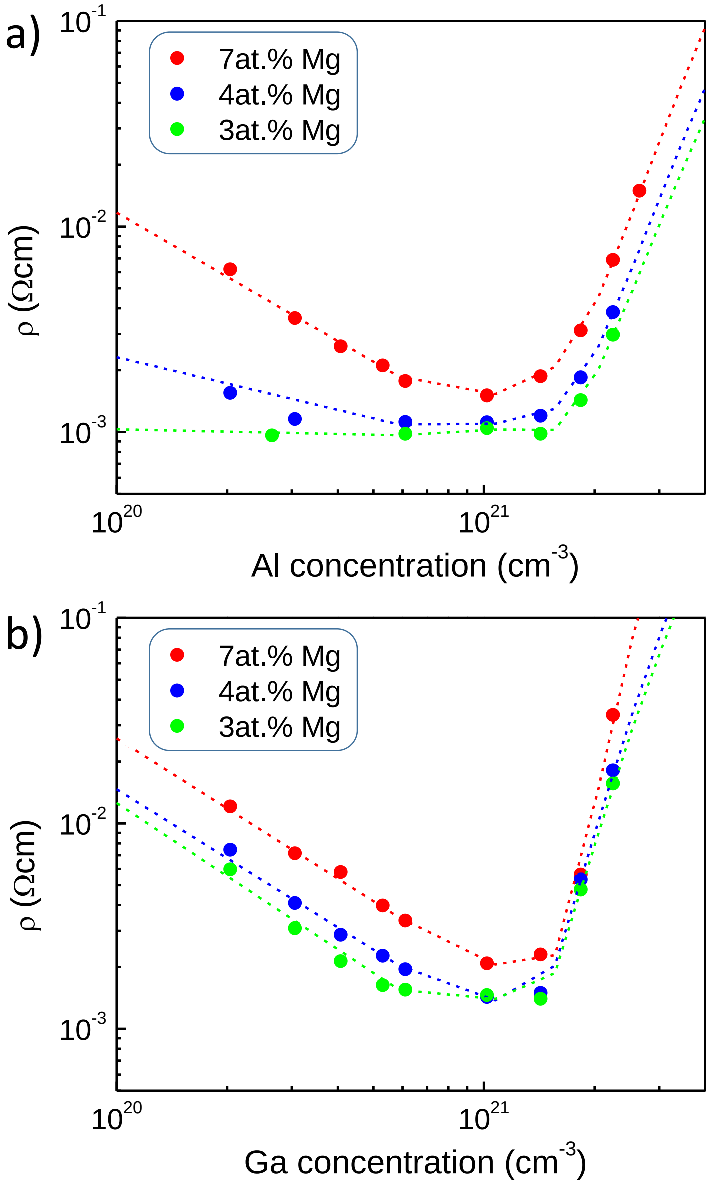

FIGURE 6.9: Resistivity of $Mg_xZn_{1-x}O$:(Al/Ga) thin films as a function of (a) Al and (b) Ga dopant concentration N_d. Dashed lines are spline approximations of the data to guide the eye.

resistivity ($1 \times 10^{-3}\,\Omega$cm) at lower doping densities due to a higher doping activation than in Ga dopant series ($2 \times 10^{-3}\,\Omega$cm).

6.3 Optical Properties

6.3.1 Optical Bandgap

Figure 6.10 depicts the optical bandgap energy of Al and Ga-doped wurtzite $Mg_xZn_{1-x}O$ alloys as a function of the dopant concentration. In both doping series, for a given dopant concentration the optical bandgap is higher for the films with higher Mg content as expected: Mg increases the bandgap of ZnO [23]. Similar to the electrical transport

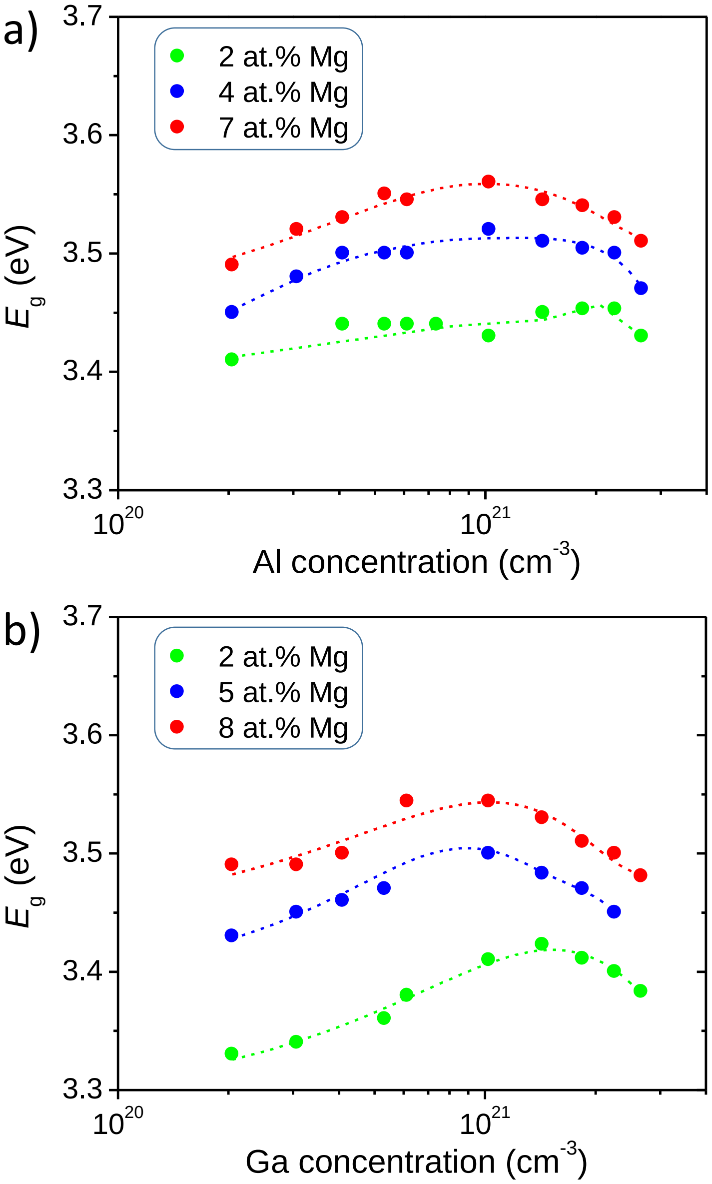

Figure 6.10: Optical bandgap energies of $Mg_xZn_{1-x}O$:(Al/Ga) films versus (a) Al and (b) Ga concentration. The bandgap was obtained by transmission data using the Tauc plot. The dashed lines are the spline approximations of the data to guide the eye.

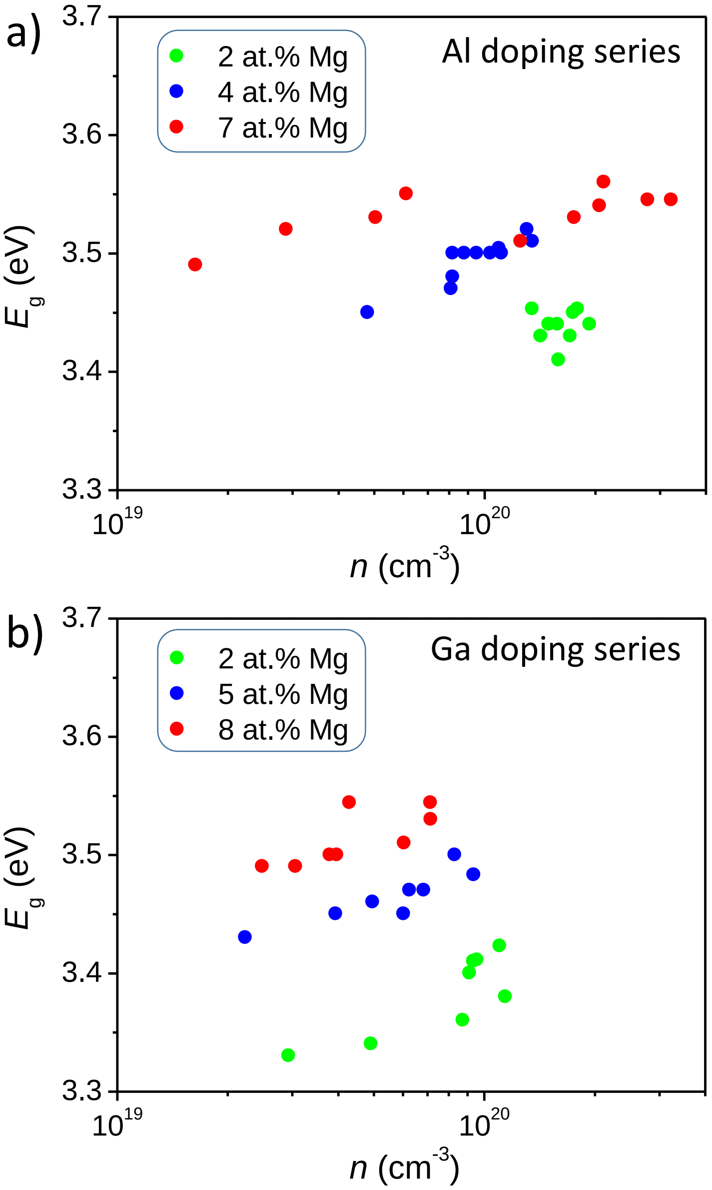

FIGURE 6.11: Optical bandgap energies of $Mg_xZn_{1-x}O$:(Al/Ga) thin films as a function of the free charge carrier density for (a) Al- and (b) Ga-doped $Mg_xZn_{1-x}O$ films.

properties discussed in the previous section, the optical bandgap first increases with increasing doping content up to $N_d \sim 10^{21}\,\mathrm{cm}^{-3}$. At higher doping levels of $N_d > 10^{21}\,\mathrm{cm}^{-3}$, the optical bandgap tends to decrease with increasing dopant concentration. Furthermore, for a given (similar) Mg-content, the optical bandgap shows a higher blue shift for the Al-doping series in comparison to the Ga-doping series and coincides with the dependency of the free charge carrier density on the dopant concentration (cf. figure 6.5). Hence, it is reasonable to conclude that these changes in the optical bandgap are mainly due to the contribution of the free charge carriers and can be explained by the Burstein-Moss (BM) shift. However, for calculating the BM shift, not only the free charge carrier density, but also the reduced mass (or the effective electron mass) has to be considered which is discussed below.

In figure 6.11, the optical bandgap versus the free charge carrier density is plotted for the $\mathrm{Mg}_x\mathrm{Zn}_{1-x}\mathrm{O}$:(Al/Ga) thin films. In both doping series, the optical bandgap changes as a function of the free charge carrier density as well as the Mg content x. The discussion given in the following holds for the Ga doping series. The Al doping series are discussed further below. Independent of the free charge carrier density, the samples with higher Mg-admixtures depicted higher optical bandgap. Furthermore, the optical bandgap increases with increasing the free charge carrier density. With increasing Mg content, the influence of the free charge carrier dependent BM shift on the optical bandgap of the films systematically decreases, being 0.09 eV, 0.07 eV, and 0.05 eV for respective Mg-admixtures of $x = 0.02$, $x = 0.05$, and $x = 0.08$. Furthermore, it has been found that the free charge carrier density decreases with increasing Mg content which might be due to the increased dopant activation energy at higher Mg-admixtures or the solubility limit of the impurities [23]. In Al-doped $\mathrm{Mg}_{0.02}\mathrm{Zn}_{0.98}\mathrm{O}$ alloys, the dependence of the optical bandgap on the dopant concentration is smaller, i.e. 0.05 eV, in comparison to the Ga doping series with the same Mg-admixture that coincides with the dependency of the free charge carrier density on the dopant concentration. In $\mathrm{Mg}_{0.04}\mathrm{Zn}_{0.96}\mathrm{O}$:Al thin films, the dependency of the free charge carrier density on the optical bandgap has been found to be similar to that of the Ga doping series. On the other hand, this dependency is different for the Al doping series that have highest Mg-admixture. In these films the optical bandgap increases only by 0.07 eV increasing the free charge carrier density in a wide range, i.e. $n \sim (1.7 - 32) \times 10^{19}\,\mathrm{cm}^{-3}$.

6.3.2 Plasma Frequency

Here, the plasma frequency ω_p is discussed, i.e. determined using infrared spectroscopic ellipsometry measurements (IRSE).

In figure 6.12, the square of the plasma energy is plotted as a function of the free charge carrier density for the (Mg,Zn)O:Al/Ga thin films. According to equation 3.4, $E_\mathrm{p} = \hbar\omega_\mathrm{p}$ becomes zero if there are no free charge carriers. As shown in the figure, this $E_\mathrm{p}^2 \sim n$ relationship is fulfilled almost for both doping series. Independent of the Mg content, experimental data points shows an excellent $E_\mathrm{p}^2 \sim n$ relationship for the free charge carrier densities lower than $1 \times 10^{20}\,\mathrm{cm}^{-3}$, which can be clearly seen in the Ga doping series (cf. figure 6.12 b). On the other hand, experimental data points are scattered more and more for higher free charge carrier concentrations of $n > 1 \times 10^{20}\,\mathrm{cm}^{-3}$ (cf.

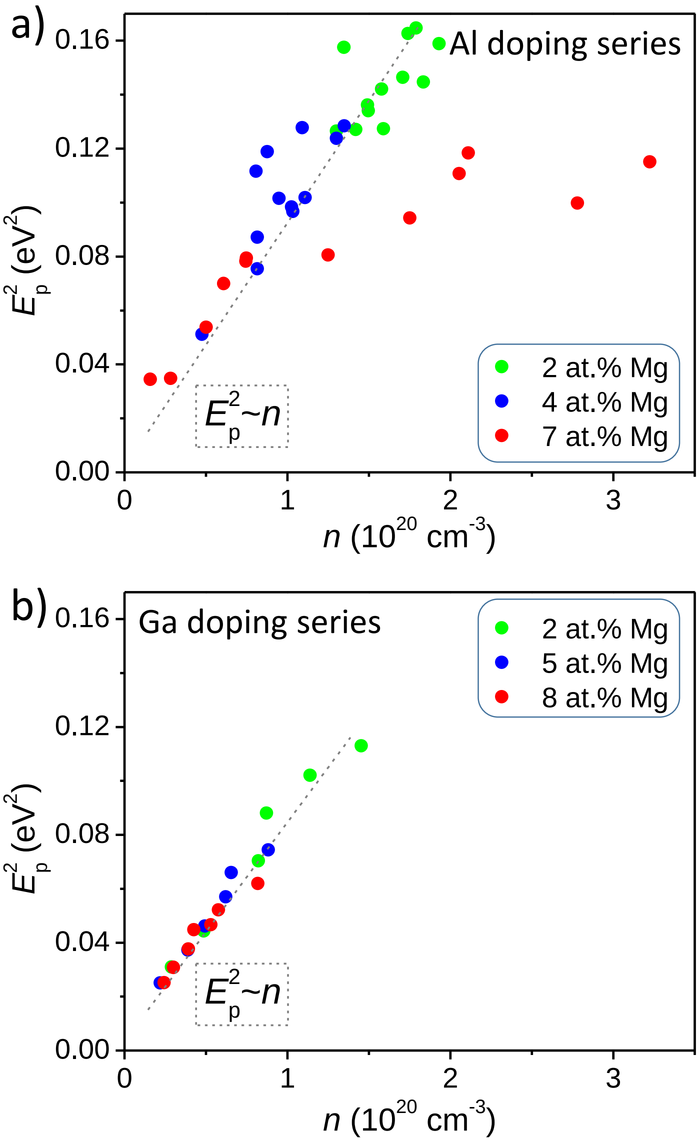

FIGURE 6.12: The dependency of the plasma energy over free charge carrier density for (a) Al- and (b) Ga-doped $Mg_xZn_{1-x}O$ films. The dashed lines are the linear dependence of E_p^2 on the free charge carrier density n.

figure 6.12 a). Similar to the discussion above on the bandgap shift, in $Mg_{0.07}Zn_{0.93}O$:Al thin films this scattering behavior of the data is more pronounced.

In figure 6.13, the plasma energy is plotted as a function of the Al/Ga doping concentration. In both doping series, the plasma energy for a given dopant concentration decreases with increasing Mg content, which can be explained with a decreased number of free charge carriers for higher Mg-admixtures. Furthermore, a dependency of the plasma energy on the doping concentration is very similar to the trend that has been observed for free charge carriers (cf. figure 6.5). E_p increases with increasing doping

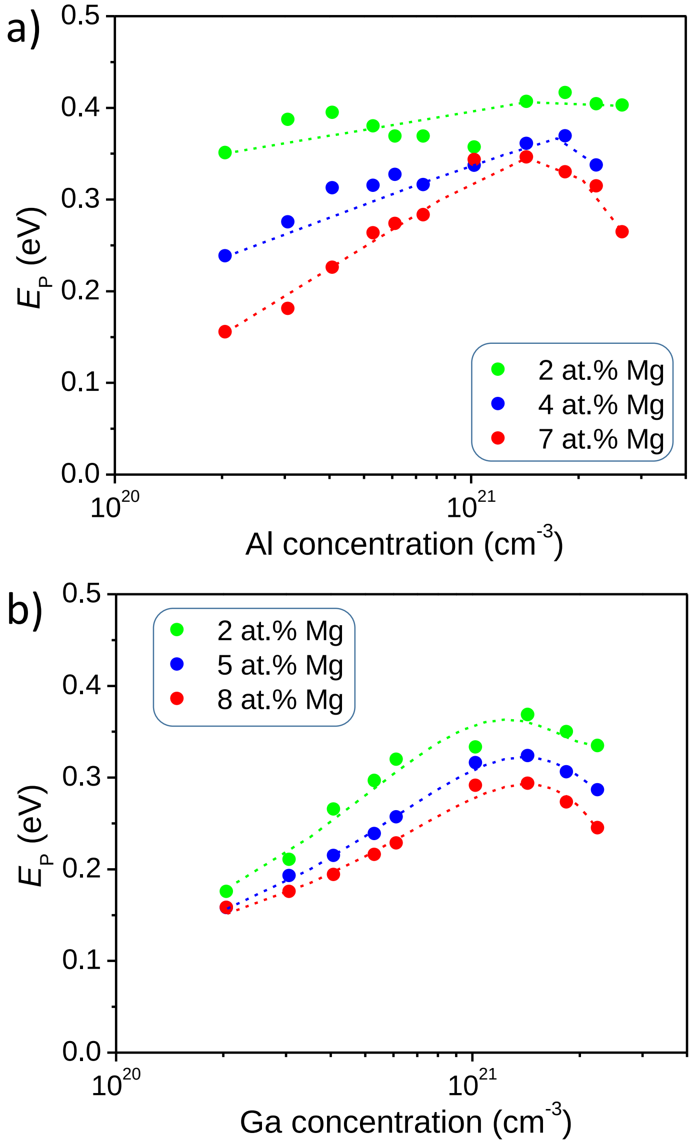

FIGURE 6.13: The plasma energy ($E_\mathrm{p} = \hbar\omega_\mathrm{p}$) of Mg$_xZn_{1-x}$O:Al/Ga films as a function of (a) Al and (b) Ga dopant concentration for indicated Mg contents. E_p was extracted from infrared spectroscopic ellipsometry (IRSE) using the Drude theory. The dashed lines are the spline approximations of the data to guide the eye.

concentration up to $N_\mathrm{d} < 1 \times 10^{21}\,\mathrm{cm}^{-3}$. It tends to decrease at higher doping levels of $N_\mathrm{d} > 1 \times 10^{21}\,\mathrm{cm}^{-3}$, where the self-compensation of the free charge carriers is dominant.

In the following, the effective electron mass of these films is discussed.

6.3.3 Effective Electron Mass

The effective electron mass of the impurity doped (Mg,Zn)O alloy is expected to increase due to (i) alloying, i.e. with increasing Mg content [23], and (ii) the Burstein-Moss effect,

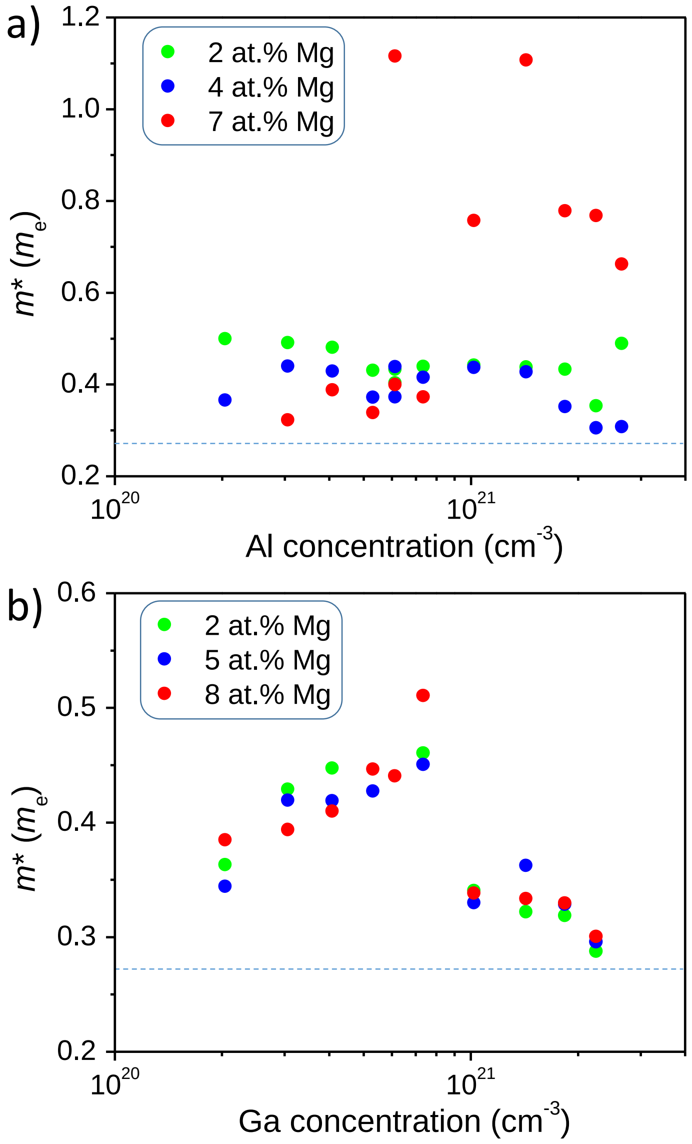

FIGURE 6.14: The effective electron masses of the $Mg_xZn_{1-x}O$:Al/Ga films as a function of (a) Al and (b) Ga dopant concentration for indicated Mg contents. The m_e^* was extracted from infrared spectroscopic ellipsometry (IRSE) using the Drude theory. Dashed lines indicate the effective mass of $0.27\,m_e$ for binary ZnO thin films.

i.e. with increasing free charge carrier density, or the combination of both. Figure 6.14 shows the effective electron masses of (Mg,Zn)O:Al/Ga thin films as a function of Al/Ga concentration for indicated Mg contents. In general, the effective electron mass values are higher than the effective electron mass of binary ZnO, i.e. $0.27\,m_e$, for all samples, including the samples with relatively low doping concentration. This might be due to the effect of the Mg alloying. On the other hand, the dependency of m_e^* on the doping concentration is also similar to the trends that have been found (i) for the free charge carriers as well as (ii) for the plasma energy. For example, at lower dopant concentrations of $N_\mathrm{d} < 1 \times 10^{21}\,\mathrm{cm}^{-3}$, higher m_e^* values are deduced for lower Mg-admixtures in the Al doping series, whereas in the Ga doping series it tends to increase systematically with increasing doping level. This might be due to the fact that band-band transitions take place from the VB to a certain level of the CB, where bandgap non-parabolicity is more pronounced. Indeed, only the CBM of ZnO can be considered parabolic with $m_\mathrm{e}^* = 0.27\,m_\mathrm{e}$, above this level the bandgap non-parabolicity has to be taken into account [15]. Furthermore, m_e^* decreases with increasing the doping level above $N_\mathrm{d} > 1 \times 10^{21}\,\mathrm{cm}^{-3}$, which is hinting to the influence of the BM-effect on the effective electron mass. Overall, the effective electron mass has changed in the range of $(0.4 \pm 0.1)\,m_e$ for the given chemical compositions of the (Mg,Zn)O:Al/Ga alloys, except the Al doping series with the highest Mg-admixture, where the masses are found to be slightly higher in comparison to other sample series.

Note

Most of the results in this chapter have been published on *Physica Status Solidi A* [8].

Chapter 7

Temperature Dependence of the Doping Efficiency in (Mg,Zn)O:Al and (Mg,Zn)O:Ga Thin Films

In this chapter, the influence of growth and annealing temperatures on doping efficiency is discussed.

7.1 Electrical Properties

Figure 7.1 shows the electrical transport properties of the Al- and Ga-doped (2.5 at. %) $Mg_{0.05}Zn_{0.95}O$ thin films for different growth temperatures. For both doping series, the mobility increases with increasing growth temperature which can be explained by the improved crystalline quality of the samples grown at higher temperature. In contrast, free charge carrier density and doping efficiency show a different dependency on the growth temperature. In the Al doping series, these parameters first increase with increasing growth temperature up to 200 °C, where the free charge carrier density has reached a value as high as $n = 8.2 \times 10^{20}\text{cm}^{-3}$ with doping efficiency of $N_{\text{d,act}} \approx 0.8$, a Hall mobility of $\mu = 13.3\,\text{cm}^2/\text{Vs}$ and a resistivity of $\rho = 5.7 \times 10^{-4}\,\Omega\text{cm}$. Above this temperature, free charge carrier density and doping efficiency tend to decrease. In the Ga doping series, free charge carrier density and doping efficiency first increase up to a growth temperature of about 300 °C, and saturates. Interestingly, at higher growth temperatures of 600 °C, the free charge carrier density as well as mobility have been found to be similar for both doping series, being $n = 1.25 \times 10^{20}\text{cm}^{-3}$, $\mu = 31.04\,\text{cm}^2/\text{Vs}$ and $n = 8.5 \times 10^{19}\text{cm}^{-3}$, $\mu = 33.11\,\text{cm}^2/\text{Vs}$ for the Al and Ga doped films, respectively. In order to understand this dissimilarity (similarity) of electrical properties at low (high)

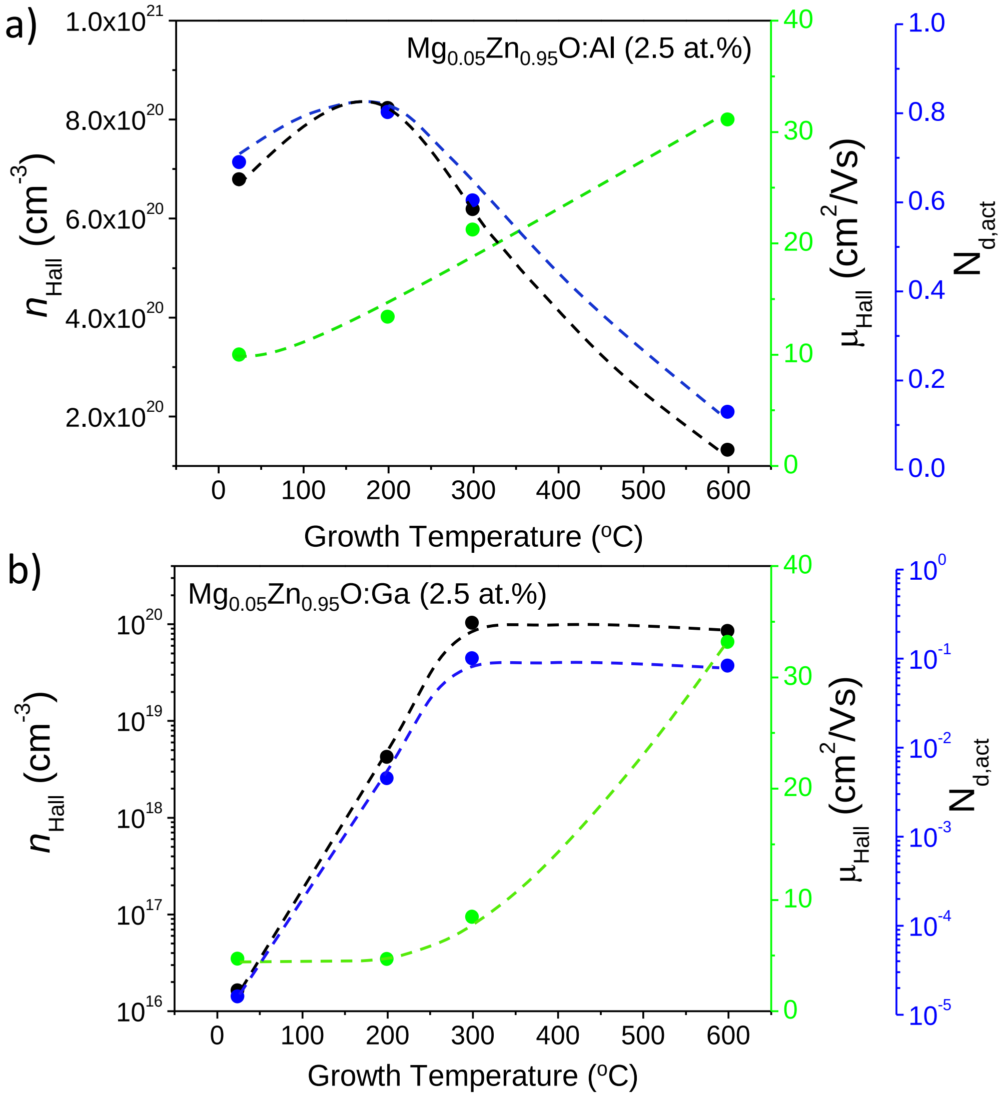

FIGURE 7.1: The free charge carrier density n, mobility μ, and doping efficiency $N_{d,act}$ as a function of growth temperature for (a) Al and (b) Ga-doped $Mg_{0.05}Zn_{0.95}O$ thin films. Both doping series have a fixed dopant concentration of 2.5 at. %. Dashed lines are guide to the eye.

growth temperatures, we post-annealed the films in vacuum at 400 °C. In the following, the influence of post-annealing on the electrical properties is discussed first for the Al doping series, followed by the discussion on the Ga doping series.

Figure 7.2 shows the free charge carrier density and the mobility of Al-doped $Mg_{0.05}Zn_{0.95}O$ thin films as a function of annealing time.

As a result of the annealing, free charge carrier density and mobility decreased for all films grown at $T_g < 400$ °C. The biggest changes in the free charge carrier density as well as mobility were observed within the first 60 minutes of annealing time. With increasing annealing time, changes in electrical parameters became smaller and smaller. It appears

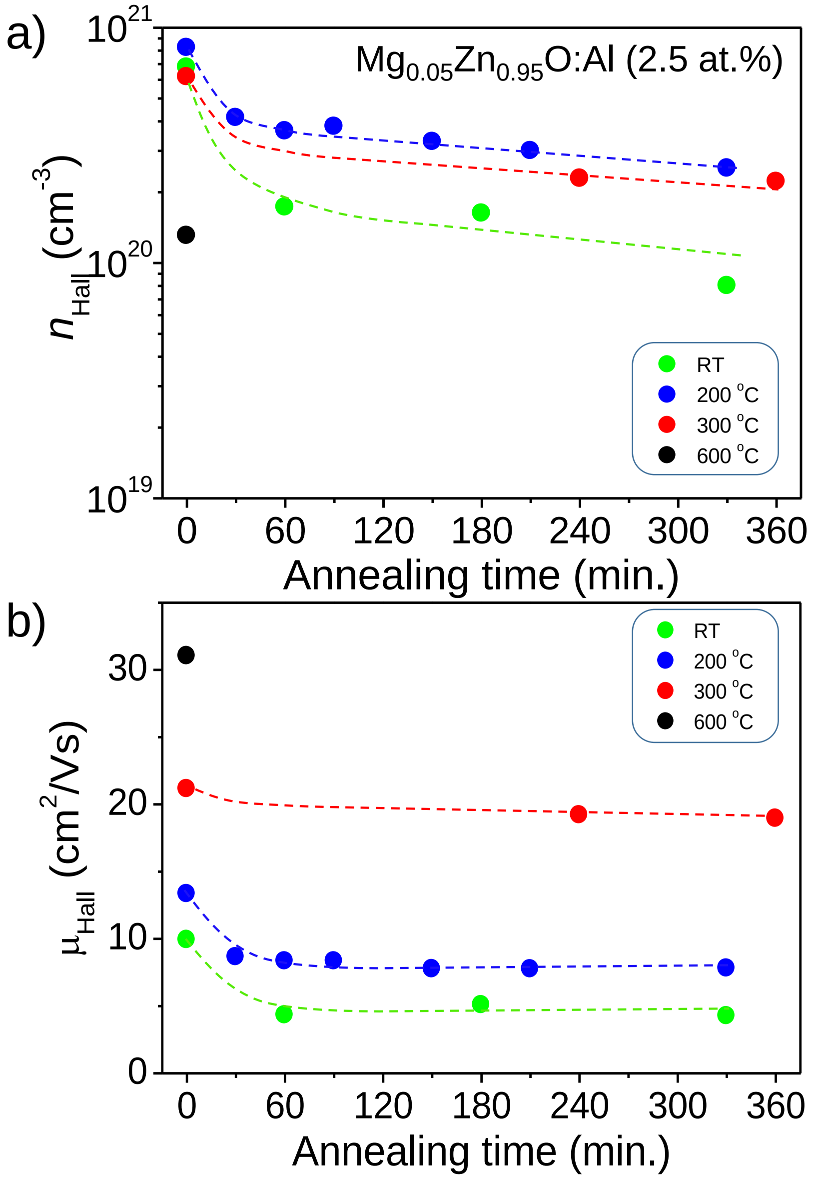

FIGURE 7.2: Dependence of (a) the free charge carrier density and (b) mobility on annealing time for $Mg_{0.05}Zn_{0.95}O$:Al (2.5 at. %) PLD films. Annealing was performed in vacuum at 400 °C. Dashed lines are guide to the eye.

to be that these films initially were in a metastable state, subsequently they get close to a thermodynamic equilibrium state under post-annealing. Hence, with increasing annealing time the number of free charge carriers is getting close to the data which was acquired for the film initially grown at the high temperature of 600 °C. If we look at the data of the high temperature grown samples (T_g = 600 °C), the Al-doped film exhibited a free charge carrier density of $n_{\mathrm{Hall}} = 1.25 \times 10^{20} \mathrm{cm}^{-3}$, corresponding to the solubility limit of Al_2O_3 in ZnO of 0.3 at.% , also determined by Shirouzu *et al.* [9] for high temperature grown (T_g > 600 °C) Al-doped ZnO. However, the free charge carrier densities of annealed films, i.e. grown at 200 °C and 300 °C are still higher than n of the

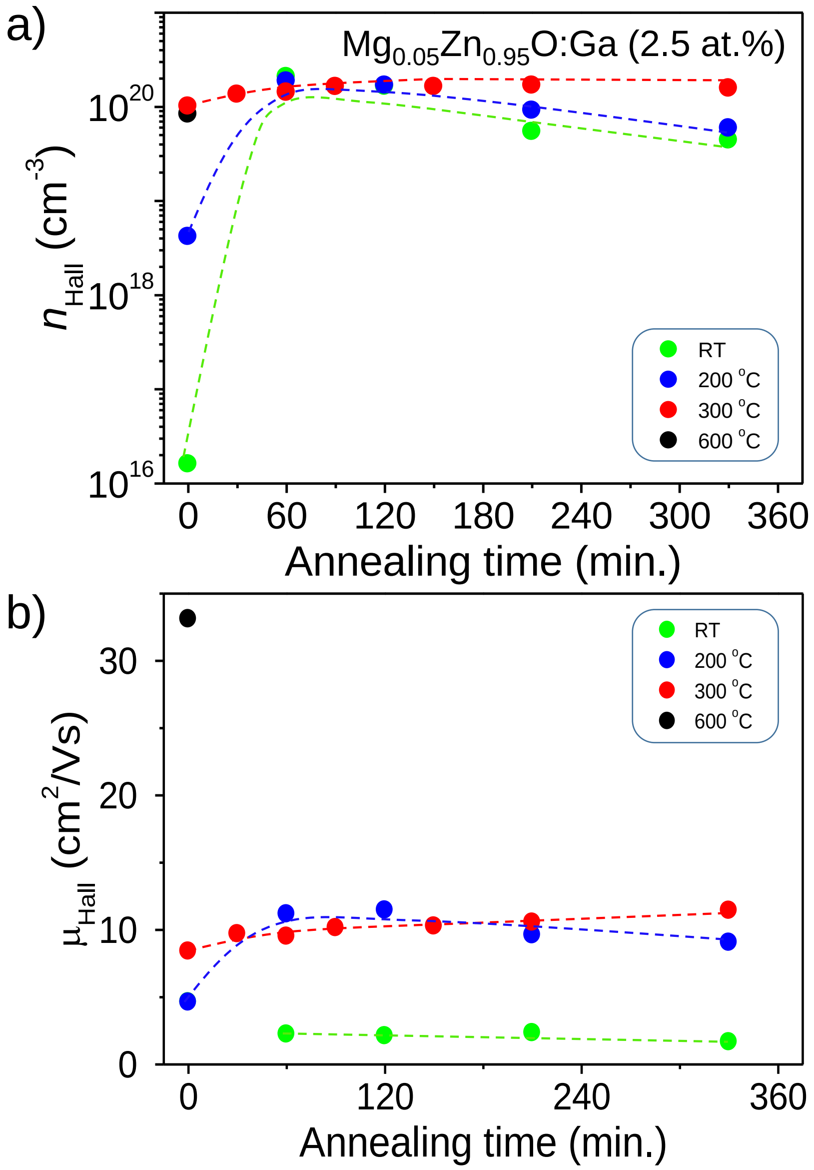

Figure 7.3: Dependence of (a) the free charge carrier density and (b) mobility on annealing time for $Mg_{0.05}Zn_{0.95}O$:Ga (2.5 at. %) thin films. Annealing was performed in vacuum at 400 °C. Dashed lines are guide to the eye.

samples grown at 600 °C. This might be due to the fact that at higher temperatures the probability of the formation of compensating defects is higher, but the chosen annealing temperature of 400 °C and/or annealing time are still not sufficient to equilibrate the metastable solid solution. The mobility of the free charge carriers also decreases as a result of the annealing (cf. figure 7.2 b). Apparently, the formed intrinsic defects do compensate the free charge carriers and act as ionized impurity scattering centers.

In figure 7.3, the free charge carrier density and the mobility of $Mg_{0.05}Zn_{0.95}O$:Ga thin films are shown as a function of the annealing time. The free carrier density of as-grown Ga-doped samples, i.e. grown at $T_g \leq 300\,°C$, is substantially lower than the values

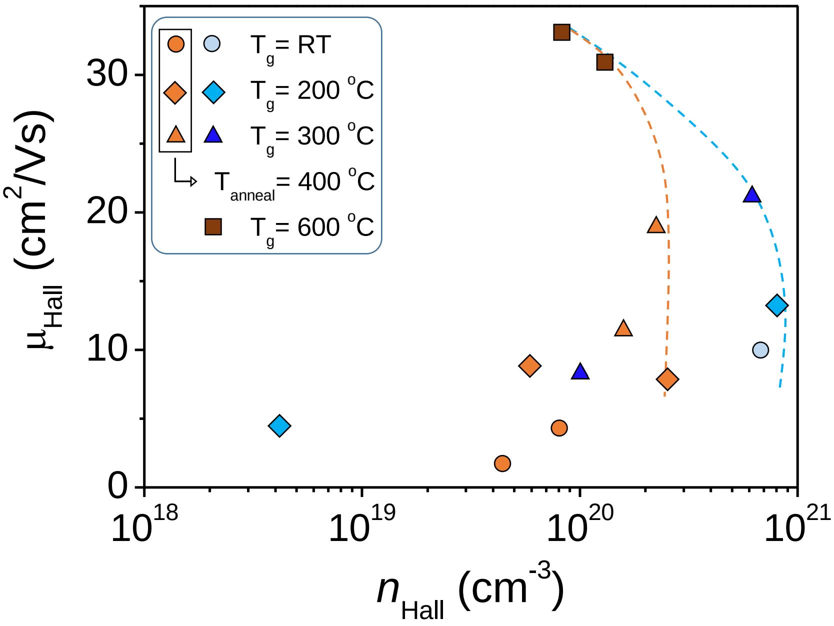

FIGURE 7.4: The mobility μ_{Hall} as a function of the free charge carrier density for as-grown and annealed $Mg_{0.05}Zn_{0.95}O$:Al/Ga (2.5 at. %) thin films. Annealing was performed in vacuum at 400 °C. Dashed lines are guide to the eye.

determined for Al-doped samples grown at the same temperatures. While for the Al-series the free charge carrier density is in principle independent of T_{g} for $T_{\mathrm{g}} \leq 300\,°\mathrm{C}$, it systematically increases for the Ga-series with increasing T_{g}. When the samples of the Ga-series were annealed, during the first 60 minutes the free charge carrier density increased. That might be due to the fact that more Ga ions became electrically active during the post-annealing by contributing free electrons into the system. With further increasing annealing time n saturated. Similar to Al doped films, the saturation values of the free charge carrier densities are very close to the data obtained for high temperature grown film at $T_{\mathrm{g}} = 600\,°\mathrm{C}$. The Hall mobility also varied as a function of annealing time. Corresponding to the free charge carrier density, the mobility first increased at the beginning of annealing process, then saturated (cf. figure 7.3 b). This can be explained as following. First, more and more Ga ions became electrically active by contributing free electrons into the system. Subsequently, potential barriers at grain boundaries are screened more effectively, thus the mobility increases. Hence, as also found for the Al-doping series, ionized impurity scattering prevents a further increase of the mobility. From figure 7.4, it is apparent that ionized impurity scattering is more pronounced for annealed films. As discussed above, it is expected that not only Al or Ga ions, but also the compensating defects contribute to increase of ionized impurity scattering [8]. Looking at the data for the samples grown at 300 °C, i.e. in figure 7.2 b) and figure 7.3 b), the Ga doped sample has a lower free carrier density and mobility in comparison to the Al doped one. One possible explanation might be that N_a is higher in this film compared to the Al doped film. As a consequence, the latter exhibit a higher electron mobility. As discussed in chapter 6, these acceptor-like compensating defects are most probably zinc vacancies ($\mathrm{V_{Zn}}$) and its complexes in ZnO and (Mg,Zn)O.

7.2 Structural Properties

In figure 7.5, the surface morphology is shown for Al and Ga doped $\mathrm{Mg_{0.05}Zn_{0.95}O}$ thin films grown and post-annealed at 200 °C, and 400 °C, respectively. The Al doped film depicted higher root mean square value (rms) of 4.0 nm compared to the Ga doped one that has a rms value of only 1.6 nm. This could also be a reason for the different mobility values on the background of different carrier concentration, being $\mu = 13.3\,\mathrm{cm^2/Vs}$ and $\mu = 4.8\,\mathrm{cm^2/Vs}$ for as-grown Al and Ga doped films, respectively. After the heat treatment, the rms value of the Al doped film decreased to 3.3 nm, while the Ga doped film showed a slight increase and depicted 1.9 nm. As a result, the surface of the former became more smooth whilst the latter stayed almost unchanged. Figure 7.6 depicts the

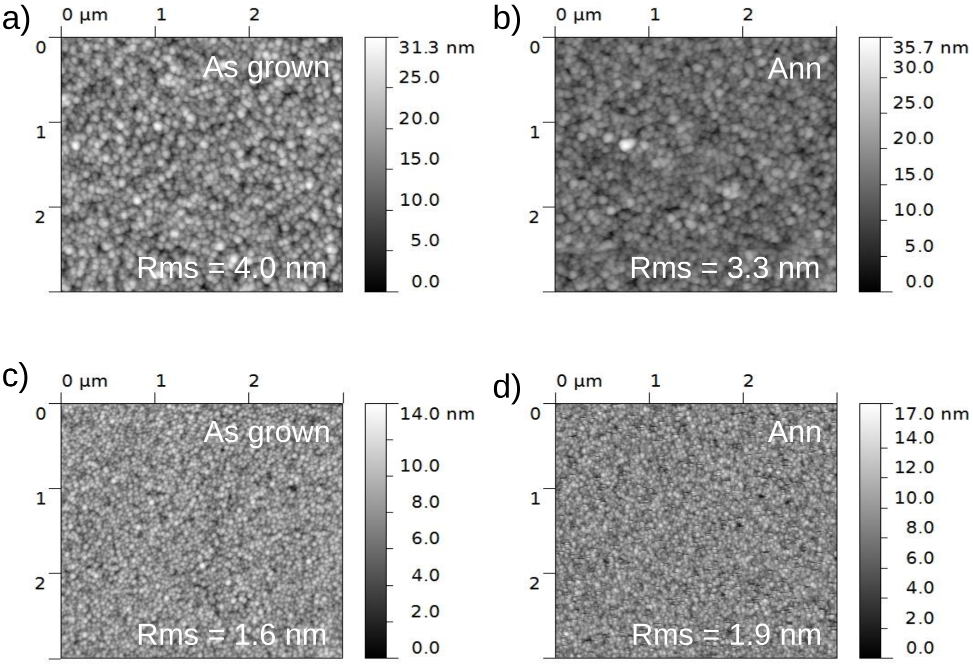

FIGURE 7.5: The surface morphology of as-grown and post-annealed (a,b) Al and (c,d) Ga doped $\mathrm{Mg_{0.05}Zn_{0.95}O}$ thin films. Rms values for Al (Ga) doped films are found to be 4.0 nm (1.6 nm) and 3.3 nm (1.9 nm) before and after post-annealed, respectively. These samples are grown at 200 °C and annealed in vacuum at 400 °C. Note that the measurements were performed after final heat treatment ($\sim 6h$) for the annealed cases.

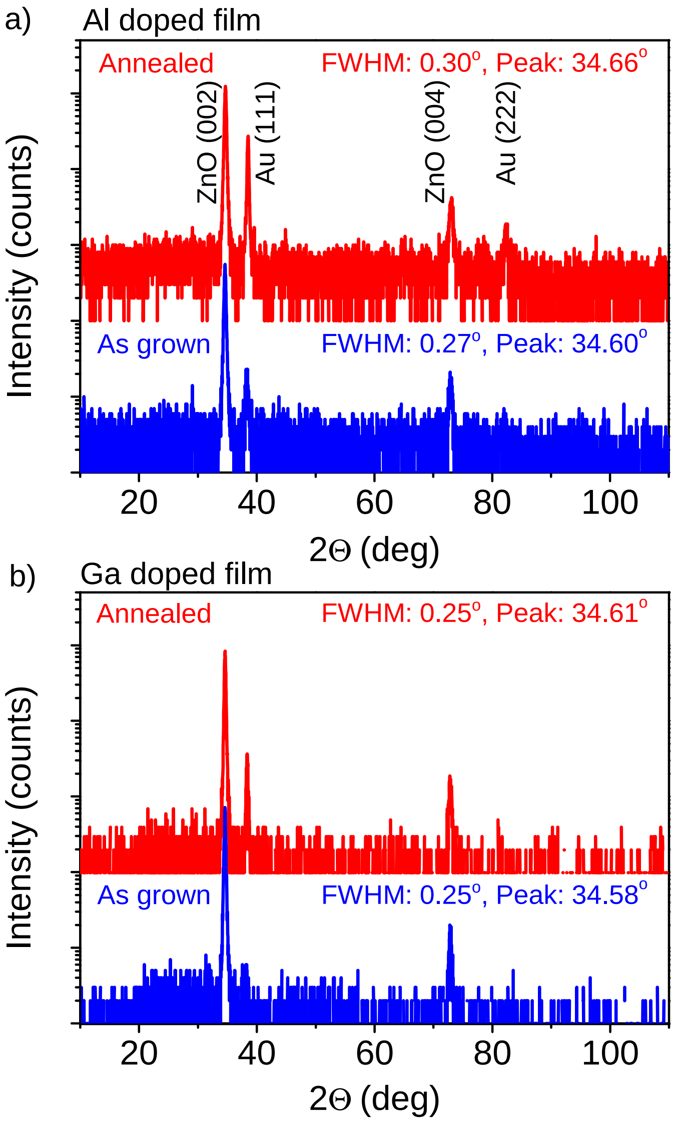

FIGURE 7.6: Wide angle XRD $2\Theta - \omega$ scans for (a) Al and (b) Ga doped $Mg_{0.05}Zn_{0.95}O$ thin films with a thickness of 270 nm and 360 nm, respectively. These samples were grown at 200 °C and annealed in vacuum at 400 °C. Note that the measurement data for the annealed films were taken for final steps ($\sim 6h$) and the Au contacts were sputtered on the corners of the films for Hall-effect measurement.

wide-angle $2\Theta - \omega$ scans in the range of 10 and 110° for these films. From XRD data, secondary phases were detected neither for as-grown nor post-annealed films. (111) and (222) diffraction peaks of Au occur resulting from ohmic Au contacts sputtered at the corners on the films. The intensity of the diffraction peaks tends to increase as a result of annealing which can be seen for the Au(111) and Au(222) peaks. This can be explained by the changes occurred on the film surface, where post-annealed films have smoother surfaces compared to as-grown ones (cf. figure 7.5). All ZnO films show (00.2) orientation and the peak position shifted to higher angles as a result of annealing.

Table 7.1: Free charge carrier density and optical bandgap energies of as-grown and post-annealed $Mg_{0.05}Zn_{0.95}O$:(Al/Ga) thin films. The samples were annealed in vacuum at 400 °C for 6 hours.

T_g (°C)	dopant	n ($10^{20}cm^{-3}$)	n(anneal) ($10^{20}cm^{-3}$)	E_g (eV)	E_g(anneal) (eV)
25	Al	6.8	0.82	-	3.65
200	Al	8.2	2.7	4.05	3.62
300	Al	6.2	2.24	-	3.64
600	Al	1.3	1.38	3.59	3.60
25	Ga	10^{-4}	0.44	3.41	3.65
200	Ga	0.04	0.61	3.37	3.55
300	Ga	0.92	1.6	3.54	3.64
600	Ga	0.83	0.97	3.61	3.61

Chang *et al.* have also observed this behavior on post-annealed Al-doped ZnO films at 500 °C that were initially grown at $T_g = 200\,°C$ [154]. They argued that the residual stress of the films can be reduced by annealing and resulting in a peak-shift towards higher angles.

Tong *et al.* have reported the influence of post-annealing on the electrical properties of Al-doped ZnO [155]. They performed annealing processes under hydrogen, nitrogen and oxygen atmosphere. Apparently, the influence of the annealing atmosphere has to be considered for temperatures below 400 °C. For higher annealing temperatures the annealing atmosphere is less important.

7.3 Optical Properties

As shown in figure 7.7 and in agreement with the electrical data, the optical bandgap shows strongest BM-shift for $T_g \leq 400\,°C$. Samples grown/annealed above this temperature showed similar optical bandgaps in the range of 3.5 ± 0.1 eV. For comparison, reported literature data have been also included for doped $Mg_xZn_{1-x}O$ $(0 < x < 0.1)$ thin films. According to the equation 3.1, the contribution of Mg-content to the given bandgap values of these films is about 0.14 eV at most that is within the range of the highlighted error bar (cf. gray area in figure 7.7). This is also consistent with the bandgap values that have been obtained for annealed films (cf. table 7.1). An explanation for this could be that the high temperature grown/annealed samples are more close to thermodynamic equilibrium state and with that the effective doping level is limited and the Fermi level is pinned by spontaneously formed compensating defects. Additionally, in equilibrium state, the solubility limit of Al and Ga is low, i.e. ≈ 0.3 at.%.

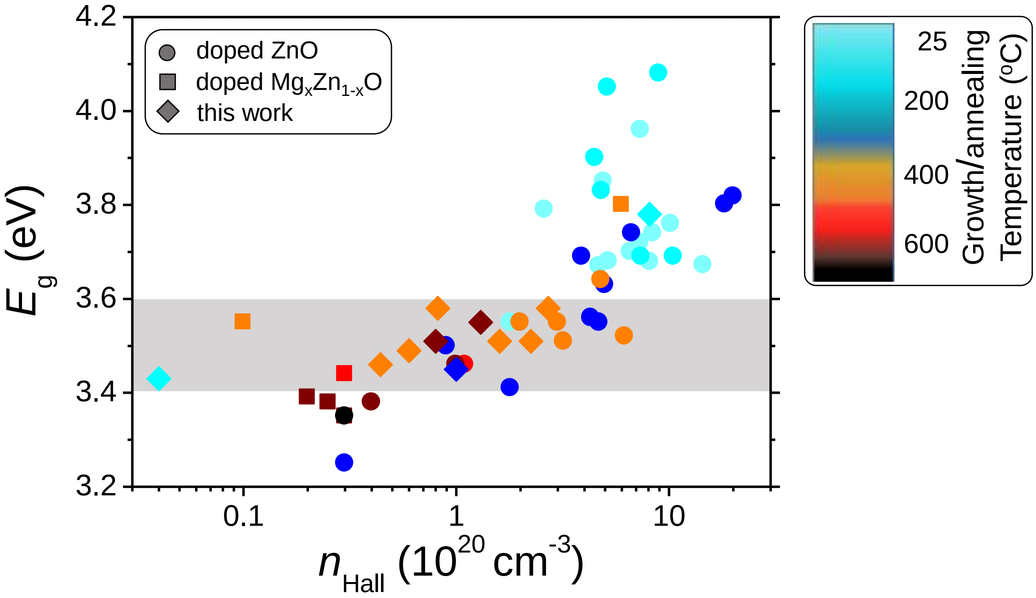

FIGURE 7.7: Optical bandgap energies of doped ZnO and $Mg_xZn_{1-x}O$ ($0 < x < 0.1$) thin films as a function of free charge carrier density and growth/annealing temperature. Literature data are taken from [8, 25, 27, 34, 153, 155–165]. The gray area is a guide to the eye.

7.4 Discussion

In figure 7.8, free carrier density n and the doping efficiency $N_{\mathrm{d,act}}$ are plotted as a function of growth and annealing temperatures. For comparison, literature values on doped ZnO and $Mg_xZn_{1-x}O$ thin films for $0 \leq x(\mathrm{Mg}) \leq 0.1$ are also included. Despite the different growth methods and conditions used, these parameters show distinct dependence on growth/annealing temperature. These experimental data points showed that the free carrier density is about one order of magnitude higher at low growth temperatures ($T_{\mathrm{g}} < 400\,^{\circ}\mathrm{C}$) by reaching the values in the range of $n \approx (1-2) \times 10^{21}\,\mathrm{cm}^{-3}$, compared to high temperature grown samples ($T_{\mathrm{g}} > 400\,^{\circ}\mathrm{C}$) that have a free charge carrier density of only $n \approx (1-2) \times 10^{20}\,\mathrm{cm}^{-3}$. The highest doping efficiency was also observed for lower growth temperature, it tends to decrease with increasing growth/annealing temperature. This can be explained in two ways; first, at higher growth/annealing temperatures, i.e. $T_{\mathrm{g}} > 400\,^{\circ}\mathrm{C}$, the density of electrically active donors decreases or second free charge carriers (electrons) resulting from these extrinsic dopants are compensated by intrinsic self-compensating defects. As discussed in previous sections of this chapter, the free charge carrier density of the Ga doping series first increases as a result of post-annealing indicating that more and more Ga ions became electrically active (cf. figure 7.3). On the other hand, free charge carrier density saturates at about $n \approx 1 \times 10^{20}\,\mathrm{cm}^{-3}$ or even

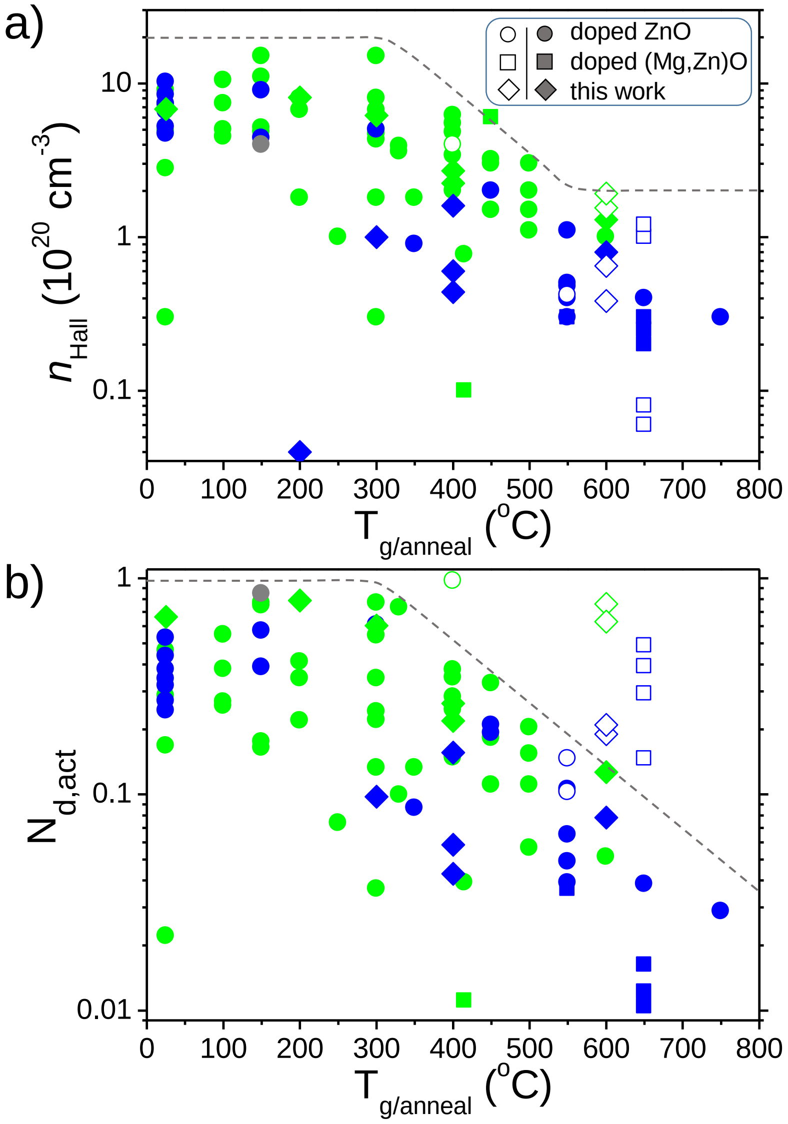

FIGURE 7.8: (a) Free charge carrier density n_{Hall}, and (b) doping efficiency $N_{\mathrm{d,act}}$ versus growth/annealing temperature for doped ZnO, and $\mathrm{Mg}_x\mathrm{Zn}_{1-x}\mathrm{O}$ $(0 < x < 0.1)$ thin films. Al, Ga and In doped films are given with green, blue and gray symbols, respectively. Literature data are taken from [8, 25, 27, 31, 34, 76, 94, 146, 153, 155–159, 161–165]. Note that the films with filled symbols have a dopant concentration of $\mathrm{N_D} > 1\,at.\%$, where the films with $\mathrm{N_D} \leq 1\,at.\%$ are given with open symbols. Dashed lines are guides to the eye.

tends to decrease with increasing annealing time where self-compensation is more and more pronounced.

Zakutayey *et al.* have also found that the samples grown at lower growth temperature exhibit higher conductivity than high temperature (> 500 °C) grown ones [166]. It has been argued that the former samples are in the non-equilibrium state, where the latter is in the thermodynamic equilibrium.

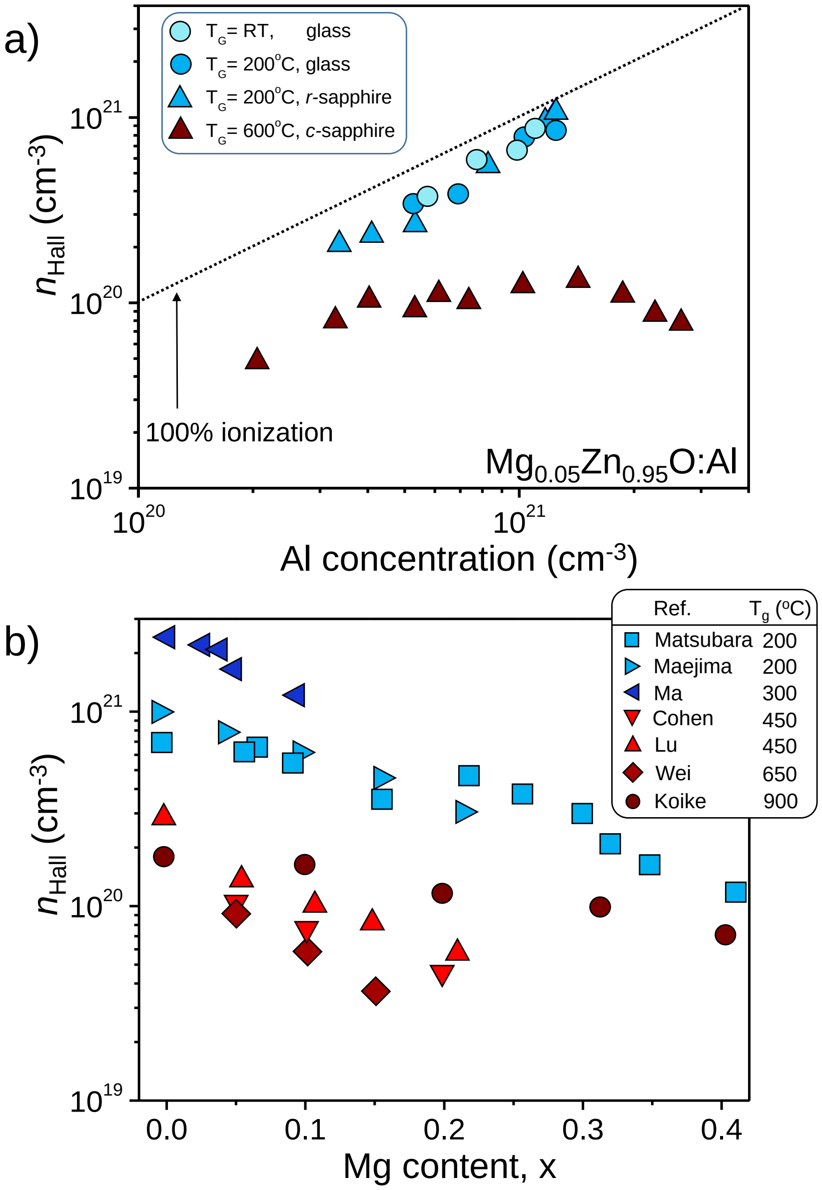

FIGURE 7.9: Dependence of the n_{Hall} on (a) Al and (b) Mg contents for impurity doped $Mg_xZn_{1-x}O$ alloys grown at different growth temperatures. The data given in (b) are taken from [24–27, 29, 30, 34]. Dashed lines are guide to the eye.

Figure 7.9 a) depicts the free charge carrier density of Al doped $Mg_{0.05}Zn_{0.95}O$ alloys as a function of Al concentration for different growth temperatures. Among all temperature series, the low temperature grown samples, i.e. at $T_g < 300\,°C$, showed high doping efficiency in the range of $0.8 < N_{d,act} < 1$. As discussed above, for high temperature grown samples, i.e. $T_g = 600\,°C$, the obtained free charge carrier densities are relatively low. For comparison, reported literature values on free charge carrier density of impurity doped $Mg_xZn_{1-x}O$ alloys are also given as a function of Mg content, x (cf. figure 7.9 b).

In general, n tends to decrease with increasing Mg content for all reported data. However, some references, i.e. Q. Ma *et al.* [29], have reported very high free charge carrier density of $n \geq 1 \times 10^{21}\,\mathrm{cm}^{-3}$ for $0 < x < 0.22$, whereas other reports have depicted relatively low free charge carrier densities. Interestingly, this scattering of the reported data is also related to the growth temperature where high temperatures grown samples, i.e. above $T_\mathrm{g} > 400\,^\circ\mathrm{C}$, have depicted the free carrier density of only $n \leq 3 \times 10^{20}\,\mathrm{cm}^{-3}$ at most.

7.5 Thermal Stability of ZnO Thin Films

Minami *et al.* reported on undoped, sputtered ZnO films that have a free charge carrier density in the order of $n \sim 10^{20}\,\mathrm{cm}^{-3}$ [87, 167]. They argued that the ZnO film properties, ten months exposed in air at RT, was stable. When the films were post-annealed for one hour in different atmosphere, being in air, vacuum, hydrogen, and inert gases, i.e. nitrogen and argon, at temperatures up to 400 °C, the resistivity of the films increased by one to ten orders of magnitude. It had been found that not only high temperature, but also the annealing atmosphere has an impact on deteriorated electrical properties. The biggest (smallest) increase in resistivity was depicted for air (hydrogen) atmosphere. Increased resistivity was mainly correlated with the change in free charge carrier density, but not mobility as it was only ± 10%. The decrease in the free charge carrier density was suggested resulting from increased chemisorption of oxygen [168] that could illuminate the shallow donor levels formed from native defects, i.e. oxygen vacancy and zinc interstitials [169, 170]. The capturing of oxygen by defects such as grain boundaries, or even by the surface of the ZnO films in the case of post-annealing in air, was suggested [167]. On the other hand, decreasing of the mobility despite increased or unchanged crystall quality was attributed to the lowering of the Fermi level towards the centre of the bandgap, resulting in the greater effectiveness of scattering centers located below the CBM [171].

It has been found that the high optical transmittance of ZnO films in the VIS range of the spectrum stayed unchanged during the post-annealing despite the changes of the electrical properties. Investigations showed that the ZnO films have the similar stability on different substrates, i.e. Si, GaAs, sapphire and glasses. Moreover, neither cracks or damages were observed when ZnO was directly immersed into the liquid nitrogen, nor it affected the resistivity. Thus, undoped ZnO had been found to be stable at temperatures below 100 °C, that makes it a suitable transparent electrode for only low temperature applications [167].

The thermal stability of impurity doped ZnO have been also reported [94, 95]. The resistivity of these doped ZnO films were found to be more stable at higher temperatures compared to undoped, intrinsic ZnO thin films [172]. This improved stability has been correlated with higher stability of extrinsic dopants for oxygen chemisorption in comparison to intrinsic defects.

Qiu *et al.* [173] reported on air heat treatment of magnetron sputtered ZnO:In films and found that the films were only stable at post-annealing temperature up to 250 °C.

Minami *et al.* [174] have also found that the growth and annealing temperatures have an impact on electrical properties. They found that the electrical properties are almost independent of the annealing temperature in the temperature range between $(250-350)\,°\mathrm{C}$. When the ZnO:Al (2 wt.%) films, i.e. initially grown at 250 °C, were annealed one hour in atmosphere at different temperatures up to 400 °C, its initial resistivity of $2.7\times10^{-4}\,\Omega\mathrm{cm}$, free charge carrier density of $n \approx 10^{21}\,\mathrm{cm}^{-3}$ and mobility of $\mu \approx 20\,\mathrm{cm}^2/\mathrm{Vs}$ showed good stability for temperatures below 300 °C, which is more stable compared to those undoped ZnO films. Our experimental results discussed in this chapter are found to be similar to these reports. It has been found that the doping efficiency is dependent on growth or annealing temperatures. Samples grown at low temperatures below 400 °C showed very high doping efficiency in the range of $0.8 < \mathrm{N}_{\mathrm{d,act}} < 1$ for dopant concentration of $[\mathrm{Al/Ga}] < 2\times10^{21}\,\mathrm{cm}^{-3}$, whereas at higher growth or annealing temperatures above 400 °C $\mathrm{N}_{\mathrm{d,act}}$ strongly decreases and free charge carrier density saturates at about $n \approx (1-2)\times10^{20}\,\mathrm{cm}^{-3}$. Indeed, this saturation value of n is similar to the solubility limit of 0.3 at.% for Al in ZnO, that was determined by Shirouzu *et al.* [9] for high temperature grown ($T_{\mathrm{g}} > 600\,°\mathrm{C}$) films. Appearance of this saturation of n in equilibrium condition can be well explained within the amphoteric defect model. According to this model, the density of acceptor-like compensating defects, i.e. V_{Zn} in n-type ZnO and (Mg,Zn)O, increase as soon as the Fermi energy level shifts towards the conduction band edge by limiting the n from further increase.

Note

The results of this chapter has been accepted for publication on *J. Appl. Phys.* [175].

Chapter 8

Summary and Conclusion

8.1 Summary

In this thesis, the structural, optical and electrical properties of wurtzite $\mathrm{Mg}_x\mathrm{Zn}_{1-x}\mathrm{O}$:Al and $\mathrm{Mg}_x\mathrm{Zn}_{1-x}\mathrm{O}$:Ga thin films have been investigated in dependence on Mg and Al/Ga concentrations. For this purpose, the samples were deposited on 2-inch in diameter sapphire with c-plane and r-plane orientation and on glass substrates by pulsed-laser deposition (PLD) applying the continuous composition spread method (CCS), that allows to grow thin films with lateral composition gradient(s) [7]. During the deposition, a threefold segmented PLD target was ablated in order to grow thin films with two, lateral composition gradients, i.e. the Mg composition is varied in one direction whereas the Al/Ga concentration is varied in a perpendicular direction. Subsequently, these CCS wafers were cut into $(5{\times}5)\,\mathrm{mm}^2$ pieces along the both composition gradients. As a result, a large material library has been created consisting of thin films with varying Al or Ga dopant concentration in the range of $0.5\,\mathrm{at.\%} < \mathrm{Al/Ga} < 7.0\,\mathrm{at.\%}$ and Mg alloy content of $0.01 < x(\mathrm{Mg}) < 0.1$ grown under the same condition. Moreover, the influence of growth temperature on doping efficiency has also been investigated. For this purpose, $\mathrm{Mg}_{0.05}\mathrm{Zn}_{0.95}\mathrm{O}$ PLD films doped with Al and Ga ($2.5\mathrm{at.\%} \mathrel{\widehat{=}} 1 \times 10^{21}\,\mathrm{cm}^{-3}$) have been grown at different substrate temperatures in the range of $(25 - 600)\,^\circ\mathrm{C}$, otherwise have the fixed, optimized growth conditions. In addition, these samples have been post-annealed in vacuum at $400\,^\circ\mathrm{C}$ in order to test the stability of the doping level achieved.

From the experimental results, it has been found that the dopant efficiency tends to decrease with increasing Mg content x as well as Al/Ga concentration ($N_\mathrm{d} > 6{\times}10^{20}\,\mathrm{cm}^{-3}$), which can be explained with an increasing density of acceptor-like compensating defects. With increasing dopant concentration of N_d up to $6 \times 10^{20}\,\mathrm{cm}^{-3}$, the free charge carrier density n shows first an $n \propto N_\mathrm{d}$, then an $n \propto {N_\mathrm{d}}^{1/2}$ behavior. In fact, this is due to the compensation of the free charge carriers by doubly chargeable defects hinting to the zinc vacancy as microscopic origin. In other words, increased N_d causes a shift of the Fermi energy level upwards within the conduction band, resulting in a decrease of the formation energy of $\mathrm{V_{Zn}}$. Further increasing the dopant concentration above $2 \times 10^{21}\,\mathrm{cm^{-3}}$ leads to a degradation of electrical and structural properties.

The mobility for both doping series, $\mathrm{Mg_{0.05}Zn_{0.95}O}$:Al and $\mathrm{Mg_{0.05}Zn_{0.95}O}$:Ga (Al/Ga = 2.5at.% $\hat{=}\ 1 \times 10^{21}\,\mathrm{cm^{-3}}$), systematically increased with increasing growth temperature for the whole investigated range of $(25 - 600)\,^\circ\mathrm{C}$. This is an indication that high temperature grown samples have a better crystalline quality. In contrast, the free charge carrier density showed a different dependency on the growth temperature. For lower growth temperatures of $T_\mathrm{g} \leq 300\,^\circ\mathrm{C}$, Al-doped films depicted higher free charge carrier densities compared to Ga-doped counterparts. For $T_\mathrm{g} = 600\,^\circ\mathrm{C}$, the free charge carrier density depicted similar values of $n \sim 1 \times 10^{20}\,\mathrm{cm^{-3}}$ for both doping series. Post-annealing changes the free charge carrier density and the mobility. In both doping series, the largest changes were observed for low temperature grown samples (room temperature) whereas the magnitude of the changes systematically decreased with increasing T_g. The free charge carrier density of Al-doped samples decreased and saturated at about $n \sim (1 - 2) \times 10^{20}\,\mathrm{cm^{-3}}$ with increasing annealing time. This is an indication for the increase of the concentration of the acceptor-like defects. Moreover, the mobility decreases during the post-annealing process that supports the fact that these compensating defects also act as ionized impurity scattering centers. On the other hand, free charge carrier density and mobility of Ga-doped samples first slightly increased and finally saturated with increasing annealing time. This is due to the fact that more and more Ga ions became electrically active by contributing free electrons into the system. As a result, the potential barriers at the grain boundaries are screened more effectively, thus the mobility increases. Apparently, compensating defects also start to form due to the enhanced n (and increased Fermi energy level) limiting the free charge carrier density and the mobility from a further increase. Interestingly, these saturation values of n, i.e. $n \approx 1 \times 10^{20}\,\mathrm{cm^{-3}}$, are similar to (i) the data obtained for high temperature grown samples and (ii) the solubility limit of 0.3 at.%, that was determined by Shirouzu *et al.* [9] for high temperature grown, $T_\mathrm{g} > 600\,^\circ\mathrm{C}$, Al-doped ZnO.

Corresponding to the electrical data, the optical bandgap energy E_g, also decreased to $3.5 \pm 0.1\,\mathrm{eV}$ for high temperature grown or annealed samples, i.e. $T_\mathrm{g/anneal} \geq 400\,^\circ\mathrm{C}$. These approached constant values of n and E_g can be explained within the amphoteric defect model (ADM). According to this model, the generation of acceptor-like compensating defects, i.e. $\mathrm{V_{Zn}}$ in n-type ZnO and (Mg,Zn)O, increases as soon as the Fermi energy level shifts upwards. This is also consistent with theoretical calculations. The formation energy of V_{Zn} is significantly reduced or even becomes zero when the Fermi level is in the conduction band.

8.2 Conclusions

The results of this work are expected to be interesting for both (a) developing high quality transparent electrodes, and (b) fundamental material science:

(a) **It has been shown that**

- Thin films can be prepared by PLD using CCS method with two perpendicular, lateral composition gradients, i.e. the Mg composition is varied in one direction whereas the Al or Ga concentration is varied in a perpendicular direction. Using this, it is possible to prepare a large material library consisting of thin films with different material compositions for systematic investigations;
- Al and Ga dopant contents up to 2.5 at.% (or [Al/Ga] $\approx 10^{21}\text{cm}^{-3}$) can be used to enhance the electrical properties of wurtzite $Mg_xZn_{1-x}O$ solid solutions, beyond that the electrical properties sharply deteriorate and the doping efficiency drops [8];
- the growth and/or annealing temperatures are important as they strongly affect to the metastable state of the solid solution;
- the highest free charge carrier density n and doping efficiency $N_{\mathrm{d,act}}$ are obtained for the films grown at growth temperatures of 200 °C and 300 °C for Al and Ga doped thin films, respectively;
- the mobility systematically increases with increasing the growth temperature. The highest mobility was found for high temperature grown samples, i.e. at $T_{\mathrm{g}} = 600\,^{\circ}\mathrm{C}$;
- highly conductive (Mg,Zn)O:Al and (Mg,Zn)O:Ga alloys can be prepared at growth temperatures in the range of $200\,^{\circ}\mathrm{C} < T_{\mathrm{g}} < 300\,^{\circ}\mathrm{C}$;
- For the growth conditions used in this work, Al-doped films showed lowest resistivity for the entire range of dopant concentration up to $N_{\mathrm{d}} \leq 2 \times 10^{21}\text{cm}^{-3}$.

Main limitations for doping of semiconductors are (i) shallowness of the dopant energy levels, (ii) solubility limit of impurities in host material, and (iii) intrinsic compensating defects [35]. In the following, the experimental results on these issues are summarized for degenerately doped n-type ZnO and (Mg,Zn)O.

(b) **It has been found that**

- group III elements, i.e. Al and Ga, are effective dopants in ZnO with shallow dopant energy levels which are also consistent with existing experimental [10, 176–178] and theoretical [179, 180] works; ZnO and (Mg,Zn)O can be degenerately doped using these dopant elements;

- The solubility limit of ≈ 0.3 at.% of Al in ZnO [9] and (Mg,Zn)O in thermodynamic equilibrium state can be circumvented and doping levels of up to $(2 - 2.5)$ at.% are feasible by preparing samples in metastable states using non-equilibrium growth methods, i.e. pulsed-laser deposition or magnetron sputtering. Thus, growth or annealing temperatures below 400 °C are preferable for the deposition of highly conducting ZnO and (Mg,Zn)O thin films.

- It is still challenging to prevent the formation of intrinsic self-compensating defects, as the formation enthalpy of these defects depends on the Fermi energy [35, 130]. Indeed, $\mathrm{V_{Zn}}$ is the main acceptor-like compensating defect in n-type ZnO and (Mg,Zn)O [149]. Doping limitations by the formation of these defects in ZnO and (Mg,Zn)O compounds can be well explained by the amphoteric defect model that has been successfully applied to several semiconductor materials [131]. According to this model, the Fermi energy level tends to saturate at a certain value. Enhanced free charge carrier density shifts the Fermi energy level upwards, e.g. in n-type ZnO, where the formation energy of compensating defects decreases or even becomes zero [108] and Fermi level pinning occurs. Thus, free carrier concentration cannot be increased by adding additional donors, since they would be compensated due to spontaneous formation of intrinsic acceptors [129, 181]. Experimental data showed that the Fermi level saturates at about 3.6 ± 0.1 eV for the films grown or annealed at higher temperatures, i.e $T_{\mathrm{g/anneal}} \geq 400\,^{\circ}\mathrm{C}$. One of the possible ways to avoid the formation of these compensating defects is to deposit samples in metastable states using non-equilibrium growth methods and choosing the growth or annealing temperatures below 400 °C.

Further, the CCS approach used within this thesis allows for a systematic study of the doping efficiency for different growth or annealing temperatures to determine the n-type Fermi level pinning energies for several different oxide materials which is of fundamental interest for theoreticians.

Abbreviations

ADM	**A**mphoteric **d**efect **m**odel
AFM	**A**tomic **f**orce **m**icroscope
AZO	**A**luminum-doped **z**inc **o**xide
BB	**B**and-**b**and (transition)
c-**plane** Al_2O_3	Single crystal α-sapphire, i.e. 001 oriented
CCS	**C**ontinuous **c**omposition **s**pread method
CB	**C**onduction **b**and
CBM	**C**onduction **b**and **m**inimum
DF	**D**ielectric **f**unction
DFT	**D**ensity-**f**unctional **t**heory
DOS	**D**ensity-**o**f-**s**tates
EDX	**E**nergy **d**ispersive **X**-ray spectroscopy
e.g.	**E**xempli **g**ratia (= for example)
FC	**F**ree **c**arrier
fcc	**F**ace-**c**entered **c**ubic
FWHM	**F**ull-**w**idth at **h**alf-**m**aximum
FTO	**F**luorine-doped **t**in **o**xide
i.e.	**i**d **e**st (= that is)
GGA	**G**eneralized **g**radient **a**pproximation
GZO	**G**allium-doped **z**inc **o**xide
hcp	**H**exagonal **c**lose-**p**acked
IRSE	**I**nfra**r**ed **s**pectroscopic **e**llipsometry
ITO	**T**in-doped **i**nduim **o**xide
LED	**L**ight **e**mitting **d**iodes
(Mg,Zn)O	$\mathbf{Mg}_x\mathbf{Zn}_{1-x}\mathbf{O}$ solid solution

NIR	**N**ear **i**nfra**r**ed
NUV	**N**ear **u**ltra**v**iolet
Ph.D.	**D**octor of **Ph**ilosophy
PLD	**P**ulsed-**l**aser **d**eposition
PV	**P**hotovoltaics
RT	**R**oom **t**emperature
SEM	**S**canning **e**lectron **m**icroscope
SNMS	**S**econdary **n**eutral **m**ass **s**pectrometry
TCO	**T**ransparent **c**onductive **o**xide
VB	**V**alence **b**and
VBM	**V**alence **b**and **m**aximum
VIS	**Vis**ible
XRD	**X**-**r**ay **d**iffraction

Physical Constants

Bohr radius	a_{B}	=	$5.29177249 \times 10^{-11}$ m
Boltzmann constant	k_{B}	=	$1.380658 \times 10^{-23}\ \mathrm{J\,K^{-1}}$
		=	$8.617385 \times 10^{-5}\ \mathrm{meV\,K^{-1}}$
Electron mass	m_e	=	$9.1093897 \times 10^{-31}$ kg
Elementary charge	e	=	$1.60217733 \times 10^{-19}$ C
Permittivity of vacuum	ϵ_0	=	$8.854187817 \times 10^{-12}\,\mathrm{F\,m^{-1}}$
Planck constant	h	=	$6.6260755 \times 10^{-34}\ \mathrm{J\,s}$
	$\hbar = h/(2\pi)$	=	$1.05457266 \times 10^{-34}\ \mathrm{J\,s}$
Speed of Light	c	=	$2.997\;924\;58 \times 10^{8}\ \mathrm{m\,s^{-1}}$

Symbols

d	thickness of the film	nm
D	Grain size	nm
E_c	Bottom of the conduction band	eV
E_g	Optical bandgap	eV
E_FS	Fermi level stabilization energy	eV
E_v	Top of the valence band	eV
m_e^*	Effective electron mass	m_e
m_d^*	DOS effective mass	m_e
m_h^*	Effective hole mass	m_e
m_r^*	Reduced mass	m_e
n	Free charge carrier density	cm^{-3}
N_a	Density of compensating defects (acceptors)	cm^{-3}
N_d	Dopant concentration	cm^{-3}
$N_\mathrm{d,act}$	Doping efficiency (n/N_d)	
$\mathrm{pO_2}$	Oxygen partial pressure	mbar
q	Absolute value of the charge of the compensating defects	
r_H	Hall factor	
R_H	Hall coefficient	$\mathrm{m^3C^{-1}}$
R	Reflectance	%
T	Transmittance	%
T_g	Growth temperature	°C
$\mathrm{V_{Zn}}$	Zinc vacancy	

μ_H	Hall mobility	$\mathrm{cm}^2/\mathrm{Vs}$
σ	Conductivity	S/cm
ρ	Resistivity	$\Omega\,\mathrm{cm}$
ω_p	Plasma frequency	rad/s
ϵ	Dielectric constant	–
ϵ_∞	High-frequency dielectric constant	–

Bibliography

[1] K. Ellmer, A. Klein, and B. Rech. *Transparent Conductive Zinc Oxide.* Springer, 2008.

[2] R. S. Ajimsha, A. K. Das, P. Misra, M. P. Joshi, L. M. Kukreja, R. Kumar, T. K. Sharma, and S. M. Oak. Observation of low resistivity and high mobility in Ga doped ZnO thin films grown by buffer assisted pulsed laser deposition. *Journal of Alloys and Compounds*, 638:55 – 58, 2015.

[3] A. Mosbah and M. S. Aida. Influence of deposition temperature on structural, optical and electrical properties of sputtered Al doped ZnO thin films. *Journal of Alloys and Compounds*, 515:149 – 153, 2012.

[4] T. Minami. Transparent conducting oxide semiconductors for transparent electrodes. *Semiconductor Science and Technology*, 20(4):S35, 2005.

[5] G. V. Rao, F. Säuberlich, and A. Klein. Influence of Mg content on the band alignment at CdS/(Zn,Mg)O interfaces. *Applied Physics Letters*, 87(3):032101, 2005.

[6] J. J. Hanak. The "multiple-sample concept" in materials research: Synthesis, compositional analysis and testing of entire multicomponent systems. *Journal of Materials Science*, 5(11):964–971, 1970.

[7] H. von Wenckstern, Z. Zhang, F. Schmidt, J. Lenzner, H. Hochmuth, and M. Grundmann. Continuous composition spread using pulsed-laser deposition with a single segmented target. *CrystEngComm*, 15:10020–10027, 2013.

[8] A. Mavlonov, S. Richter, H. von Wenckstern, R. Schmidt-Grund, J. Lenzner, M. Lorenz, and M. Grundmann. Doping efficiency and limits in (Mg,Zn)O:Al,Ga

thin films with two-dimensional lateral composition spread. *Physica Status Solidi (A)*, 212(12):2850–2855, 2015.

[9] K. Shirouzu, T. Ohkusa, M. Hotta, N. Enomoto, and J. Hojo. Distribution and Solubility Limit of Al in Al_2O_3-Doped ZnO Sintered Body. *Journal of the Ceramic Society of Japan*, 115(1340):254–258, 2007.

[10] Y. Ke, S. Lany, J. J. Berry, J. D. Perkins, P. A. Parilla, A. Zakutayev, T. Ohno, R. O'Hayre, and D. S. Ginley. Enhanced Electron Mobility Due to Dopant-Defect Pairing in Conductive ZnMgO. *Advanced Functional Materials*, 24(19):2875–2882, 2014.

[11] M. Grundmann. Karl Bädeker (1877–1914) and the discovery of transparent conductive materials. *Physica Status Solidi (A)*, 212(7):1409–1426, 2015.

[12] K. M. Yu, M. A. Mayer, D. T. Speaks, H. He, R. Zhao, L. Hsu, S. S. Mao, E. E. Haller, and W. Walukiewicz. Transparent conductors for full spectrum photovoltaics. In *Photovoltaic Specialists Conference (PVSC), 38th IEEE*, pages 002024–002029, 2012.

[13] T. Minami. New n-Type Transparent Conducting Oxides. *MRS Bulletin*, 25: 38–44, 2000.

[14] M. Grundmann. *The Physics of Semiconductors: An Introduction Including Nanophysics and Applications*. Springer, 2016.

[15] K. Ellmer. Resistivity of polycrystalline zinc oxide films: current status and physical limit. *Journal of Physics D: Applied Physics*, 34(21):3097, 2001.

[16] D. S. Ginley and C. Bright. Transparent Conducting Oxides. In *MRS Bulletin*, pages 15–18, 2000.

[17] J. F. Wager, D. A. Keszler, and R. E. Presley. *Transparent Electronics*. Springer, 2008.

[18] I. A. Rauf. Low resistivity and high mobility tin-doped indium oxide films. *Materials Letters*, 18(3):123–127, 1993.

[19] J. Pettersson, C. Platzer-Björkman, and M. Edoff. Temperature-dependent current-voltage and lightsoaking measurements on Cu(In,Ga)Se_2 solar cells with

ALD-Zn$_{1-x}$Mg$_x$O buffer layers. *Progress in Photovoltaics: Research and Applications*, 17(7):460–469, 2009.

[20] J. Pettersson, M. Edoff, and C. Platzer-Björkman. Electrical modeling of Cu(In,Ga)Se$_2$ cells with ALD-Zn$_{1-x}$Mg$_x$O buffer layers. *Journal of Applied Physics*, 111(1):014509, 2012.

[21] M. Grundmann, H. Frenzel, A. Lajn, Mi. Lorenz, F. Schein, and H. von Wenckstern. Transparent semiconducting oxides: Materials and devices. *Physica status solidi (a)*, 207(6):1437–1449, 2010.

[22] R. G. Gordon. Criteria for Choosing Transparent Conductors. *MRS Bulletin*, 25: 52 – 57, 2000.

[23] H. von Wenckstern, R. Schmidt-Grund, C. Bundesmann, A. Müller, C.P. Dietrich, M. Stölzel, M. Lange, and M. Grundmann. *The (Mg,Zn)O Alloy. Handbook of Zinc Oxide and Related Materials, Vol. 1 Materials*, chapter 1, Z.C. Feng ed., pages 257–320. Taylor and Francis/CRC Press, 2012.

[24] K. Matsubara, H. Tampo, H. Shibata, A. Yamada, P. Fons, K. Iwata, and S. Niki. Band-gap modified Al-doped Zn$_{1-x}$Mg$_x$O transparent conducting films deposited by pulsed laser deposition. *Applied Physics Letters*, 85(8):1374–1376, 2004.

[25] W. Wei, C. Jin, J. Narayan, and R. J. Narayan. Optical and electrical properties of gallium-doped Mg$_x$Zn$_{1-x}$O. *Journal of Applied Physics*, 107(1):013510, 2010.

[26] K. Koike, K. Hama, I. Nakashima, S. Sasa, M. Inoue, and M. Yano. Molecular Beam Epitaxial Growth of Al-doped ZnMgO Alloy Films for Modulation-doped ZnO/ZnMgO heterostructures. *Japanese Journal of Applied Physics*, 44(6R):3822–3827, 2005.

[27] D. J. Cohen, K. C. Ruthe, and S. A. Barnett. Transparent conducting Zn$_{1-x}$Mg$_x$o:(Al,In) thin films. *Journal of Applied Physics*, 96(1):459–467, 2004.

[28] Y. Ke, J. Berry, P. Parilla, A. Zakutayev, R O'Hayre, and D. Ginley. The origin of electrical property deterioration with increasing Mg concentration in ZnMgO:Ga. *Thin Solid Films*, 520(9):3697 – 3702, 2012.

[29] Q.-B. Ma, H.-P. He, Z.-Z. Ye, L.-P. Zhu, J.-Y. Huang, Y.-Z. Zhang, and B.-H. Zhao. Effects of Mg doping on the properties of highly transparent conductive and near

infrared reflective $Zn_{1-x}Mg_xO$:Ga films. *Journal of Solid State Chemistry*, 181(3): 525 – 529, 2008.

[30] K. Maejima, H. Shibata, H. Tampo, K. Matsubara, and S. Niki. Characterization of $Zn_{1-x}Mg_xO$ transparent conducting thin films fabricated by multi-cathode RF-magnetron sputtering. *Thin Solid Films*, 518(11):2949 – 2952, 2010.

[31] K. Ellmer and G. Vollweiler. Electrical transport parameters of heavily-doped zinc oxide and zinc magnesium oxide single and multilayer films heteroepitaxially grown on oxide single crystals. *Thin Solid Films*, 496(1):104–111, 2006.

[32] C. W. Gorrie, A. K. Sigdel, J. J. Berry, B. J. Reese, M. F. A. M. van Hest, P. H. Holloway, D. S. Ginley, and J. D. Perkins. Effect of deposition distance and temperature on electrical, optical and structural properties of radio-frequency magnetron-sputtered gallium-doped zinc oxide. *Thin Solid Films*, 519(1):190 – 196, 2010.

[33] T. Minami, H. Nanto, and S. Takata. Optical Properties of Aluminum Doped Zinc Oxide Thin Films Prepared by RF Magnetron Sputtering. *Japanese Journal of Applied Physics*, 24(8A):L605, 1985.

[34] J. G. Lu, S. Fujita, T. Kawaharamura, H. Nishinaka, Y. Kamada, and T. Ohshima. Carrier concentration induced band-gap shift in Al-doped $Zn_{1-x}Mg_xO$ thin films. *Applied Physics Letters*, 89(26):262107, 2006.

[35] S. B. Zhang, S.-H. Wei, and A. Zunger. Overcoming doping bottlenecks in semiconductors and wide-gap materials. *Physica B: Condensed Matter*, 273 - 274(0): 976 – 980, 1999.

[36] D. Ginley and J. Perkins. *Transpatent Conductors. Handbook of Transparent Conductors*, chapter 1, pages 1–26. Springer, New York, 2010.

[37] M. Lorenz, E.M. Kaidashev, H. von Wenckstern, V. Riede, C. Bundesmann, D. Spemann, G. Benndorf, H. Hochmuth, A. Rahm, H.-C. Semmelhack, and M. Grundmann. Optical and electrical properties of epitaxial $(Mg,Cd)_xZn_{1-x}O$, ZnO, and ZnO:(Ga,Al) thin films on c-plane sapphire grown by pulsed laser deposition. *Solid-State Electronics*, 47(12):2205 – 2209, 2003.

[38] M. Lorenz, H. Hochmuth, M. Kneiß, M. Bonholzer, M. Jenderka, and M. Grundmann. From high-Tc superconductors to highly correlated Mott insulators - 25 years of pulsed laser deposition of functional oxides in Leipzig. *Semiconductor Science and Technology. Special Issue "Semiconducting Functional Oxides"*, 30: 024003, 2015.

[39] R. Schmidt-Grund, M. Schubert, B. Rheinländer, D. Fritsch, H. Schmidt, E. M. Kaidashev, M. Lorenz, C. M. Herzinger, and M. Grundmann. UV-VUV spectroscopic ellipsometry of ternary $Mg_xZn_{1-x}O$ ($0\leq x\leq 0.53$) thin films. *Thin Solid Films*, 455-456:500 – 504, 2004.

[40] R. Schmidt-Grund, A. Carstens, B. Rheinländer, D. Spemann, H. Hochmuth, G. Zimmermann, M. Lorenz, M. Grundmann, C. M. Herzinger, and M. Schubert. Refractive indices and band-gap properties of rocksalt $Mg_xZn_{1-x}O(0.68\leq x\leq 1)$. *Journal of Applied Physics*, 99(12):123701, 2006.

[41] R. Schmidt-Grund, C. Kranert, T. Böntgen, H. von Wenckstern, H. Krauß, and M. Grundmann. Dielectric function in the NIR-VUV spectral range of $(In_xGa_{1-x})_2O_3$ thin films. *Journal of Applied Physics*, 116(5):053510, 2014.

[42] M. Ohring. *The materials science of thin films.* Academic Press, Boston, 1992. p.517.

[43] J. Orton. *The story of semiconductors.* Oxford, 2009.

[44] M. Takase, N. Fukuda, T. Dodo, and S. Fukuda. Transparent panel heater and method for manufacturing same, September 5 1995. US Patent 5,448,037.

[45] D. Pepitone, K.R. Sarma, and S. Wyatt. Aircraft cockpit visor display, August 1 2012. EP Patent App. EP20,110,191,421.

[46] J. G. W. Corrosion resistant coating for metal surfaces, June 22 1943. US Patent 2,322,349.

[47] W. R. Aiken. History of the Kaiser-Aiken, thin cathode ray tube. *IEEE Transactions on Electron Devices*, 31(11):1605–1608, 1984.

[48] D. A. Cathey. Low resistance electrodes useful in flat panel displays, August 30 1994. US Patent 5,342,477.

[49] E. A. Johnson. Touch display—a novel input/output device for computers. *Electronics Letters*, 1:219–220(1), October 1965.

[50] G. J. K. M. Koolen. Low-cost resistive tablet with touch and stylus functionality, July 7 1998. US Patent 5,777,607.

[51] D. Martchovsky. Capacitive touch sensor, December 11 2007. US Patent 7,307,626.

[52] K. Lieberman, Y. Maor, Y. Chay, and Y. Sharon. Optical touch screen assembly, August 24 2010. US Patent 7,781,722.

[53] S. K. Deb. Optical and photoelectric properties and colour centres in thin films of tungsten oxide. *Philosophical Magazine*, 27(4):801–822, 1973.

[54] M. Green. Electrochromic glass for use in cars and buildings, January 28 1997. US Patent 5,598,293.

[55] Best Research-Cell efficiencies, 1976-2016. Technical report, NREL, 2016. URL `www.nrel.gov/ncpv/`.

[56] F. H. Hart. Low emissivity coatings on transparent substrates, July 31 1984. US Patent 4,462,883.

[57] J. E. Day, T. House, and R. Buckley. Low transmission low emissivity glass window and method of manufacture, July 20 1993. US Patent 5,229,881.

[58] T. K. Gupta. Application of Zinc Oxide Varistors. *Journal of the American Ceramic Society*, 73(7):1817–1840, 1990.

[59] D. R. Clarke. Varistor ceramics. *Journal of the American Ceramic Society*, 82(3): 485–502, 1999.

[60] H. Yoshimoto, K. Ito, H. Ichikawa, and T. Honma. Liquid crystal display device having varistor elements, June 2 1992. US Patent 5,119,218.

[61] G. Korotcenkov. Metal oxides for solid-state gas sensors: What determines our choice? *Materials Science and Engineering: B*, 139(1):1 – 23, 2007.

[62] Y.-S. Shim, H. G. Moon, D. H. Kim, H. W. Jang, C.-Y. Kang, Y. S. Yoon, and S.-J. Yoon. Transparent conducting oxide electrodes for novel metal oxide gas sensors. *Sensors and Actuators B: Chemical*, 160(1):357 – 363, 2011.

[63] K. Wetchakun, T. Samerjai, N. Tamaekong, C. Liewhiran, C. Siriwong, V. Kruefu, A. Wisitsoraat, A. Tuantranont, and S. Phanichphant. Semiconducting metal oxides as sensors for environmentally hazardous gases. *Sensors and Actuators B: Chemical*, 160(1):580 – 591, 2011.

[64] H. W. Jang, S. J. Yoon, J. S. Kim, C. Y. Kang, J. W. Choi, and H. G. Moon. High-sensitivity transparent gas sensor and method for manufacturing the same, June 13 2013. US Patent App. 13/542,874.

[65] C. I. Bright. Review of Transparent Conductive Oxides (TCO). In *Fall Bulletin*, pages 38–45, 2008.

[66] G. Rupprecht. Untersuchungen der elektrischen und lichtelektrischen Leitfähigkeit dünner Indiumoxydschichten. *Z. Phys.*, 139:p.504, 1954.

[67] G. Bogner and E. Mollwo. Über die Herstellung von Zinkoxyd Einkristallen mit definierten Zusätzen. *Journal of Physics and Chemistry of Solids*, 6(2):136 – 143, 1958.

[68] J. Aranovich, A. Ortiz, and R. H. Bube. Optical and electrical properties of ZnO films prepared by spray pyrolysis for solar cell applications. *Journal of Vacuum Science & Technology*, 16(4):994–1003, 1979.

[69] J. B. Webb, D. F. Williams, and M. Buchanan. Transparent and highly conductive films of ZnO prepared by rf reactive magnetron sputtering. *Applied Physics Letters*, 39(8):640–642, 1981.

[70] P. S. Nayar and A. Catalano. Zinc phosphide - zinc oxide heterojunction solar cells. *Applied Physics Letters*, 39(1):105–107, 1981.

[71] P. Petrou, R. Singh, and D. E. Brodie. The use of ZnO in transparent type MIS solar cells. *Applied Physics Letters*, 35(12):930–931, 1979.

[72] A. P. Roth and D. F. Williams. Properties of zinc oxide films prepared by the oxidation of diethyl zinc. *Journal of Applied Physics*, 52(11):6685–6692, 1981.

[73] T. Minami. Present status of transparent conducting oxide thin-film development for Indium-Tin-Oxide (ITO) substitutes. *Thin Solid Films*, 516(17):5822 – 5828, 2008.

[74] I. A. Rauf. A novel method for preparing thin films with selective doping in a single evaporation step. *Journal of Materials Science Letters*, 12(24):1902–1905, 1993.

[75] A. Suzuki, T. Matsushita, T. Aoki, Y. Yoneyama, and M. Okuda. Pulsed Laser Deposition of Transparent Conducting Indium Tin Oxide Films in Magnetic Field Perpendicular to Plume. *Japanese Journal of Applied Physics*, 40(4B):L401, 2001.

[76] H. Agura, A. Suzuki, T. Matsushita, T. Aoki, and M. Okuda. Low resistivity transparent conducting Al-doped ZnO films prepared by pulsed laser deposition. *Thin Solid Films*, 445(2):263 – 267, 2003.

[77] V. Bhosle, A. Tiwari, and J. Narayan. Electrical properties of transparent and conducting Ga doped ZnO. *Journal of Applied Physics*, 100(3):033713, 2006.

[78] H. Kim, G. P. Kushto, R. C. Y. Auyeung, and A. Piqué. Optimization of F-doped SnO_2 electrodes for organic photovoltaic devices. *Applied Physics A*, 93(2): 521–526, 2008.

[79] H. Liu, V. Avrutin, N. Izyumskaya, Ü. Özgür, and H. Morkoç. Transparent conducting oxides for electrode applications in light emitting and absorbing devices. *Superlattices and Microstructures*, 48(5):458 – 484, 2010.

[80] L. Chinnappa, K. Ravichandran, K. Saravanakumar, G. Muruganantham, and B. Sakthivel. The combined effects of molar concentration of the precursor solution and fluorine doping on the structural and electrical properties of tin oxide films. *Journal of Materials Science: Materials in Electronics*, 22(12):1827–1834, 2011.

[81] D. Tatar and B. Düzgün. The relationship between the doping levels and some physical properties of SnO_2:F thin films spray-deposited on optical glass. *Pramana*, 79(1):137–150, 2012.

[82] G. Zhu and Z. Yang. Effect of sputtering power and annealing temperature on the properties of indium tin oxide thin films prepared from radio frequency sputtering using powder target. *Journal of Materials Science: Materials in Electronics*, 24 (10):3646–3651, 2013.

[83] J. Du, X. Chen, C. Liu, J. Ni, G. Hou, Y. Zhao, and X. Zhang. Highly transparent and conductive indium tin oxide thin films for solar cells grown by reactive thermal evaporation at low temperature. *Applied Physics A*, 117(2):815–822, 2014.

[84] K. Zhu, Y. Yang, and W. Song. Effects of substrate temperature on the structural, morphological, electrical and optical properties of Al and Ga co-doped ZnO thin films grown by {DC} magnetron sputtering. *Materials Letters*, 145(0):279 – 282, 2015.

[85] E. Mokaripoor and M.-M. Bagheri-Mohagheghi. Effect of very low to high Sb-doping on the structural, electrical, photo-conductive and thermoelectric properties of fluorine-doped SnO_2 (FTO) thin films prepared by spray pyrolysis technique. *Journal of Materials Science: Materials in Electronics*, 27(3):2305–2314, 2015.

[86] O. Gürbüz, I. Kurt, S. Çalişkan, and S. Güner. Influence of Al concentration and annealing temperature on structural, optical, and electrical properties of Al co-doped ZnO thin films. *Applied Surface Science*, 349:549 – 560, 2015.

[87] T. Minami, H. Nanto, and S. Takata. Highly conductive and transparent zinc oxide films prepared by rf magnetron sputtering under an applied external magnetic field. *Applied Physics Letters*, 41(10):958–960, 1982.

[88] T. Hada, K. Wasa, and S. Hayakawa. Structures and electrical properties of zinc oxide films prepared by low pressure sputtering system. *Thin Solid Films*, 7(2): 135 – 145, 1971.

[89] T. Minami, H. Sato, H. Nanto, and S. Takata. Highly Conductive and Transparent Silicon Doped Zinc Oxide Thin Films Prepared by RF Magnetron Sputtering. *Japanese Journal of Applied Physics*, 25(9A):L776–L779, 1986.

[90] H. Sato, T. Minami, and S. Takata. Highly transparent and conductive group IV impurity-doped ZnO thin films prepared by radio frequency magnetron sputtering. *Journal of Vacuum Science & Technology A*, 11(6):2975–2979, 1993.

[91] J. Hu and R. G. Gordon. Textured fluorine-doped ZnO films by atmospheric pressure chemical vapor deposition and their use in amorphous silicon solar cells. *Solar Cells*, 30(1–4):437 – 450, 1991.

[92] O. Kuboi. Degradation of ITO Film in Glow-Discharge Plasma. *Japanese Journal of Applied Physics*, 20(11):L783, 1981.

[93] M. Kitagawa, K. Mori, S. Ishihara, M. Ohno, T. Hirao, Y. Yoshioka, and S. Kohiki. Interaction of hydrogenated amorphous silicon films with transparent conductive films. *Journal of Applied Physics*, 54(6):3269–3271, 1983.

[94] T. Minami, H. Sato, H. Nanto, and S. Takata. Group III Impurity Doped Zinc Oxide Thin Films Prepared by RF Magnetron Sputtering. *Japanese Journal of Applied Physics*, 24(10A):L781–L784, 1985.

[95] T. Minami, T. Yamamoto, and T. Miyata. Highly transparent and conductive rare earth-doped ZnO thin films prepared by magnetron sputtering. *Thin Solid Films*, 366(1–2):63 – 68, 2000.

[96] JCPDS 79-2205. International Centre for Diffraction Data. 1998.

[97] K. Momma and F. Izumi. Vesta 3 for three-dimensional visualization of crystal, volumetric and morphology data. *J. Appl. Crystallogr.*, 44:1272–1276, 2011.

[98] P. Erhart, K. Albe, and A. Klein. First-principles study of intrinsic point defects in ZnO: Role of band structure, volume relaxation, and finite-size effects. *Physical Review B*, 73:205203, 2006.

[99] D. L. Young, T. J. Coutts, V. I. Kaydanov, A. S. Gilmore, and W. P. Mulligan. Direct measurement of density-of-states effective mass and scattering parameter in transparent conducting oxides using second-order transport phenomena. *Journal of Vacuum Science & Technology A*, 18(6):2978–2985, 2000.

[100] A. Tsukazaki, A. Ohtomo, T. Kita, Y. Ohno, H. Ohno, and M. Kawasaki. Quantum Hall Effect in Polar Oxide Heterostructures. *Science*, 315(5817):1388–1391, 2007.

[101] A. Ohtomo, M. Kawasaki, T. Koida, K. Masubuchi, H. Koinuma, Y. Sakurai, Y. Yoshida, T. Yasuda, and Y. Segawa. $\mathrm{Mg}_x\mathrm{Zn}_{1-x}\mathrm{O}$ as a II-VI widegap semiconductor alloy. *Applied Physics Letters*, 72(19):2466–2468, 1998.

[102] S. Choopun, R. D. Vispute, W. Yang, R. P. Sharma, T. Venkatesan, and H. Shen. Realization of band gap above 5.0 eV in metastable cubic-phase $\mathrm{Mg}_x\mathrm{Zn}_{1-x}\mathrm{O}$ alloy films. *Applied Physics Letters*, 80(9):1529–1531, 2002.

[103] N. B. Chen, H. Z. Wu, D. J. Qiu, T. N. Xu, J. Chen, and W. Z. Shen. Temperature-dependent optical properties of hexagonal and cubic $\mathrm{Mg}_x\mathrm{Zn}_{1-x}\mathrm{O}$ thin-film alloys. *Journal of Physics: Condensed Matter*, 16(17):2973, 2004.

[104] Y. Ke. *Towards Improved Understanding and Conductivity in Band-Gap-Tunable Zinc Magnesium Oxide*. PhD thesis, Colorado School of Mines, 2013.

[105] X. D. Zhang, M. L. Guo, C. L. Liu, L. A. Zhang, W. Y. Zhang, Y. Q. Ding, Q. Wu, and X. Feng. First-principles investigation of electronic and optical properties in wurtzite $\mathrm{Zn}_{1-x}\mathrm{Mg}_x\mathrm{O}$. *Eur. Phys. J. B*, 62(4):417–421, 2008.

[106] S. Lany and A. Zunger. Dopability, Intrinsic Conductivity, and Nonstoichiometry of Transparent Conducting Oxides. *Physical Review Letters*, 98:045501, 2007.

[107] S. Lany, J. Osorio-Guillén, and A. Zunger. Origins of the doping asymmetry in oxides: Hole doping in NiO versus electron doping in ZnO. *Physical Review B*, 75: 241203, 2007.

[108] F. Oba, M. Choi, A. Togo, and I. Tanaka. Point defects in ZnO: an approach from first principles. *Science and Technology of Advanced Materials*, 12(3):034302, 2011.

[109] A. F. Kohan, G. Ceder, D. Morgan, and Chris G. Van de Walle. First-principles study of native point defects in ZnO. *Physical Review B*, 61:15019–15027, 2000.

[110] F. Oba. Defect energetics in ZnO: A hybrid Hartree-Fock density functional study. *Physical Review B*, 77:245202, 2008.

[111] A. Janotti and C. G. Van de Walle. Native point defects in ZnO. *Physical Review B*, 76(12):122102, 2007.

[112] A. A. Sokol, S. A. French, S. T. Bromley, C. R. A. Catlow, H. J. J. van Dam, and P. Sherwood. Point defects in ZnO. *Faraday Discuss.*, 134:267–282, 2007.

[113] F. Oba, M. Choi, A. Togo, A. Seko, and I. Tanaka. Native defects in oxide semiconductors: a density functional approach. *Journal of Physics: Condensed Matter*, 22(38):384211, 2010.

[114] S. B. Zhang, S.-H. Wei, and A. Zunger. Intrinsic n -type versus p -type doping asymmetry and the defect physics of ZnO. *Physical Review B*, 63:075205, 2001.

[115] D. C. Look, K. D. Leedy, L. Vines, B. G. Svensson, A. Zubiaga, F. Tuomisto, D. R. Doutt, and L. J. Brillson. Self-compensation in semiconductors: The Zn vacancy in Ga-doped ZnO. *Physical Review B*, 84:115202, 2011.

[116] A. Janotti and C. G. Van de Walle. Fundamentals of zinc oxide as a semiconductor. *Reports on Progress in Physics*, 72(12):126501, 2009.

[117] D. C. Look, J. W. Hemsky, and J. R. Sizelove. Residual Native Shallow Donor in ZnO. *Physical Review Letters*, 82:2552–2555, 1999.

[118] D. G. Thomas. The diffusion and precipitation of Indium in Zinc Oxide. *Journal of Physics and Chemistry of Solids*, 9(1):31 – 42, 1959.

[119] B. K. Meyer, J. Sann, S. Lautenschläger, M. R. Wagner, and A. Hoffmann. Ionized and neutral donor-bound excitons in ZnO. *Physical Review B*, 76:184120, 2007.

[120] I. Sieber, N. Wanderka, I. Urban, I. Dörfel, E. Schierhorn, F. Fenske, and W. Fuhs. Electron microscopic characterization of reactively sputtered ZnO films with different Al-doping levels. *Thin Solid Films*, 330(2):108 – 113, 1998.

[121] S. Cornelius, M. Vinnichenko, N. Shevchenko, A. Rogozin, A. Kolitsch, and W. Möller. Achieving high free electron mobility in ZnO:Al thin films grown by reactive pulsed magnetron sputtering. *Applied Physics Letters*, 94(4):042103, 2009.

[122] M. Grundmann. *The Physics of Semiconductors, An Introduction Including Nanophysics and Applications.* Springer, 2010.

[123] L. Makowski and M. Glicksman. Disorder scattering in solid solutions of iii–v semiconducting compounds. *Journal of Physics and Chemistry of Solids*, 34(3): 487 – 492, 1973.

[124] A. Bikowski and K. Ellmer. A comparative study of electronic and structural properties of polycrystalline and epitaxial magnetron-sputtered ZnO:Al and $Zn_{1-x}Mg_xO$:Al Films—Origin of the grain barrier traps. *Journal of Applied Physics*, 114(6):063709, 2013.

[125] D. J. Chadi. Doping in ZnSe, ZnTe, MgSe, and MgTe wide-band-gap semiconductors. *Physical Review Letters*, 72:534–537, Jan 1994.

[126] W. Walukiewicz. Activation of shallow dopants in II-VI compounds. *Journal of Crystal Growth*, 159(1-4):244 – 247, 1996.

[127] J. Qiu, J. M. DePuydt, H. Cheng, and M. A. Haase. Heavily doped p-ZnSe:N grown by molecular beam epitaxy. *Applied Physics Letters*, 59(23):2992–2994, 1991.

[128] I. S. Hauksson, J. Simpson, S. Y. Wang, K. A. Prior, and B. C. Cavenett. Compensation processes in nitrogen doped ZnSe. *Applied Physics Letters*, 61(18):2208–2210, 1992.

[129] W. Walukiewicz. Mechanism of Fermi-level stabilization in semiconductors. *Physical Review B*, 37:4760–4763, 1988.

[130] W. Walukiewicz. Amphoteric native defects in semiconductors. *Applied Physics Letters*, 54(21):2094–2096, 1989.

[131] W. Walukiewicz. Intrinsic limitations to the doping of wide-gap semiconductors. *Physica B: Condensed Matter*, 302-303:123–134, 2001.

[132] A. Zunger. Theory of 3d Transition Atom Impurities in Semiconductors. *Annual Review of Materials Science*, 15(1):411–453, 1985.

[133] J. M. Langer and H. Heinrich. Deep-Level Impurities: A Possible Guide to Prediction of Band-Edge Discontinuities in Semiconductor Heterojunctions. *Physical Review Letters*, 55:1414–1417, 1985.

[134] K. L. Chopra, S. Major, and D. K. Pandya. Transparent conductors—A status review. *Thin Solid Films*, 102(1):1–46, 1983.

[135] URL `http://www.Alfa-chemcat.com`.

[136] URL `http://www.sigmaaldrich.com`.

[137] Z. Zhang, H. von Wenckstern, and M. Grundmann. Energy-selective multichannel ultraviolet photodiodes based on (Mg,Zn)O. *Applied Physics Letters*, 103(17): 171111, 2013.

[138] H. von Wenckstern, Z. Zhang, J. Lenzner, F. Schmidt, and M. Grundmann. A continuous composition spread approach towards monolithic, wavelength-selective

multichannel UV-photo-detector arrays. In *Symposium R – Oxide Semiconductors*, volume 1633 of *MRS Online Proceedings Library*, pages 123–129, 2014.

[139] Z. Zhang, H. von Wenckstern, and M. Grundmann. Monolithic Multichannel Ultraviolet Photodiodes Based on (Mg,Zn)O Thin Films With Continuous Composition Spreads. *Selected Topics in Quantum Electronics, IEEE Journal of*, 20 (6):106–111, 2014.

[140] C. Kranert, J. Lenzner, M. Jenderka, M. Lorenz, H. von Wenckstern, R. Schmidt-Grund, and M. Grundmann. Lattice parameters and Raman-active phonon modes of $(\mathrm{In}_x\mathrm{Ga}_{1-x})_2\mathrm{O}_3$ for x<0.4. *Journal of Applied Physics*, 116(1):013505, 2014.

[141] H. von Wenckstern, D. Splith, M. Purfürst, Z. Zhang, Ch. Kranert, S. Müller, M. Lorenz, and M. Grundmann. Structural and optical properties of $(\mathrm{In,Ga})_2\mathrm{O}_3$ thin films and characteristics of Schottky contacts thereon. *Semiconductor Science and Technology*, 30(2):024005, 2015.

[142] L. J. van der Pauw. A method of measuring specific resistivity and Hall effect of discs of arbitrary shape. *Phillips Research Reports*, 13(1), 1958.

[143] H. von Wenckstern. *Doping, contacting, defect levels and transport properties of ZnO*. PhD thesis, Universität Leipzig, 2008.

[144] K. Ellmer. *Hall Effect and Conductivity Measurements in Semiconductor Crystals and Thin Films. Book Chap. Characterization of Materials. Edit. Elton N. Kaufmann.* John Wiley & Sons, Inc., 2012.

[145] P. Nunes, E. Fortunato, P. Tonello, F. B. Fernandes, P . Vilarinho, and R. Martins. Effect of different dopant elements on the properties of ZnO thin films. *Vacuum*, 64(3–4):281 – 285, 2002.

[146] D.-J. Lee, H.-M. Kim, J.-Y. Kwon, H. Choi, S.-H. Kim, and K.-B. Kim. Structural and Electrical Properties of Atomic Layer Deposited Al-Doped ZnO Films. *Advanced Functional Materials*, 21(3):448–455, 2011.

[147] R. Wang, A. W. Sleight, and D. Cleary. High Conductivity in Gallium-Doped Zinc Oxide Powders. *Chemistry of Materials*, 8(2):433–439, 1996.

[148] G. Frank and H. Köstlin. Electrical properties and defect model of tin-doped indium oxide layers. *Applied Physics A*, 27(4):197–206, 1982.

[149] F. Tuomisto, V. Ranki, K. Saarinen, and D. C. Look. Evidence of the Zn Vacancy Acting as the Dominant Acceptor in n-Type ZnO. *Physical Review Letters*, 91: 205502, 2003.

[150] D. C. Look, K. D. Leedy, D. B. Thomson, and B. Wang. Defects in highly conductive ZnO for transparent electrodes and plasmonics. *Journal of Applied Physics*, 115(1):012002, 2014.

[151] D. C. Look, K. D. Leedy, and D. L. Agresta. Nondestructive quantitative mapping of impurities and point defects in thin films: Ga and V_{Zn} in ZnO:Ga. *Applied Physics Letters*, 104(24):242107, 2014.

[152] E. Korhonen, V. Prozheeva, F. Tuomisto, O. Bierwagen, J. S. Speck, M. E. White, Z. Galazka, H. Liu, N. Izyumskaya, V. Avrutin, Ü. Özgür, and H. Morkoç. Cation vacancies and electrical compensation in Sb-doped thin-film SnO_2 and ZnO. *Semiconductor Science and Technology*, 30(2):024011, 2015.

[153] M. Gabás, A. Landa-Cánovas, J. L. Costa-Krämer, F. Agulló-Rueda, A. R. González-Elipe, P. Díaz-Carrasco, J. Hernández-Moro, I. Lorite, P. Herrero, P. Castillero, A. Barranco, and J.R. Ramos-Barrado. Differences in n-type doping efficiency between Al- and Ga-ZnO films. *Journal of Applied Physics*, 113(16): 163709, 2013.

[154] J. F. Chang, W. C. Lin, and M. H. Hon. Effects of post-annealing on the structure and properties of Al-doped zinc oxide films. *Applied Surface Science*, 183(1–2): 18–25, 2001.

[155] H. Tong, Z. Deng, Z. Liu, C. Huang, J. Huang, H. Lan, C. Wang, and Y. Cao. Effects of post-annealing on structural, optical and electrical properties of Al-doped ZnO thin films. *Applied Surface Science*, 257(11):4906 – 4911, 2011.

[156] C. Charpentier, P. Prod'homme, and P. Roca i Cabarrocas. Microstructural, optical and electrical properties of annealed ZnO:Al thin films. *Thin Solid Films*, 531 (0):424–429, March 2013.

[157] W. M. Kim, J. S. Kim, J.-H. Jeong, J.-K. Park, Y.-J. Baik, and T.-Y. Seong. Analysis of optical band-gap shift in impurity doped ZnO thin films by using non-parabolic conduction band parameters. *Thin Solid Films*, 531(0):430–435, 2013.

[158] Z.-C. Jin, I. Hamberg, and C. G. Granqvist. Optical properties of sputter-deposited ZnO:Al thin films. *Journal of Applied Physics*, 64(10):5117–5131, 1988.

[159] C. Agashe, O. Kluth, J. Hüpkes, U. Zastrow, B. Rech, and M. Wuttig. Efforts to improve carrier mobility in radio frequency sputtered aluminum doped zinc oxide films. *Journal of Applied Physics*, 95(4):1911–1917, 2004.

[160] S. Mandal, H. Mullick, S. Majumdar, A. Dhar, and S. K. Ray. Effect of Al concentration in grain and grain boundary region of Al-doped ZnO films: a dielectric approach. *Journal of Physics D: Applied Physics*, 41(2):025307, 2008.

[161] Y. Kim, W. Lee, D.-R. Jung, J. Kim, S. Nam, H. Kim, and B. Park. Optical and electronic properties of post-annealed ZnO:Al thin films. *Applied Physics Letters*, 96:171902, 2010.

[162] C. Zhu, J. Li, Y. Yang, J. Huang, Y. Lu, R. Tan, N. Dai, and W. Song. Zn-aided defect control for ultrathin GZO films with high carrier concentration aiming at alternative plasmonic metamaterials. *Physica Status Solidi (A)*, 212(8):1713–1718, 2015.

[163] J. G. Lu, Z. Z. Ye, Y. J. Zeng, L. P. Zhu, L. Wang, J. Yuan, B. H. Zhao, and Q. L. Liang. Structural, optical, and electrical properties of (Zn,Al)O films over a wide range of compositions. *Journal of Applied Physics*, 100(7):073714, 2006.

[164] R. Pandey, S. Yuldashev, H. D. Nguyen, H. C. Jeon, and T. W. Kang. Fabrication of aluminium doped zinc oxide (AZO) transparent conductive oxide by ultrasonic spray pyrolysis. *Current Applied Physics*, 12(4):S56–S58, 2012.

[165] J. Liu, X. Zhao, L. Duan, H. Sun, X. Bai, L. Chen, and C. Chen. Effect of annealing ambient on electrical and optical properties of Ga-doped $Mg_xZn_{1-x}O$ films. *Applied Surface Science*, 258(17):6297–6301, 2012.

[166] A. Zakutayev, N. H. Perry, T. O. Mason, D. S. Ginley, and S. Lany. Non-equilibrium origin of high electrical conductivity in gallium zinc oxide thin films. *Applied Physics Letters*, 103(23):232106, 2013.

[167] T. Minami, H. Nanto, S. Shooji, and S. Takata. The stability of zinc oxide transparent electrodes fabricated by R.F. magnetron sputtering. *Thin Solid Films*, 111 (2):167–174, 1984.

[168] O. Caporaletti. Heat treatment of bias sputtered ZnO films. *Solid State Communications*, 42(2):109–111, 1982.

[169] G. Neumann. On the Defect Structure of Zinc-Doped Zinc Oxide. *Physica Status Solidi (B)*, 105(2):605–612, 1981.

[170] E. Ziegler, A. Heinrich, H. Oppermann, and G. Stöver. Electrical properties and non-stoichiometry in ZnO single crystals. *Physica Status Solidi (A)*, 66(2):635–648, 1981.

[171] M. Buchanan, J. B. Webb, and D. F. Williams. Preparation of conducting and transparent thin films of tin-doped indium oxide by magnetron sputtering. *Applied Physics Letters*, 37(2):213–215, 1980.

[172] S. Takata, T. Minami, and H. Nanto. The stability of aluminium-doped ZnO transparent electrodes fabricated by sputtering. *Thin Solid Films*, 135(2):183–187, 1986.

[173] S. N. Qiu, C. X. Qiu, and I. Shih. Air heat treatment of In-doped ZnO thin films. *Solar Energy Materials*, 15(4):261–267, 1987.

[174] T. Minami, K. Oohashi, S. Takata, T. Mouri, and N. Ogawa. Preparations of ZnO:Al transparent conducting films by d.c. magnetron sputtering. *Thin Solid Films*, 193-194:721–729, 1990.

[175] A. Mavlonov, S. Richter, H. von Wenckstern, R. Schmidt-Grund, M. Lorenz, and M. Grundmann. Temperature dependent self-compensation in Al- and Ga-doped $Mg_{0.05}Zn_{0.95}O$ thin films grown by pulsed laser deposition. *Journal of Applied Physics*, 120, 2016. doi: 10.1063/1.4968544. (Accepted).

[176] B. M. Ataev, A. M. Bagamadova, A. M. Djabrailov, V. V. Mamedov, and R. A. Rabadanov. Highly conductive and transparent Ga-doped epitaxial ZnO films on sapphire by {CVD}. *Thin Solid Films*, 260(1):19 – 20, 1995.

[177] T. Minami, H. Nanto, and S. Takata. Highly Conductive and Transparent Aluminum Doped Zinc Oxide Thin Films Prepared by RF Magnetron Sputtering. *Japanese Journal of Applied Physics*, 23(5A):L280, 1984.

[178] S. Y. Myong, S. J. Baik, Ch. H. Lee, W. Y. Cho, and K. S. Lim. Extremely Transparent and Conductive ZnO:Al Thin Films Prepared by Photo-Assisted Metalorganic Chemical Vapor Deposition (photo-MOCVD) Using $AlCl_3(6H_2O)$ as New Doping Material. *Japanese Journal of Applied Physics*, 36(8B):L1078, 1997.

[179] G. F. Neumark. Achievement of well conducting wide band-gap semiconductors: Role of solubility and of nonequilibrium impurity incorporation. *Physical Review Letters*, 62:1800–1803, 1989.

[180] S. B. Zhang. The microscopic origin of the doping limits in semiconductors and wide-gap materials and recent developments in overcoming these limits: a review. *Journal of Physics: Condensed Matter*, 14(34):R881, 2002.

[181] S. B. Zhang, S.-H. Wei, and A. Zunger. A phenomenological model for systematization and prediction of doping limits in II-VI and I-III-VI_2 compounds. *Journal of Applied Physics*, 83(6):3192–3196, 1998.

Acknowledgements

First, I am grateful to my supervisors, Prof. Dr. Marius Grundmann for letting me doing self-determined research in his labs where it is possible to grow the high quality thin films and to systematic investigate their chemical, structural, electrical and optical properties using high standard techniques in house, and Dr. Holger von Wenckstern for his guidance during my Ph.D study.

I gratefully acknowledge my colleagues and friends in “Semiconductor Physics Group”, where I received countless help and support. In particular:

Anja Heck and Birgit Wendisch for administration,

Gabriele Ramm for target preparation and SNMS measurements,

Holger Hochmuth for sample deposition by PLD,

Monika Hahn for sample preparation and photolytography,

Ulrike Teschner for transmission and reflection measuremants,

Jörg Lenzner for EDX, CL, SEM measurements,

Dr. Fabian Klüpfel and Daniel Splith for the softwares which have been used for analyzing the experimental data,

Dr. Christian Kranert for the animation on CCS process,

Prof. Dr. Michael Lorenz for discussion on XRD measurement data,

Dr. Florian Schmidt and Michael Bonholzer for AFM measurements,

Dr. Rüdiger Schmidt-Grund and Steffen Richter for SE measurements,

Dr. Rüdiger Schmidt-Grund, Dr. Chris Sturm, Dr. Stefan Müller, Peter Schlupp, Daniel Splith and Steffen Richter for the discussion and proof-reading of the thesis.

I am thankful to my family, both in Uzbekistan and here in Germany, as well as friends, Bernd and Renata Jonke, for their support all the time.

Financial supports by the Islamic Development Bank (IDB) within the framework of “Merit Scholarship for High Technology” (No. 91.UZB.P32, Stud.-ID. 600014428), the Graduate School Leipzig School of Natural Sciences - BuildMoNa and the Deutsche Forschungsgemeinschaft (DFG) within SFB 762 are gratefully acknowledged.

Curriculum vitae

Personal information

- Name: Abdurashid Abduvahobovich Mavlonov
- Date of Birth: April 3, 1986
- Place of Birth: Tashkent, Uzbekistan
- Nationality: Uzbek
- Children: Zebo Abduvakhobova (born August 17, 2007), Muazzam Abduvakhobova (born July 27, 2011), Zokir Mavlonov (born March 1, 2015)

Education and scientific activities

- 1992-1999 Primary and secondary school in Tashkent Region
- 1999-2001 Secondary school, gymnasium in Tashkent
- 2001-2003 High school, lyceum in Tashkent
- 2003-2007 Study of physics at National University of Uzbekistan, Tashkent
- 2007-2009 M. Sc. at National University of Uzbekistan, Tashkent
- 2009-2010 Exchanging student at South-west Jiaotong University, Chengdu, China
- since 10/2010 Junior researcher at Physical-Technical Institute, Scientific Production Association "Physics-Sun", Academy of Science of Uzbekistan (since 10/2012: sabbatical leave.)
- since 10/2012 Ph.D. student at Universität Leipzig

Declaration of Authorship

I, Abdurashid Mavlonov, declare that this thesis titled, “Doping Efficiency and Limits in Wurtzite (Mg,Zn)O Alloys” and the work presented in it are my own. I confirm that:

- This work was done wholly or mainly while in candidature for a research degree at this University.
- Where any part of this thesis has previously been submitted for a degree or any other qualification at this University or any other institution, this has been clearly stated.
- Where I have consulted the published work of others, this is always clearly attributed.
- Where I have quoted from the work of others, the source is always given. With the exception of such quotations, this thesis is entirely my own work.
- I have acknowledged all main sources of help.
- Where the thesis is based on work done by myself jointly with others, I have made clear exactly what was done by others and what I have contributed myself.

Signed: ______________________________

Date: ______________________________

Minor changes have been made compared to the submitted version, namely:

- Recent experimental data was added to Table 7.1 during the manuscript preparation for publication. Data is also published in [175].
- According to the publication of Ma *et al.* [29], the Mg content in Figure 7.9 was changed.
- At the end of Chapter7, it has been mentioned that the results of this chapter has been accepted for publication on *J. Appl. Phys.* [175].